APPLICATION OF ELECTROANALYTICAL METHODS TO INVESTIGATE BIOGEOCHEMICAL PROCESSES FROM GLOBAL TO MOLECULAR SCALES

by

Jeffrey M. Hudson

A dissertation submitted to the Faculty of the University of Delaware in partial fulfillment of the requirements for the degree of Doctor of Philosophy in Civil Engineering

Spring 2022

APPLICATION OF ELECTROANALYTICAL METHODS TO INVESTIGATE BIOGEOCHEMICAL PROCESSES FROM GLOBAL TO MOLECULAR SCALES

by

Jeffrey M. Hudson

Approved: _____
Jack A. Puleo, Ph.D.
Chair of the Department of Civil and Environmental Engineering

Approved: _____
Levi T. Thompson, Ph.D.
Dean of the College of Engineering

Approved: _____
Louis F. Rossi, Ph.D.
Vice Provost for Graduate and Professional Education and
Dean of the Graduate College

I certify that I have read this dissertation and that in my opinion it meets the academic and professional standard required by the University as a dissertation for the degree of Doctor of Philosophy.

Signed: _____

Yu-Ping Chin, Ph.D.
Professor in charge of dissertation

I certify that I have read this dissertation and that in my opinion it meets the academic and professional standard required by the University as a dissertation for the degree of Doctor of Philosophy.

Signed: _____

Pei C. Chiu, Ph.D.
Member of dissertation committee

I certify that I have read this dissertation and that in my opinion it meets the academic and professional standard required by the University as a dissertation for the degree of Doctor of Philosophy.

Signed: _____

Dominic M. Di Toro, Ph.D.
Member of dissertation committee

I certify that I have read this dissertation and that in my opinion it meets the academic and professional standard required by the University as a dissertation for the degree of Doctor of Philosophy.

Signed: _____

George W. Luther III, Ph.D.
Member of dissertation committee

ACKNOWLEDGMENTS

Wow! I have so many people to acknowledge and thank that I don't even know where to begin. First off, I will start with my incredible advisor Yo, who was not just a boss, but a mentor and second father figure for me throughout these years. Moving from Ohio State was worth the risk and I will never regret it! I also want to thank my committee for their advisement, particularly Dr. Luther who enabled me to study a bit under his wing on two research cruises early on. That really helped me out when I was a young and struggling grad student. I also really enjoyed journal clubs with Dr. Chiu's group and enjoyed the modeling courses with Dr. Di Toro; I learned so much! Finally, on the work side of things, I'd like to thank the Chin lab group for helping me with research and reminding me how important it is to keep it "fun." They were also always down for a good laugh or deep conversation.

As far as my friends, family, and loved ones: I want to thank the "Quinonebians" for always providing encouragement and giving me inspiration. I also enjoyed working with some of you! My high school buddies back home, especially Eric, Mike, and Dave: I know you never really understood what my research was about, but nonetheless you were steadfast in your support. To my parents: You guys always have supported me everywhere I've gone and everything I've done. At times, our weekly zoom chats were what gave me encouragement when I was having a tough week. And finally, to my beautiful girlfriend Dani: I am the luckiest man in the world. Thank you for supporting me during my PhD, and I can't wait to see you obtain your own PhD within a few months and celebrate together!

TABLE OF CONTENTS

LIST OF TABLES

LIST OF FIGURES

ABSTRACT

Electroanalytical methods are widely applicable in a variety of scientific fields and have proven to be a useful tool for fundamental and applied scientific investigations involving redox reactions and species. Over the past decades, electrochemical methods have been increasingly applied to investigate environmental processes. Environmental applications of electrochemistry range from large-scale environmental monitoring to bench-top investigations of fundamental processes at a micro-scale. This dissertation primarily applies two analytical techniques, voltammetry and mediated electrochemical oxidation (MEO), to directly investigate *in situ* redox cycling in estuarine and lacustrine environments, and to probe iron complexation and redox dynamics with organic ligands in a controlled laboratory setting.

Voltammetric microelectrodes were used in conjunction with a pump-profiling system to measure concentrations of redox-active species (O_2, Mn^{II}, Fe^{II}, H_2S) associated with a stratified water column in Chesapeake Bay. Electrochemical measurements of high vertical resolution were achieved in the water column with the pumping system, which was also used to measure other constituents. Microelectrodes displayed high precision and accuracy when compared with other sensors onboard a research vessel, and measurements from two separate years showed distinct redox zonation between bottom and surface waters that were influenced by freshwater inputs from tributaries.

Voltammetric microelectrodes were then applied to Arctic lacustrine systems near Toolik Lake, AK to investigate the distribution of redox-active species (O_2, Mn^{II}, Fe^{II}, Fe^{III}-complexes) associated with terminal electron acceptors (TEA). High vertical resolution profiles of TEAs in Toolik Lake sediment pore waters and iron-rich seeps were paired with microbiological analysis of iron and carbon cycling bacteria. Results enable the interpretation of relationships between the location the distribution of TEAs, while gaining insight into the influence of TEAs and other geochemical parameters on carbon cycling in the Arctic, which is particularly sensitive to climate change.

MEO was used to investigate the influence of model organic ligands on Fe^{II} oxidation across fixed thermodynamic conditions (i.e. E_H and pH). Iron oxidation reactions play an important role in biogeochemical processes, such carbon cycling and sequestration, as well as environmental transformation of nitroaromatic explosives. Fe^{III}-stabilizing ligands containing oxygen or nitrogen donor atoms induced high-spin Fe^{II} and increased oxidation e*xtent* at lower pH by decreasing the thermodynamic stability of Fe^{II}. Additionally, a linear relationship exists between measured apparent reduction potentials (E_H^{Φ}) of the Fe-ligand complexes and the ratio of their known stability constants (log $K_{Fe(III)}$ /$K_{Fe(II)}$), thus enabling the determination of stability constant ratios of unknown ligands. This method improves on traditional probe compound methods that indirectly determine redox properties of complexes based on probe compound reduction kinetics.

Finally, MEO was used in conjunction with the previously generated to broadly assess iron-dissolved organic matter (DOM) stability constant ratios. Preliminary results with 3 DOM isolates imply that weak Fe-DOM complexes form at

low pH, while higher pH conditions enable the formation of strong Fe^{III}-stabilizing complexes with low E_H^{Φ}. Although a disadvantage of the method is that it does not allow for precise determination of individual Fe^{II} or Fe^{III}-DOM stability constants, a weaker correlation between measured E_H^{Φ} and known Fe^{III} stability constants of model ligands allows for the estimation of strong Fe^{III}-DOM stability constants, which are similar to other values reported in the literature.

Chapter 1

SIGNIFICANCE, SCOPE, AND STRUCTURE

Electrochemistry studies the interrelation of electrical and chemical effects and has long been utilized in various fields within science, engineering, and medicine to study a wide range of phenomena and devices including corrosion, electrophoresis, batteries, and fuel cells [1]. A unique aspect of electrochemistry is that multiple characteristics of a chemical system, including detection of a species, thermodynamic data, reaction pathways, and electron transfer kinetics, can be deduced from only a single or a few analytical measurements [1]. Additionally, many electrochemical measurements are non-invasive (i.e., they do not destroy the analyte of interest) leading to a clean experimental system that simplifies measurements.

Over the past several decades, electroanalytical methods have led to them becoming increasingly employed in environmental systems [2-5]. Initially, most environmental applications of electroanalytical techniques were constrained to the development of potentiometric ion-selective electrodes (ISE) or polarographic techniques that enabled the detection of trace concentrations of metals and nutrients in aquatic systems, as well as the determination of equilibrium stability constants of environmental metals with ligands and dissolved organic matter (DOM), along with some electrochemical properties of minerals or DOM [6-9].

More recently, an explosion of published studies highlights an increase in the use of electrochemical techniques that have been employed by environmental chemists and engineers [3,4,10,11]. Newer techniques, such as mediated potentiometry and

chronocoulometry, have been used to investigate other electrochemical properties (e.g., redox potential, electron transfer behavior) of both dissolved and solid-phase geo-constituents with greater success [10,11], while the use of techniques such as voltammetry have been expanded to capture dynamic, non-equilibrium behavior of redox-active species *in-situ* in previously inaccessible environmental settings [12-14].

This dissertation primarily utilizes two electroanalytical techniques to investigate a variety of large (macro) and small (micro) scale environmental processes. Voltammetry, the first technique of focus, utilizes a three-electrode setup (working, counter, and reference electrode) to measure the change in currents caused by a redox active substance as measured by the working electrode that result from varying potential in a positive (anodic) or negative (cathodic) sweep [1]. Current response can be standardized to analytes of interest that occur at discreet potentials, enabling electrodes to be used to measure concentrations of redox-active species without disturbing sample matrices or exposing redox-sensitive samples to oxygen during measurement preparation for other methods. Mercury-amalgam (Hg/Au) microelectrodes in particular have been extensively used in the past to measure concentrations of various redox-active species including O_2, Mn(II), Fe(II), H_2S, S^0, Fe(III)-organic complexes, and polysulfides via voltammetry [2,15]. Voltametric microelectrodes are particularly advantageous for environmental studies because voltammograms can capture multiple species (e.g. Fe(II), Mn(II), and H_2S) in a single scan based on the current response that occurs for the species at a given potential [2,15]. Due to their small surface areas (100 um), microelectrodes can be designed to capture redox gradients with high vertical resolution *in situ*, making them an excellent

tool to capture dynamic redox reactions that happen in mm to cm scales in benthic porewaters and water columns while preventing sample alteration [2,15].

Another method used in this dissertation, mediated chronocoulometry, also utilizes a three-electrode system and measures current response. Unlike voltammetry, chronocoulometry experiments are performed at a fixed potential. Experiments are initiated by applying a fixed potential to an electrochemical cell that doubles as a vessel to hold reaction solutions. Because environmental redox kinetics are slow, mediating chemicals are added to facilitate electron transfer to or from the cell, depending on the oxidizing or reducing potential of the experiment [3,4]. After addition of mediating chemicals, geochemical phases, ranging from DOM to redox-active minerals can be added into the cell. Sharp current responses upon addition of geochemical phases to the cell occur due to rapid electron transfer as oxidized or reduced electron mediators are re-reduced or oxidized at the electrode surface [3,4]. Integration of the sharp current responses yields the number of electrons donated or accepted at a given potential (E_H), henceforth the *extent* of reduction or oxidation [11]. Without mediators, peak integration would be impossible due to slow or sluggish electron transfer kinetics at the electrode surface [3]. Mediated chronocoulometry, more commonly referred to as mediated electrochemical analysis (MEA), has been used to measure the redox properties of DOM, clay minerals, iron oxide minerals, and more recently sediments [3,4,11,16,17].

The overall goals of this dissertation were to (1) expand the application of voltammetry to measure redox gradients and elucidate their related biogeochemical processes in a wide variety of field settings, and (2) develop a new method using MEA to investigate redox properties of Fe(II)-ligand complexes in laboratory settings.

In Chapter 2, goal (1) is addressed. Mercury-gold amalgam microelectrodes are constructed and developed in conjunction with a pump profiling system to monitor stratified water columns in Chesapeake Bay [18]. The profiling system is able to measure redox species, along with other collected analytes, with a high vertical resolution that improves on traditional approaches. Redox species gradients and other constituents measured *in situ* in the bay from year-to-year show changes related to spatiotemporal fluctuations in salinity, which controls stratification in the bay.

In Chapter 3, goal (1) was also addressed as voltammetric microelectrodes were again applied to measure the distribution of redox-active species (and their associated terminal electron acceptors) in lacustrine porewaters and an iron seep located around Toolik Lake, Alaska [19]. A heterogenous distribution of redox species in sediment porewaters at various locations throughout the lake indicates the patchy nature of biogeochemical processes in lacustrine sediments. Measurements were also paired with microbiological analysis and suggest that iron cycling between iron oxidizing and reducing (FeOB, FeRB) bacteria influence carbon cycling in the environments investigated. Overall, it can be concluded that microelectrode measurements, when paired with other types of analysis (e.g. microbiological analysis, dissolved organic carbon) are a powerful tool to effectively analyze large scale biogeochemical trends, which is important given our changing climate and highlights the need for future investigations, particularly in the Arctic.

Goal (2) is addressed in Chapter 4, where a previously established electrochemical technique (MEA) is used to investigate the influence of organic ligands on the redox properties of Fe(II). Specifically, mediated electrochemical oxidation (MEO) is employed across different applied redox potentials (E_H) and pH

conditions (i.e., fixed thermodynamic boundary conditions) in order to directly observe Fe(II) oxidation. Fe(II) oxidation plays a key role in biogeochemical cycles that regulate carbon cycling and pollutant dynamics. MEO improves upon traditional probe compound studies that use compound reduction kinetics to indirectly obtain information on redox properties of complexes. Integration of Fe(II) oxidation peaks enabled the calculation of iron(II,III)-complex redox potentials, and a linear Nernstian relationship was discovered between measured reduction potentials of complexes and the ratio of their reported thermodynamic stability constants for Fe(III) and Fe(II).

Finally, in Chapter 5, goal (2) was addressed again as MEO was applied to investigate Fe(II) redox properties in the presence of DOM. Specifically, the Nernstian relationship developed in Chapter 4 was used to estimate the ratio of stability constants for unknown natural complexes with Fe(III) and Fe(II). Preliminary work at pH 4 and 8, along with speciation modeling at pH 4 found the existence of weak and strong complexes in the DOM tested. Using reported thermodynamic stability constants for model ligands enabled the original relationship from Chapter 4 to be split into two separate relationships for estimating thermodynamic stability constants for the complexation of Fe(III) and Fe(II) with DOM. Future work will investigate different DOM isolates that vary in composition, origin, and the way they were isolated (e.g. reverse membrane osmosis, XAD-resin, etc.). Initial results from this study are important because they suggest a new method to obtain stability constants of iron in DOM, which are critical because they control the bioavailability and redox properties of iron. Additionally, these values have previously been shown to be difficult to determine and highlight the broad capabilities of MEA as a technology.

Future research will continue to use both electrochemical methods (voltammetry and MEO) as a tool to investigate large- and small-scale biogeochemical processes. For example, voltammetry can be employed to investigate high resolution (< 1mm) redox gradients in soil porewaters that reveal how manganese drives abiotic carbon oxidation [14]. Additionally, it is expected that paired voltametric, geochemical and microbiological analysis will continue to reveal insights into relationships between biological iron cycling and carbon cycles in the Arctic, where permafrost thaw is shifting carbon and iron cycling dynamics. Indeed, upcoming field expeditions in our lab plan to utilize voltammetry to investigate links between measured geochemical data and microbiological analysis in both North Dakota and in the Arctic. The use of MEO, particularly for observing the influence of ligands on redox properties of iron, is also anticipated to be used in the future, particularly with solid or amorphous iron phases in addition to aqueous Fe(II) [20].The high sensitivity of the method, as well as the developed linear relationships from this dissertation, will allow this method to be applied to a variety of experimental systems to investigate iron redox reactivity. Overall, widescale applications of electrochemistry are likely to increase in environmental fields, of which this dissertation hopes to provide new insights and considerations into their use as a methodology when approaching complex biogeochemical phenomena.

Chapter 2

A DURABLE AND INEXPENSIVE PUMP PROFILER TO MONITOR STRATIFIED WATER COLUMNS WITH HIGH VERTICAL RESOLUTION

This chapter is a reprinted version of an article published in Talanta: "Hudson, J.M., MacDonald, D.J., Estes, E.R. and Luther III, G.W., 2019. A durable and inexpensive pump profiler to monitor stratified water columns with high vertical resolution. *Talanta*, 199, pp.415-424 doi.org/10.1016/j.talanta.2019.02.076."

2.1 Introduction

Stratification and subsequent redox speciation in marine environments can be complex and dynamic. Detection and quantification of redox active species and their gradients are vital for gaining a larger perspective of marine biogeochemical processes [21] Pump profiling systems aboard research vessels and small boats can be utilized for *in situ* chemical analysis and collection of discrete samples for laboratory based analyses at a resolution equal to the orifice of the pump (0.254 m in this paper) in a quite sea state [22-31]. Most CTD systems collect samples using 10 L Niskin bottles, which limits vertical resolution to their 1 m length because water at the bottom of the bottle may not be the same as at the top [29-31]. Many pump profiling systems in the literature report extensive and expensive pump and hose networks to transport water samples to the surface, where samples are collected and analyzed via traditional techniques in shipboard or home laboratories [32-24]. Pump profiling systems shorten the time between sampling events and laboratory analysis and provide a means to obtain environmental data rapidly and without contamination.

Voltammetric microelectrodes, in conjunction with a laboratory potentiostat and a pump profiler system, are an ideal analytical method to measure redox active species. This approach minimizes the cost of pressure housings, connectors and cables for *in situ* electronic equipment. Microelectrodes can be deployed as a cheaper, more durable alternative to other techniques that compliment pumping systems [22-28,35]. Multiple redox species can be detected in a single voltammetric scan including O_2, hydrogen peroxide (H_2O_2), Mn(II), I^-, Fe(II), organically complexed Fe(III), FeS clusters, and reduced sulfur species [35-39]. Microelectrode surfaces are small (100 uM), so permit operations at low currents (nano-amps or nA) and in solutions with lower ionic strengths [38]. Additionally, small electrode surface areas increase sensitivity to redox-active species and allow for fast scans (1-2 V/s) to be made in a matter of seconds because small surface areas decrease the charging current relative to the Faradaic current [38,40]. Microelectrodes are easily transportable [38] and can reduce analytical errors from contamination and handling [38]. Finally, because electrodes allow for the rapid analysis of the water column, they can guide scientists in making decisions with respect to the collection of discrete samples for the determination of other chemical and microbial species by other methods [24-27].

In this chapter, a pump profiling system composed of durable plastics has been constructed for a cost of under $1000 USD and mated with voltammetric solid-state electrodes to detect dissolved O_2 and H_2S in an estuarine water column. The system was designed to be inexpensive and easy to clean so that it can be applied to many different field scenarios. In a quiet sea state, a vertical resolution of 2.54 cm (0.0254 m) can be obtained. Data collected during our cruises were provided with a resolution of 0.5 ± 0.1 meter (error is based on sea state). The profiling system resolution is an

improvement over traditional 10L Niskin bottles, which are commonly found on ships and which have a resolution of 1 meter (the length of the Niskin bottle). The principle redox analytes measured are O_2 and H_2S as they represent oxic and anoxic boundaries in the water column, and can be used to delineate zones where other redox-active trace metals (i.e. Fe(II), Mn(III),Mn (II)) are present [22,26-28,36,39,41]. To demonstrate that the pump profiling system can collect samples without contamination due to O_2 in air, microelectrode O_2 data were compared to data from an *in situ* Clark oxygen sensor that was mounted on a ship's conductivity-temperature-depth (CTD) rosette system. H_2S concentration data are also plotted to obtain full concentration versus depth profiles. O_2 and H_2S profiles were measured from two Chesapeake Bay research cruises (2017, 2018) that demonstrate the system's durable character and enabled us to observe dynamic spatial and temporal changes in the bay. Finally, our pump system allows for collection of large water volumes to determine many other environmentally relevant chemical constituents including nutrients (PO_4^{3-}, NO_3^-, NO_2^-, and NH_4^+), trace metals, organic carbon for DOC analysis, proteins for analysis, and microbes for microbial work [22,24,25]. Nitrite data from pumped samples in 2017 and 2018 are plotted with O_2 and H_2S data to show the versatility of our pump profiler [26].

2.2 Methods

2.2.1 Sampling location

Calibration and field data were obtained from the Chesapeake Bay during two of our sampling campaigns in August 2017 and 2018 at a location (Figure 2.1) below the Chesapeake Bay Bridge ($38^0 58'$ N; $76^0 22'$ W). Deeper basins in the Chesapeake experience anoxia above the sediment water interface during summer months from

microbial degradation of organic matter [22,24-27]. The sampling location responsible for these data, located in the upper bay, is deep (~25 m) and allows for entrainment of higher salinity water from ocean waters during tidal motion [22,24-27,39]. Stratification of the upper bay water and influx of higher salinity water traps anoxic water and prevents mixing, creating an increasing salinity gradient from the surface to bottom waters, as well as distinct anoxic, suboxic, and oxic zones.

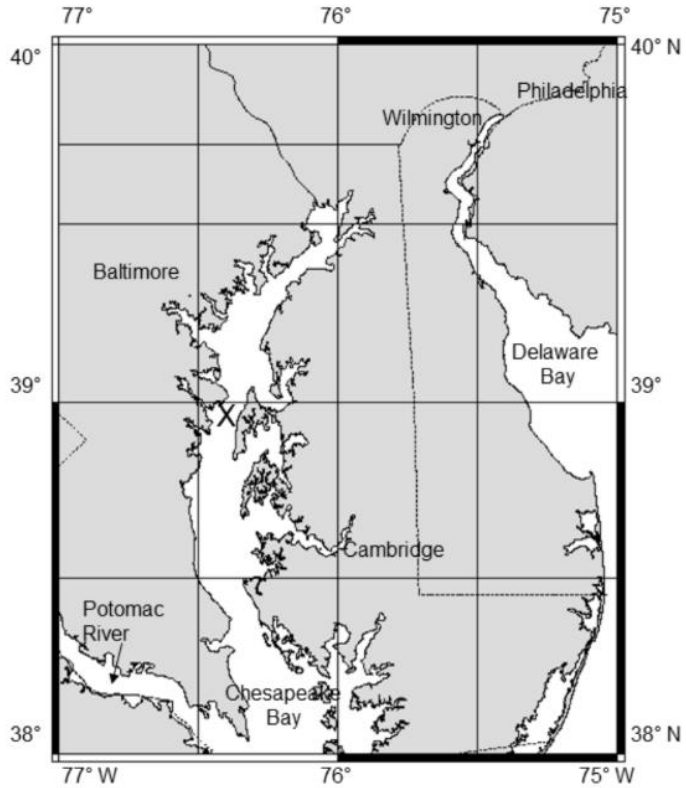

Figure 2.1 Map of sampling location with site X at $38^0 58'$ N; $76^0 22'$ W.

2.2.2 Electrode fabrication

Au/Hg amalgam working electrodes were fabricated according to previous methods [2,15]. BNC cable (Newark Electronics) was stripped down to the copper conductor wire, which was then fixed and soldered to 100 µM gold wire (Alfa). The soldered wire was fixed within 0.125" PEEK™ tubing. With the wire fixed inside the PEEK™ tubing, 105 epoxy (West System) and 206 hardener (West System) were mixed at a 1 part to 4 parts ratio and injected via syringe into the tubing. After hardening overnight, electrode surfaces were sanded and polished using sandpapers with increasingly finer grits (100-1000), and subsequently with diamond pastes (15, 6, 1, 0.25 µm, Buehler).

Following polishing, working, Ag/AgCl reference, and Pt counter electrodes were placed in a 0.1 M $Hg(NO_3)_2$ (dissolved in 0.1 M HNO_3 with a pH ~ 1.0) plating solution purged with N_2. Working electrode gold surfaces were plated by reducing Hg(II) for 4 minutes at a fixed potential of -0.1V. It is important to note that the reference electrode used for plating was encased within a glass frit to prevent Ag dissolution due to the low pH (1.0) of the plating solution. Following electrode plating, a polarization procedure was performed, where the working electrode and Pt counter electrode were transferred to a 1M NaOH solution and held at a potential at -9V for 90 seconds. Finally, working electrodes were run in seawater up to 50 times to ensure electrode functionality and to obtain O_2 signal reproducibility. Multiple electrodes were fabricated, tested, and calibrated aboard the ship before use in sampling.

2.2.3 Pump system

A photo collage of the pump system is shown in Figure 2.2. Water for sampling was pumped shipboard by way of a network of durable tubes (schedule 40 PVC, 1-inch outer diameter, OD), clear PVC tubing and fittings. Tubes and plumbing connectors reduced the initial diameter from 1-3/8'' outer diameter (1" inner diameter, ID) at the sampling end to 1/8'' outer diameter Teflon or polypropylene tubing at the voltammetric sampling cell aboard the ship. The connectors included schedule 40 PVC pieces, bushings (3/4 to ½ "), and NPT fittings, some of which are shown in Figures 2.2 and 2.3. A submersible all plastic bilge pump with a neoprene rotating impeller (12V Model 27DA, West Marine / Rule Industries) at the bottom of the pump system was fastened to the CTD rosette apparatus with hose clamps and/or zip ties (Figure 2.2A,B) The pump orifice was within 5cm of the orifices of other sensors on the CTD whereas the bottom of the Niskin bottles was 40 cm above the sensors. The pump was powered by a 12V marine deep cycle battery (West Marine AGM 105 Amp hr). Here, a 30.5 m 16-gauge extension cord was mated to the electrical wires of the bilge pump by soldering the wires, covering them with heat shrink tubing then encapsulating them with underwater splicing tape (Scotch 23) to be waterproof and connected to the battery. Large 1" ID (1-3/8" OD) tubing (30.5 m of clear high-pressure PVC tubing with 3/16" wall thickness from McMaster Carr #5238K778) was fastened to the pump and secured to the CTD rosette with zip ties and hose clamps. The tubing could be extended with the CTD-rosette system to a maximum depth of 25 meters over which measurements were made. The dead volume of the tubing is approximately 14.7 L, and the pump is capable of flushing the tubing in one minute. Aboard the ship, the tubing was connected to a 3-way or T tube (3/4" NPT at all 3 ports) that had three ball valves (2;3/4" and 1; ½"), which were fastened with an

assortment of fittings to the T tube and that could be reduced on the exit side to other sizes as necessary (Figure 2.2C; see the schematic of parts in Figure 2.3). A 3/4" black ball valve on the bottom of the T tube could be stepped down in size to ¼ or 3/8 inch (using ¾" to ½" bushing plus a Swagelok ½" NPT to ¼ or 3/8" compression fitting adapter), which allowed for sample flow to be diverted for the collection of discrete samples (Figure 2.3). The third part of the T tube utilizes a 1/2" ball valve that was attached to the voltammetry cell with a nylon Swagelok fitting adapter (from ½ inch NPT to ¼ compression) to reduce the tubing size (Figure 2.2D). Furthermore, this ¼" tubing was reduced to 1/8" OD tubing above a sink in the wet lab, where flowing water could be diverted to a 50 ml falcon tube (Figure 2.2E) attached to a ring stand that served as our cell for electrochemical analysis. All tubing reported was either of Teflon or polypropylene grade. As shown in Table 2.1, the entire pump ensemble cost less than $1000, and most supplies were readily obtainable at local hardware, marine and scientific supply stores. An earlier pump profile version [39] from over twenty years ago used a pump from the deck (rather than a submersible pump) that cost $1500 not counting any other parts; part of it was also susceptible to corrosion. Because our system is composed of plastic parts, corrosion is not a problem and the system can be used for trace metal studies [22,26,27].

An oxygen sensor (Clark electrode, SBE Inc.) and fluorescence sensor (Eco-FL Fluorometer, WETLabs) were also part of the CTD Rosette to take measurements during sampling. The system was cleaned with DI water onboard the deck of the ship after deployment. There were no coating effects observed with the pump system.

Table 2.1 Costs of components for the pump profiler are based on January 2019 prices. There are deep cycle batteries that are less expensive; e.g., a West Marine deep cycle flooded marine battery (75 AH) costs $189.99.

component description	**quantity**	**cost each USD**	**total cost**
1100 GPH (4000 LPH) Rule Industries bilge pump (West Marine)	1	69.99	$69.99
West Marine AGM sealed marine battery 105 AH	1	264.98	$264.98
30.5 meter electrical cord	1	38.98	$38.98
30.5 meter PVC clear hose (McMaster Carr #5238K778)	1	337.00	$337.00
PVC ball valve 3/4 inch	2	3.68	$7.36
PVC ball valve 1/2 inch	1	3.08	$3.08
PVC bushings 3/4 to 1/2	2	0.96	$1.92
PVC tee 3/4 inch	1	3.82	$3.82
PVC nipple 3/4 to 3/4 inch	2	0.91	$1.82
PVC nipple 1/2 to 1/2 inch	1	0.55	$0.55
1/2 NPT to 3/8 tube NY-600-1-4 (Swagelok)	2	10.00	$20.00
1 inch OD to 3/4 inch NPT coupling for tee inlet	1	0.53	$0.53
1 inch OD sch 40 PVC inlet to tee (12 ft)	1	6.03	6.03
3/8 OD 1/4 ID polypropylene tubing t-95875-07 (Cole Parmer)[1]	100 ft	103.00	103.00
1/4 OD 1/8 ID polypropylene tubing t-95875-02 (Cole Parmer)[1]	100 ft	63.80	63.80
			$922.86

[1.] Only 6-8 ft of Polypropylene (Teflon) Tubing are needed. If Teflon tubing is preferred for trace metal work, we use FEP tubing (comes in 25 foot sections) from Cole Parmer [3/8 OD; 1/4 ID FEP tubing t-06450-07 ($166) and 1/4 OD; 1/8 ID FEP tubing t-06450-05 ($108)]. Total cost is then $1030.06.

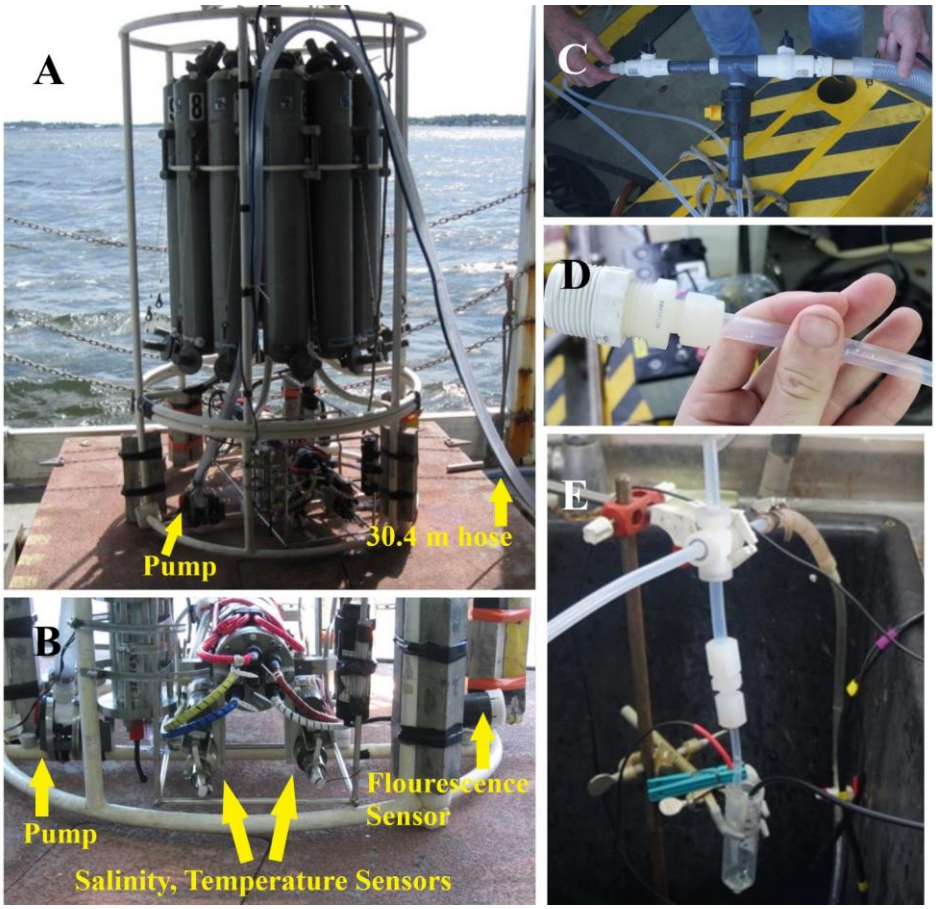

Figure 2.2 A) The pump system is zip tied to the CTD rosette, with the bilge pump (bottom yellow arrow) on the bottom. Tubing (top yellow arrow) connects the pump and structure to the onboard flow cells. B) A closer view of the bilge pump (left yellow arrow) zip-tied to the bottom of the CTD rosette near other sensors, including the salinity and temperature sensors (middle yellow arrows) and fluorescence sensor (right yellow arrow). All orifice inputs are within 5 cm. C) T tube apparatus on deck of the vessel. Flow from the right could be diverted through the T tube for sample collection through the bottom valve or left to the electrochemical cell. A more detailed schematic of the T tube parts is provided in Figure 3. D) ¾" to ½" bushing coupled to a nylon ½" NPT to 3/8" tube fitting leading from the 1/2 " ball valve from the T tube to the voltammetry cell. E) Electrochemical cell. A 50 ml falcon tube is attached to a ring stand. Working, reference, and counter electrodes are placed inside the cell. When pump flow is turned on, sample flows into the cell and continuous real time measurements are made.

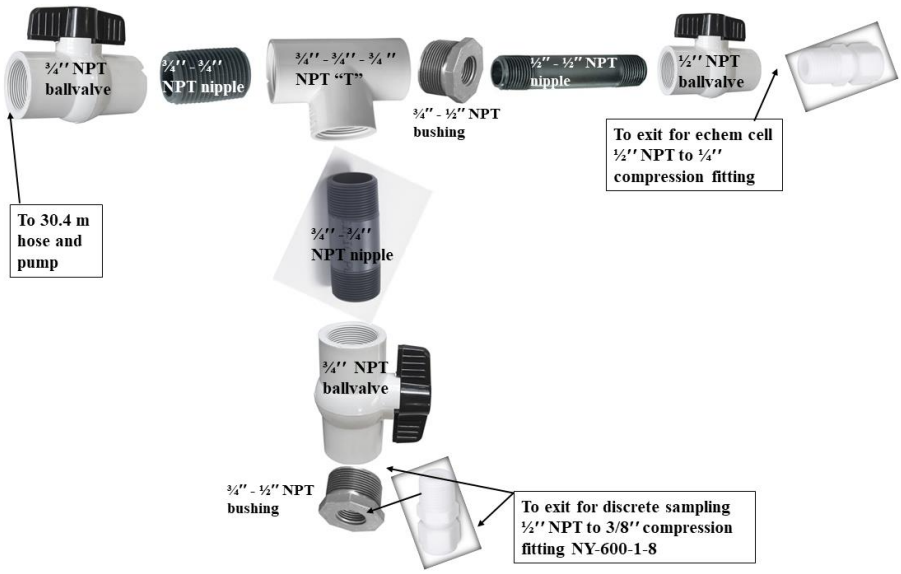

Figure 2.3 Schematic of T-nozzle apparatus for the pump system. Individual NPT fittings and parts are labeled. The inflow end on the left side (connected to the hose and pump), and the outflow end on the right-hand side of the T-nozzle (to the exit for the electrochemical cell).

2.2.4 Experimental procedure

Real time voltammetry was performed by pumping water from discrete depths to the electrochemical cell aboard ship with the pump system for 30-45 min before and after slack tides when water movement was at a minimum. Electrochemical measurements during CTD rosette casts were made at each sampling depth desired. To reduce costs of the electrochemical cell, the working, reference, and counter electrodes were placed in a 50 ml centrifuge tube attached to a ring stand that acted as an electrochemical cell to measure O_2 and H_2S. Water was pumped into the bottom of the tube so that the tube was filled to overflowing levels at least three times prior to any measurement to ensure that no oxygen from air would contaminate the waters (Figure 2.2E; this approach is similar to the sampling of oxygen for Winkler titrations) [34,39]. Electrodes were attached to a potentiostat (DLK 60, Analytical Instrument

Systems, Inc.). Oxygen calibrations were performed concurrently with experiments (see Calibrations). When only O_2 was present, linear sweep voltammetry (LSV) was performed at potentials ranging from -0.1 V to -1.8 V at scan rates of 1000 mV/s after application of a conditioning potential at -0.1 V for 2 sec. For sulfide measurements, cyclic voltammetry (CV) was performed by scanning from -0.1 to -1.8 and back to -0.1 V. For sulfide scans, a 5 second conditioning potential was applied to the working electrode poised at a potential of -0.7 V before sulfide scans to ensure the removal of any reactive redox species that were previously deposited on the electrode surface. Likewise, a 2 second conditioning potential poised at -0.1 V was applied prior to the initiation of all scans. At each depth sampled, multiple scans were performed until scan peaks reached a repeatable current; this took at least one minute, which was the flushing time of the 30.5 m tubing. In addition to electrochemical measurements, samples at discrete depths from the pump system could be collected for lab-based analyses through the other port of the T tube apparatus. After each depth was sampled, the tubing was flushed for 1-2 minutes through the ¾ inch ball valve without the ¾" NPT to 3/8" sampling adapter prior to the next set of analyses and sample collections at a different depth. After a cast was completed, the entire system was flushed for 3 minutes with distilled water from the ship's evaporators and the clear PVC tubing containing distilled water was laid out on the deck in a figure eight configuration for storage. Pump profiling O_2 data obtained with voltammetry were compared with CTD O_2 data. O_2 and H_2S voltammetric methods were known to reliable based on previous intercomparisons [28,38].

Shipboard nitrite determination was performed using the method of Grasshoff (1983) [43]. Two 25 mL sample, 0.5 mL of 58 mM sulfanilamide in 10% v/v HCl and

0.5 mL of a 4 mM N(1-naphthyl)ethylene diamine hydrochloride solution were added. Samples with added reagents were shaken and left to sit for 15 minutes, followed by UV-Vis analysis at 540 nm using a 10-cm cell to increase detection limits. Calibration curves were constructed using sodium nitrite.

2.2.5 Electrode calibrations

Oxygen calibrations were performed during sampling events. To perform a calibration, anoxic samples with nondetectable oxygen concentrations (<3 uM) were first analyzed for sulfide. Upon analysis of the anoxic samples (typically 5 or more scans), the anoxic sample was bubbled with air from an aquarium bubbler (Penn-Plax, Sea Pony) to reach 100% oxygen saturation and to purge H_2S. Upon saturation, LSV scans were then performed and corresponding current amplitudes were measured to obtain a two-point calibration curve (zero current for nondetectable O_2 and measured current for 100% O_2 saturation). While our previous work has shown that it is possible to obtain up to a 6-point calibration curve, it is well known that 2-point calibration curves are reliable and are commonly used [44]. Multiple calibration curves were built per rosette cast to account for changes of salinity and temperature with water column depth, as changes in salinity (i.e. electrolyte concentration in electrochemical cell) and temperature affect electrode response [23,35].

Sulfide calibrations were performed based on previously described methods [28,35,36,37]. Briefly, single $Na_2S \bullet 9H_2O$ crystals were weighed and prepared in sealed glass ampoules. Ampoules aboard the ship were kept in a refrigerator until use for calibrations. 3-10 mM calibration stock solutions were prepared by snapping an ampoule vial and dropping the sodium sulfide crystal into a volumetric flask with N_2 purged DI water.

2.3 Results and Discussion

2.3.1 Oxygen calibrations; effect of salinity changes on electrode response

Electrodes were calibrated in real time during rosette casts. Dissolved oxygen concentrations were lower at depths with higher salinity, therefore current response of the electrode was much lower. Figures 2.4A-E show three calibration scans (LSV) performed during cast 5 (August 4, 2017, 1:24 pm local time) to account for changing salinity. Figure 2.4A shows a scan from an anoxic water sample (23.3 m). After bubbling the sample with oxygen to 100% saturation, discrete O_2 and H_2O_2 peaks (-0.34 V, -1.23 V) were visible (2.4B). The O_2 peak amplitude was 55 nA and was used as a calibration point that represented 100% saturation. For each sample depth, the theoretical concentration of 100% O_2 saturation [C] was calculated using the method of Weiss [42], where T is absolute temperature and S is salinity (Eq. 2.1). A and B terms are volumetric stability constants for the calculation of solubilities from moist air at one atmosphere of pressure [45].

$$ln[C] = A1 + A2 * \left[\frac{100}{T}\right] + A3 * ln\left[\frac{T}{100}\right] + A4\left[\frac{T}{100}\right] + S‰\left[B1 + B2\left(\frac{T}{100}\right) + B3\left(\frac{T}{100}\right)^2\right] \quad (2.1)$$

The 100% O_2 peak height obtained was then plotted vs concentration determined from eq. 1 to obtain a two-point calibration curve, the other peak height being 0 nA for zero O_2. Figures 2.4C and 2.4E show scans before bubbling to 100% oxygen saturation, whereas 2.4D and 2.4F show scans after 100% oxygen saturation. At shallower depths (of decreasing salinity), O_2 currents were measured so 0 nA for zero μM O_2 was assumed based upon the deep samples where O_2 is not detected. As shown in figure 2.5B, although temperature (T) is also a factor governing O_2

solubility, temperatures at all depths in the water column were relatively consistent, making salinity a larger factor in electrode response.

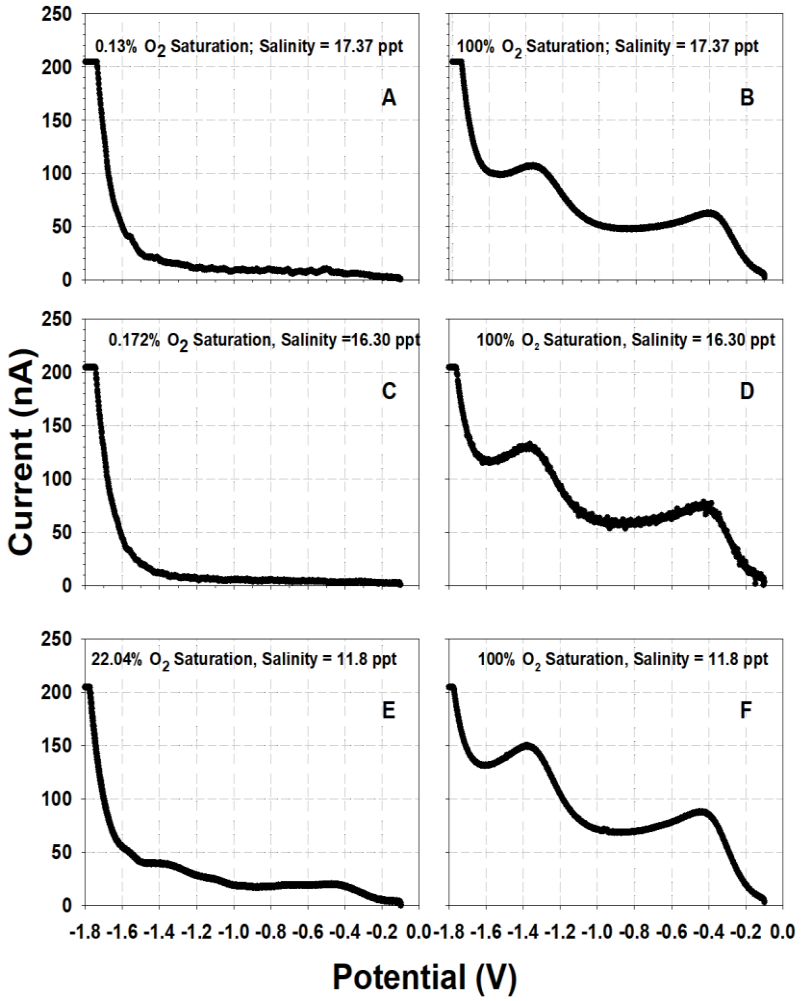

Figure 2.4 O_2 electrode Calibrations performed during sampling. Each row includes the original sample (left) and the sample following bubbling for 100% O_2 saturation (right). A) With decreasing salinity, O_2 concentrations increase, increasing the amplitude of O_2 waves. Scan A shows an anoxic sample (salinity of 17.37‰) B) bubbled to 100% O_2 saturation C) Suboxic sample (salinity of 16.3‰) D) 100% O_2 saturation of suboxic sample E) A sample from the lower-oxic zone salinity of (11.7‰) F) 100% O_2 saturation of sample. All calibration scans were performed using linear sweep voltammetry (LSV) at 1000 mV/s.

2.3.2 Electrode correlation with CTD for O_2 measurements

Microelectrode data from the pump profiling system were correlated with CTD O_2 data. At each sampling depth, an oxygen sensor at the bottom of the CTD rosette took readings of O_2 concentration (µM) and these are taken 1 minute prior to analysis by voltammetry so both measurements can be time correlated properly. Voltammetric microelectrode data are compared to CTD data from cast 5 in 2017 in figure 2.5A. Depths sampled ranged from 23.3 m to 11.8 m. The inset in figure 2.5A shows that values for electrode O_2 concentration are all consistent as a regression of electrode O_2 and CTD O_2 yields a slope of ~1 (1.016; $r^2 = 0.9972$) as expected. Slight deviation is due to the fact that voltammetry measures residual and Faradaic current, whereas the Clark sensor on the CTD does not give a measure of residual current. Salinity and temperature from cast 5 are also provided in figure 2.5B. Measurements were taken over a range of salinities (17.37ppt to 11.8 ppt) that required multiple calibrations. Temperatures were relatively consistent throughout the water column and varied only 0.3 ^{0}C from ~25.70°C to 25.40°C.

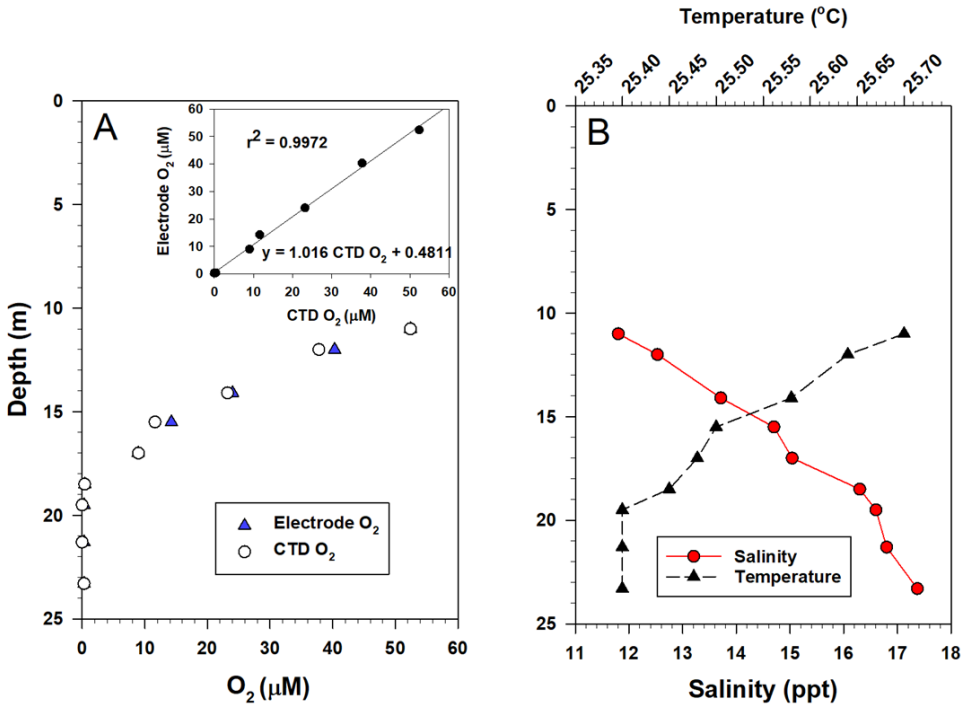

Figure 2.5 A) CTD O_2 and electrode O_2 concentration vs depth is plotted from Cast 5 in 2017 (August 4, 1:24 pm). The inset is a regression of CTD O_2 vs electrode O_2 that shows a slope of 1.016, which indicates agreement between the two methods. B) Salinity and temperature are provided from the same cast. While temperature only varied 0.3 ^{0}C, salinity changed from 17.37 ppt to 11.80 ppt.

2.3.3 Chesapeake profiles using the pump profiler

Full pump profiles of the Chesapeake Bay water column were obtained for both O_2 and H_2S using voltammetry, as well as for nitrite from samples collected with the pump profiler [40]. O_2 and H_2S measurements were obtained rapidly and provided

information for the collection of discrete samples for other dissolved constituents in the water column. As noted above, pump profiling O_2 data are consistent with CTD O_2 data, and H_2S data are also reliable based on previous intercomparisons [27,36]. Figure 2.6A shows a full profile from rosette Cast 10 (Aug 6, 2017, 7:10 am local time) for O_2 and H_2S (obtained by voltammetry), and figure 2.6B shows the salinity and temperature data from the same cast. The anoxic zone is clear at depths ranging from 22.3 meters to 18 meters. At these depths H_2S is present at concentrations up to 19.5 µM at 20 meters (Figure 2.6A). Above this region, a distinct suboxic zone void of O_2 and H_2S is present from sampling depths of 16 to 14 meters. At 13 meters, trace O_2 is present and increases towards the surface. Figure 2.6B shows salinity changes 6 units on descending from the lower part of the oxic zone at 11.5 m to the upper part of the anoxic zone at 18 m. Overall, salinity at 22.3 meters is 19.22‰ and decreased to 7.51‰ at 3 meters of depth. The decrease in salinity from bottom to top illustrates the density-driven stratification of the Chesapeake Bay, with fresher water on top of the saltier water. Temperature at all depths remains relatively consistent, ranging from 29.49 to 29.95 °C.

Temporal changes in Chesapeake Bay water chemistry were able to be monitored by the profiling system. Figures 2.6C and 2.6D show a profile from 2018 (Cast 6, July 30, 9:50 am). There is a notable decrease in H_2S concentrations when compared to 2017 (Figure 2.6A) as the maximum H_2S concentration was only 5.09 µM at 23.18 meters. Chesapeake data in 2018 consistently showed lower sulfide concentrations for all rosette pump casts. As shown in figure 2.6C, O_2 penetrated deeper into the water column in 2018, to ~19 m. The larger size of the oxic zone and smaller size of the anoxic zone could be attributed to a large influx of freshwater (from

many severe summer rain events) into northern Chesapeake Bay from the opening of the Conowingo Dam floodgates along the Susquehanna River, a large tributary located at the northern head of the bay [43]. Indeed, dam floodgates were opened immediately prior to the 2018 research cruise. Freshening of upper bay water was observed via salinity data (Figure 6D), which show the surface salinity at 3m in 2018 as 7.41 ppt, as opposed to 7.51 ppt in 2017 (2.6B). Earlier casts in 2018 had salinity as low as 2.61 ppt at 3m (data not shown). In 2018, the salinity gradient from 18 to 22 meters from the bottom of the oxic zone to the top of the anoxic zone was less than 2 salinity units, but the suboxic zone was again only 2 meters from 19 to 21 meters. Although pump profiler resolution can reach 2.54 cm, which allows for steep gradients to be observed, Figures 2.6A-D show that data collected only every 0.5 to 1.0 m is necessary to characterize the suboxic zone in both years. This is better than what can be achieved with Niskin bottles, where maximum resolution is constrained because of the length of the Niskin bottle (~1 m); water at the bottom of the bottle may not be similar to that at the top of the bottle. A sharp salinity gradient in Figure 2.6D is not observed below a depth of 16.9 m but there is a salinity change of 9 units above this depth in the oxic zone. The salinity increase with depth shows that stratification had developed in 2018, but the penetration depth of O_2 from the freshwater river input was deeper and prevented the buildup of H_2S toward surface waters.

Voltammetric measurements provided rapid analysis of O_2 and H_2S while aiding scientists with sampling decisions for the measurement of other chemical species. Samples were collected in 2017 and 2018 with the pump profiler to measure nitrite (NO_2^-), a nitrogen intermediate that forms under low O_2 conditions [29,44-46]. NO_2^- data are plotted with O_2 and H_2S (Figure 2.6A) and show that NO_2^- increases as

O_2 concentration decreases at the top of the suboxic zone, then decreases in the suboxic zone due to denitrification and in the anoxic zone, as it reacts with sulfide. This behavior has been shown previously in other low oxygen environments such as the Black Sea, which has a larger suboxic zone (as much as 40 m) [29]. In 2018, NO_2^- data (Figure 2.6C) again increases as O_2 concentration decreases at the top of the suboxic and bottom of oxic zone. However, NO_2^- concentration ranges in 2018 are much lower (less than 1.7 µM) than in 2017 (>6 µM in the oxic zone). This again can be attributed to higher O_2 conditions that enhance nitrate formation over the formation of this nitrogen intermediate. Fluorescence data in figures 2.6B and 2.6D indicate that the upper water column has a maximum fluorescence. The highest fluorescence data also match the highest oxygen concentration. Chlorophyll, which is the major analyte measured by the fluorescesence sensor, is an indicator of primary productivity, so an increase in fluorescence indicates an increase in primary productivity by phytoplankton, which produces O_2 at photosystem center II [47].

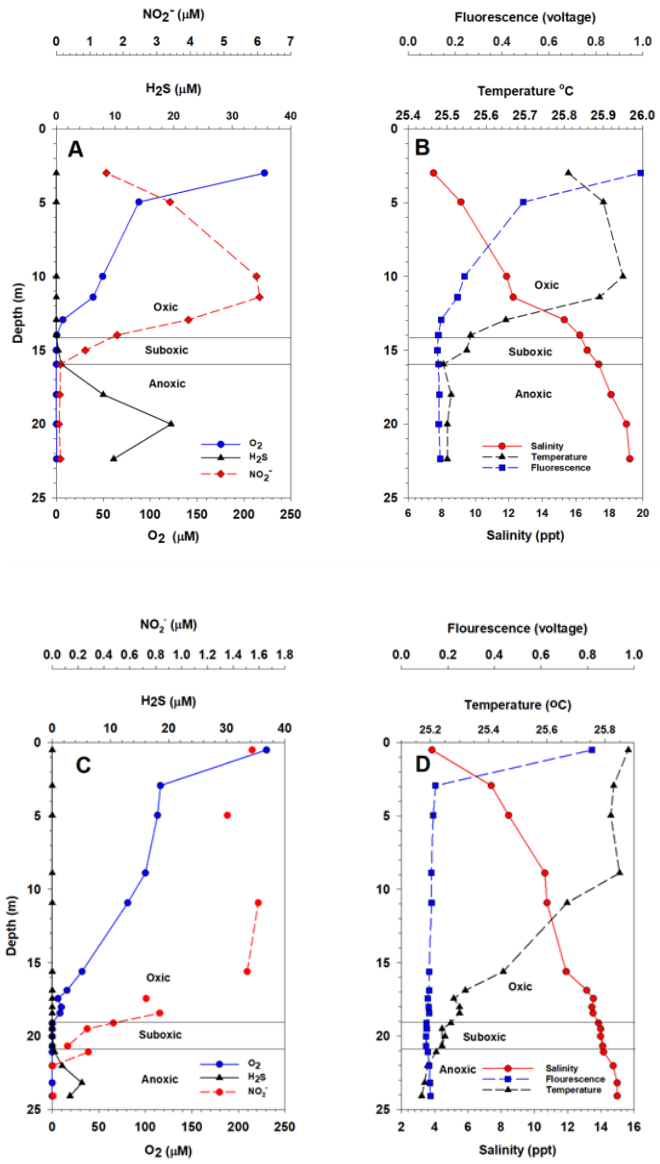

Figure 2.6 Full profiles of O_2, H_2S, NO_2^-, fluorescence, temperature, and salinity plotted vs. depth. A) Cast 10 (Aug 6, 2017, 7:10 am local time) plot of O_2, H_2S, and NO_2^-. B) Cast 10 plot of fluorescence (voltage), salinity (ppt) and temperature (°C). C) Cast 6 (July 30, 2018, 9:50 am local time) plot of O_2, H_2S, and NO_2^-. NO_2^- was not sampled/measured at all depths. D) Cast 6 plot of fluorescence, salinity and temperature. A depth resolution of 0.5 meters was chosen to better characterize the anoxic to suboxic to oxic transition zone for figures 2.6C,D.

2.4 Conclusions

A durable and inexpensive pump profiler for measuring dissolved electroactive redox species in real time and for the collection of samples for other environmental purposes has been presented. The pump profiling system utilizes an inexpensive plastic bilge pump powered by a 12V battery to transport samples from discrete depths to deck surfaces in one minute. Voltammetric analysis of the pumped samples is performed in a 50 ml plastic centrifuge tube using Au/Hg solid-state microelectrodes. Our pump profiling method is accurate, as voltammetric O_2 data correlate well with CTD Clark sensor O_2 data. High resolution water samples can be collected for other species [13,23-26], including nutrients (NO_2^- in this work), dissolved organic carbon, dissolved inorganic carbon, pH, proteins, and microbes with better resolution than using Niskin bottles.

The pump profiler, equipped with a laboratory potentiostat, is portable enough to be used in other environments such as lakes (off docks and other platforms) and not constrained to use aboard research vessels. We have made a smaller and simpler version of the pump profiler to be used off small boats in up to a 6 meter water depth that does not require a winch (Figure 2.7). The smaller system uses a pump that has the orifice outlet immediately stepped down from 1 inch to 3/8 inch for 3/8 inch Teflon or polypropylene tubing, but with no “T tube” (~0.14 L total tubing volume; ~2.5 L min rate). A smaller 12 V battery is used for power as smaller volumes of water are pumped up for collection or to a cell for voltammetry and other sensors as desired. The tubing and power cord are attached with plastic zip ties to one inch OD schedule 40 PVC pipe, which is made into 1 or 2 meter sections that can be attached with screw couplings for easy (dis)assembly and storage. The PVC tubing has markings for every 5-10 cm and is lowered into the water. Hand held sensors (e.g.,

salinity and temperature) with long cables can also be attached to the schedule 40 PVC tubing with zip ties.

Finally, the pump profiling method is durable and extremely affordable. Including all components, the entire cost of the pump profiler system is under $1000 making the system extremely affordable compared to previous pump profiling methods [29,30,48,49]. The smaller profiler has a cost of around $250.

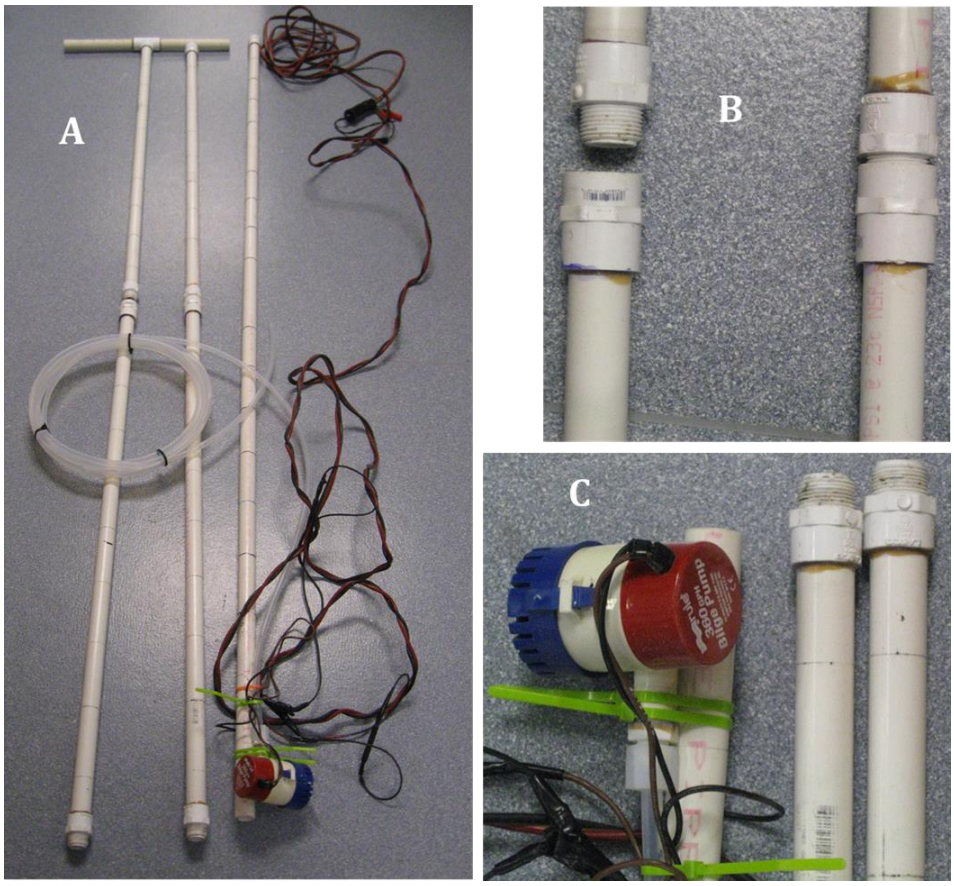

Figure 2.7 A) Small boat pump profiler with 2, 2 meter extensions and 2,1 meter extensions. B) Closeup of screw couplings. C) Closeup of the pump with 3/8 inch Teflon tubing attached to the extension.

Chapter 3

SPATIAL DISTRIBUTION AND BIOGEOCHEMISTRY OF REDOX ACTIVE SPECIES IN ARCTIC SEDIMENTARY POREWATERS AND SEEPS

This chapter is a reprinted version of an article published in Environmental Science: Processes and Impacts: "Hudson, J.M., Michaud, A.B., Emerson, D. and Chin, Y.P., 2022. Spatial distribution and biogeochemistry of redox active species in arctic sedimentary porewaters and seeps. *Environmental Science: Processes & Impacts*. DOI: 10.1039/d1em00505g"

3.1 Introduction

Benthic processes in lacustrine environments of the Arctic are pivotal in controlling important biogeochemical processes such as the emission of CO_2 [50,51] and methane [52-54]; metal and nutrient cycling [55,56]; and contaminant attenuation [57]. Redox active species, such as Fe(III), play an important role as terminal electron acceptors (TEA) in organic matter mineralization in lacustrine sediments given their ability to exert influences on methanogenesis if sufficiently abundant for utilization by Fe-reducing microorganisms [58,59]. Fe(III) reducing bacteria can suppress methane production by outcompeting methanogens due to the thermodynamic favorability of using Fe(III) as a TEA as opposed to less energetic TEAs used in methanogenesis [58,59]. Similarly, organic matter oxidation by other TEAs such as oxygen and Mn(IV) solids may also influence the cycling of carbon in Arctic lakes by acting as an alternative electron acceptor [60,61]. Conversely, enzymatic activity by aerobic microbes or abiotic reactions involving oxygen and Fe(II)-mediated (Fenton)

pathways may promote organic matter mineralization, enhancing methanogensis [50,62-64].

Currently, little is known about the spatial distribution and abundances of important redox active species in sediment porewaters from Arctic lacustrine systems due to the logistical challenges of conducting measurements in these remote and extreme environments. Previous studies in the Arctic that include spatial distribution and abundance of redox-active species have indicated great heterogeneity of TEA distribution and methane generation between lakes and within lakes that make it difficult to understand carbon cycling on larger scales [54,58-61]. Further, these data rely upon the analysis of redox sensitive substances using *ex situ* methods, which are invasive, reflect a composite sample from specific depth intervals, and are subject to the alteration of native redox conditions, especially when transported outside the field location [61,65,66]. As such there exists very sparse benthic porewater redox data for Arctic lacustrine environments due to their inaccessibility, and a significant knowledge gap remains with respect to the spatial distribution of key redox-active species such as iron, sulfur, and manganese. Given the important role of Arctic lacustrine environments in carbon cycling and the disproportionate way this region is affected by a rapidly warming climate, understanding biogeochemically mediated redox processes will advance our understanding of the carbon cycle in the Arctic.

Voltammetric microelectrodes have been used to measure redox-active species in a broad range of marine and estuarine environments ranging from the water column and sediments [15,67] to hydrothermal vents [2,68,69]. They have been less commonly applied in lacustrine systems and/or coupled to concurrent microbial analyses of the sediments [13,34,70-73]. These complementary approaches could help

link the observed porewater geochemistry of TEAs to the microbial activity responsible for the observations. Voltammetric microelectrodes are advantageous because they can achieve high vertical resolution (mm to cm scale) in both sediment cores and the overlying water, while minimally disturbing the sample matrix [13,18,34,73]. Additionally, they can quantify multiple redox-active species (e.g., O_2, Fe(II), Mn(II), reduced sulfur species), and identify Fe(III)-organic complexes that exist as stable chelates under reducing conditions simultaneously without or minimally altering their native oxidation states [15]. This enables us to rapidly analyze and quantify porewater chemical species as a function of depth and, more importantly, measure the redox-active species in their *in situ* redox state [2,13,15,18,70]. Finally, microelectrodes are robust, relatively inexpensive, and can be coupled with Bluetooth enabled portable, battery-operated potentiostats. These attributes make this system amenable to a wide variety of field applications [2,13,15,18,41,68]. Our goal was to quantify redox-active species associated with O_2, Mn and Fe TEA in high, vertical spatial resolution (mm) in Toolik Lake sediment porewater and a microbial iron mat adjacent to the Oksrukuyik Creek (both in Arctic Alaska). Further, we coupled our voltammetric measurements with 16S rRNA gene sequencing to assess how geochemical gradients are influenced by the composition of the microbial communities at our sites. We hypothesized that shallow cores near the perimeter of Toolik Lake would exhibit different redox species distributions (i.e. TEAs) than deeper sediments, based on evidence from previous studies that indicate increased organic matter loading around the Toolik Lake perimeter [74,75]. High-resolution *in situ* measurements of TEAs along geochemical gradients coupled to genomic analyses

across various lacustrine environments enable us to better understand the linkages between biogeochemical redox processes and the cycling of carbon.

3.2 Materials and Methods

3.2.1 Field sampling and experiments

Sediment cores were collected at Toolik Lake, Alaska (68°38′N, 149°43′W, elevation 760 m), an Arctic Long Term Ecological Research (LTER) and National Ecological Observatory Network (NEON) site (Figure 3.1a., b.). The Toolik Lake watershed lies north of the Brooks Range and is characterized by continuous permafrost with a shallow (~50 cm) active layer. Due to low temperatures and input of nutrients, Toolik Lake is oligotrophic, supporting slow rates of organic matter deposition and decomposition with sediments rich in manganese and iron [61]. Cores collected (6) were divided into shallow cores (STL9, STL10, NETL8, ETL10) vs. two paired deep lake cores from the same site (STL15) (Figure 3.1; Figure A.6). Cores from two sites, one in shallow (9 m) water (STL9) and deeper (15 m) water (STL15) were taken from the southwest side of Toolik Lake and are the focus of our study [61]. Coring was conducted from a boat using a gravity corer (Pylonex AB) with a polycarbonate core liner. Following core recovery, cores were transferred to a shore-side laboratory at Toolik Field Station (TFS) and partially extruded until at least 3 cm or more of water was left at the top of the core to preserve the sediment-water interface (SWI), and for placement of the counter and reference electrodes (Figure A.1).

Redox profiling of an iron seep adjacent to the Oksrukuyik Creek (Figure 1b.,c.) was conducted *in situ* at the site. Steel supports were laid across the ~0.75 m

wide and 0.8 m deep pool of water (Figure A.2). A ring-stand was placed on the platform and supported both a potentiostat (details provided below) and a micromanipulator (Narishige), which held an Hg/Au-amalgam working electrode (description below and Figure A.3). The counter and reference electrode were securely fastened to the platform with electrical tape so that they were held in the surface water. A Bluetooth connection enabled communication between the potentiostat (Metrohm Dropsens µStat-400) and the controlling computer, which optimized working conditions. Water column parameters were measured with a hand-held field multimeter (O_2, pH, temperature, conductivity; YSI). The O_2 electrode was calibrated with a two-point calibration curve using 100% air saturated lake water and a 0% O_2 solution of 1M sodium ascorbate and NaOH. The pH probe was calibrated using a 3-point calibration curve of certified pH buffers at pH 4, 7, and 10.

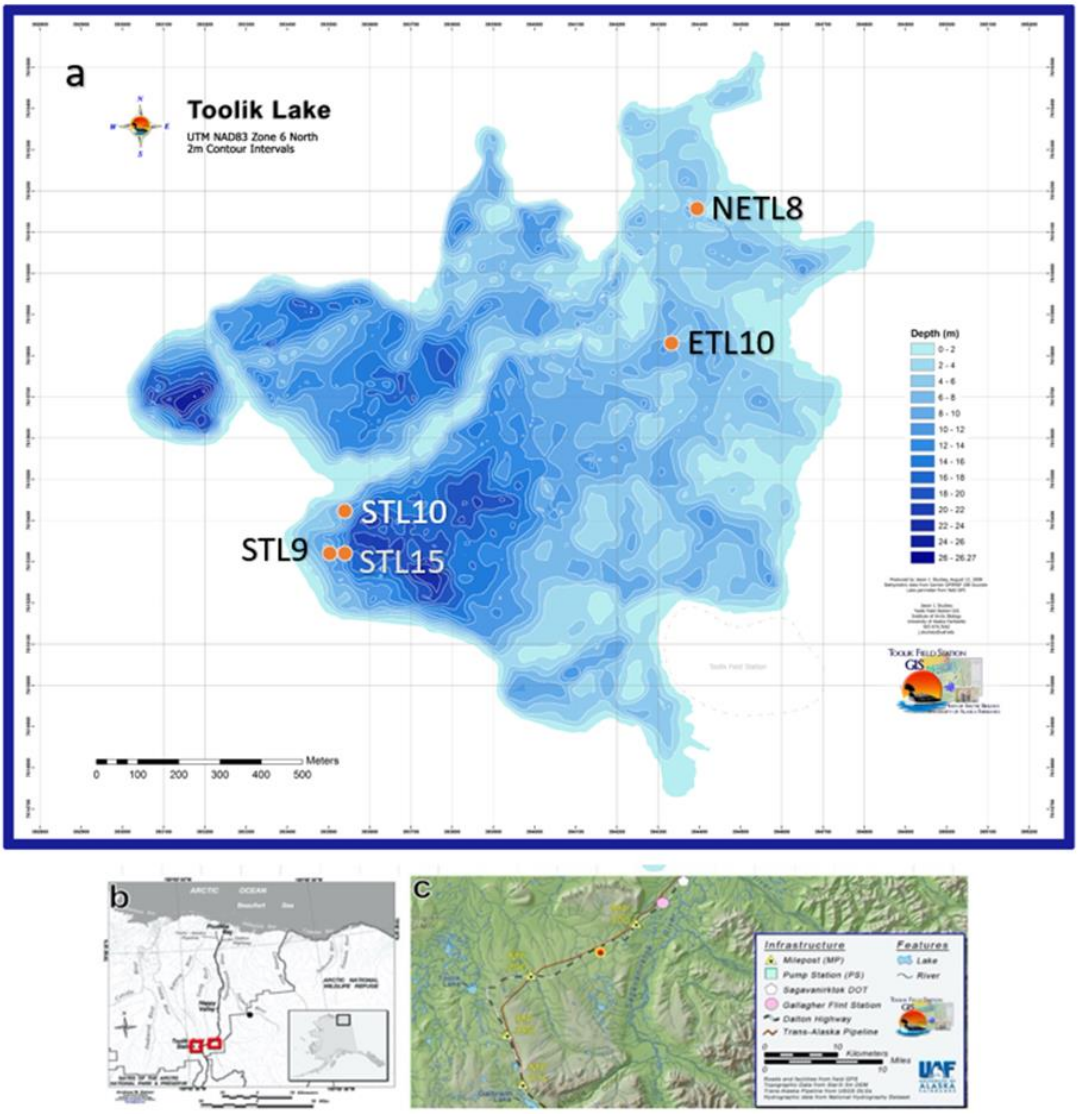

Figure 3.1 Bathymetry map of Toolik Lake and sampling locations near Toolik Lake research field station (a). Overview of the North Slope of Alaska, showing the location of Toolik Lake in the left square and the Oksrukuyik Creek iron seep site in the right red square (b), with a detailed view of the Oksrukuyik Creek iron seep site within the Oksrukuyik watershed (c).

3.2.2 Voltammetric analyses

Electrochemical scans were completed using the potentiostat coupled to a three-electrode configuration comprised of a gold-amalgam (Hg/Au) working

electrode, Ag/AgCl reference electrode (BASi, West Lafayette, IN), and Pt-wire counter electrode (BASi). Working electrodes were fabricated in our laboratory at the University of Delaware and are identical to ones used in earlier marine studies [2]. Based on previous sediment work in our group [34], we opted to use PEEK-based material for our microelectrode sheath fabrication, which is much more robust and easily transported to our remote field site than capillary glass microelectrodes. Calibrations for O_2, Mn(II), and Fe(II) were done in unfiltered Toolik Lake water prior to use in the field. Details regarding the construction and calibration of the electrodes can be found in the Supporting Information (SI). Both Ag/AgCl reference and Pt counter electrodes were attached along the top of the core liner so that they were submerged into the overlying water above the sediment interface (Figure A.1). The Hg/Au-amalgam working electrode was then fastened securely to a micromanipulator above the core liner allowing it to be manually lowered into the overlying water and sediment at mm resolution (Figure A.1).

Measurements of redox active species in the cores were initiated by placing the working electrode in the overlying water near the sediment/water interface in the core and working down the core in millimeter to centimeter intervals, based on transition areas within biogeochemical gradients, (i.e., higher resolution (mm) measurements were made closer to the SWI, which represents the region of greatest change in redox speciation). At the iron seep, measurements were made in the overlying surface water at centimeter intervals. Near the water-iron mat interface, measurements were made at millimeter intervals into the mat, and then again at larger intervals once the electrode was deeper in the mat.

Scans for both the cores and the iron seep were performed using cyclic voltammetry (CV) at scan rates of 1000 mV/s from -0.1 V to -1.8 V to -0.1 V (vs. Ag/AgCl). A fast scan rate was chosen to increase the sensitivity of the measurement [15]. Three distinct, quantifiable redox-active dissolved species were measured in the cores: O_2, Fe(II), and Mn(II). O_2 occurs at a higher potential (around -0.33 V relative to Ag/AgCl) and presents as the first broad peak on the cathodic scan as it is irreversibly reduced at the amalgam surface of the electrode (Figure A.4). Fe(II) and Mn(II) occur at lower potentials around -1.4 V and -1.55 V, respectively, and appear as broad shoulders as they are reduced and deposited onto the electrode surface (Figure A.4B and D). For Fe(II) and Mn(II) measurements deeper in the core, conditioning steps were employed by holding the working electrode poised at -0.8 or -0.7 V for 10 to 40 seconds to remove any previously deposited redox active species. Conditioning steps were not used for O_2 measurements, as potentials lower than -0.1 V would partially reduce O_2 to form reactive oxygen species (ROS) [15]. The limit of detection for O_2, Mn(II), and Fe(II) with our electrodes was 3, 5, and 5 µM, respectively. Depending on the location and redox-state of the core, other redox-active species were present, including Fe(III)-organic complexes that occurred as broad peaks at higher potentials ranging from -0.1 to -0.8 V (Figure A.4C and D). Fe(III)-organic signals could not be calibrated, as the specific complexes responsible (mostly oxygen-containing, carboxylate-type ligands) for the signal are unknown [2,15,67,70]. We did not detect any reduced sulfur substances in any of the samples, which most commonly can include H_2S that shows a peak at -0.6V in voltammograms, and $FeS_{(aq)}$ in the form of molecular clusters, which occurs as a shoulder at -1.15V [67]. This is not surprising, as Toolik Lake and its watershed is generally devoid of sulfur [61].

Reduced sulfur species have been shown to decrease or eliminate voltametric Fe(III)-organic signals via reduction in strongly reducing conditions [76]. Scans were performed 4 to 5 times at each discrete depth, and total analysis time for one depth was about 1 to 3 minutes.

3.2.3 *Ex Situ* iron analysis

Ex situ measurements of Fe(II) concentrations from the iron seep were made from the overlying water collected using a Rhizon membrane filter (0.2 µm) sampling device. This measurement was made to compare the voltammetric assays to more common *ex situ* methods (Figure A.5) [66]. The 5-cm long filter section of the Rhizon was placed vertically in the top 5 cm of the water overlying the Fe(III)-oxide mat of the iron seep. The water was pulled through the Rhizon by connecting a 10 mL syringe and applying a vacuum. The first 0.2 mL of water was used to rinse the Rhizon and discarded, then 2 mL of water was allowed to flow into the syringe. After the 2 mL sample was collected into the syringe, 1 mL of water was immediately transferred to 0.1 mL of 10 M HCl to yield a ~1 M HCl and a low pH sample matrix thereby preventing any further oxidation of Fe(II) [77]. The Ferrozine assay [32] was used to quantify Fe(III) and Fe(II). Briefly, samples for Fe(II) were combined 1:1 with the Ferrozine reagent and quantified using a 6-point standard curve. Fe(III) was calculated by measuring the total Fe in the sample by pretreating a separate aliquot 5:1 with 10% hydroxylamine hydrochloride for 30 min in the dark. Total iron was calculated from a separate 6-point standard curve and Fe(III) calculated as the difference between Fe(II) and total Fe. We did not collect porewaters from our Toolik Lake sediment cores for Fe(II) analysis, as our liners lacked the predrilled ports needed for the Rhizon samplers.

The pool of solid-phase, microbially-reducible Fe(III)-oxides was quantified by adding a known amount of Toolik Lake sediment to a 15 mL centrifuge tube, then adding 5 mL of 0.5 M HCl and incubating at room temperature (21ºC) on a shaker table (30 RPM) for one hour in the dark [65]. After one hour of incubation, the tubes were centrifuged at 3600x*g* for 5 min at 10ºC to pellet the sediment. One milliliter of supernatant was pipetted into a clean 2 mL centrifuge tube. The Ferrozine assay was used to quantify the Fe(II) and Fe(III) in the extraction solutions [32]. All reagents for the Fe extractions were made with glassware that was washed with 2% oxalic acid, then 1% HCl, and rinsed six times in distilled deionized water. The handling of sediment during the extraction process was conducted inside a portable glove bag flushed three times its volume with N_2.

3.2.4 Microbiological sampling and molecular analysis

A separate, paired core at site STL15 was sampled and analyzed for the consortium of microbiological communities associated with redox gradients present in the porewaters. The overlying water was pipetted off the top of the sediment core and the sediment core was extruded until the sediment surface was even with the top edge of the core liner. The surficial orange flocculant layer was pipetted into a 15 mL sterile tube using a sterile cut-off pipette tip and immediately frozen at -20°C. The core was then extruded upward 0.5 cm and sediment was collected from the center of the core using a metal spatula flame-sterilized with 100% ethanol. Again, the sediment was placed in a 15 mL sterile tube and frozen immediately at -20°C. This process was repeated for the 1-1.5, 2-2.5, 3-3.5, 4-4.5, 5-5.5, and 6-6.5 cm depth intervals. The microbial iron mat along the banks of the Oksrukuyik Creek was sampled using a sterile 25 mL serological pipette to aspirate the top 1 cm of mat material, which was

then transferred into a 15 mL sterile tube and frozen. Samples were shipped frozen (-20ºC) to the Bigelow Laboratory for Ocean Sciences. DNA was extracted using the DNeasy PowerSoil kit (Qiagen) with slight modifications for the high iron content of these sediments [56]. Briefly, 200 µL of bead beating solution was pipetted out of each bead beating tube, then 0.25 mL of thawed sediment was pipetted with a cut-off pipette tip into the bead beating tube along with 200 µL of phenol-chloroform-isoamyl alcohol (PCI; 25:24:1). The manufacturer's protocol was followed after the addition of PCI. Extracted DNA was stored at -20°C until it was sent to Integrated Microbiome Resources (Dalhousie University, Halifax, Nova Scotia, Canada) where it was amplified with the 515F/926R primer pair (V4-V5 region of the 16S rRNA gene sequence) before 250 bp paired-end Illumina sequencing. Raw sequences were assembled, quality controlled, clustered, and classified using mothur [78]. Specifically, assembled sequences with ambiguous bases, homopolymers longer than 8 nt, or those contigs with more or less basepairs than expected from the primer pair were discarded. Chimeric sequences were removed with VSEARCH. Clustering of operational taxonomic units (OTU) was done at the 97% similarity level. All samples were subsampled to the lowest number of sequencing reads (n=21264) of the samples in this dataset. Taxonomic assignment of each OTU was made using the SILVA database v138 (release date 16 Dec 2019) [79], curated for the specific region of the 16S rDNA gene sequence used here (V4-V5). We collated OTUs that were taxonomically-assigned to families which contained known iron-oxidizing and iron-reducing bacteria, methanogenic archaea, and methane-oxidizing microorganisms. Then, the relative abundances of these functional groups were summed within each depth interval. Please see the github website (https://github.com/abmichaud) for the

mothur and R code used to process sequence data. These sequence data are deposited in the short read archive under project accession number PRJNA658085 and PRJNA769663.

3.3 Results and Discussion

3.3.1 Redox active species in Toolik Lake sediment porewaters

We observed O_2, Mn(II), Fe(II), and Fe(III)-complexes in Toolik Lake porewaters in our CV scans from all our cores (Figure 3.2 and A.4, A.6), indicating both Fe(II) oxidation, as well as nonreductive dissolution of Fe(III) solids, and reductive dissolution of Fe(III) and Mn(IV) solids [70]. In all cores, voltammetric O_2 peaks were distinctly visible around -0.33 V in the water column above the SWI (Figure A.4). O_2 concentrations vary from saturation (~280 µM) in the overlying water of each core to below the detection limit within the first millimeter to centimeter of depth in sediments (Figure 3.2, Figure A.6). We did not detect any of the reduced metal species (Fe(II) or Mn(II)) in the overlying water of any core (Figure 3.2, Figure A.6) and found little or no vertical overlap between O_2 and reduced metals (Fe(II) and/or Mn(II)) in all cores, which indicates degradation of organic matter by alternate TEAs with increased depth and decreasing favorable free energy, which supports established sediment diagenesis models [80]. Analysis of all cores show that shallow cores located near the lake perimeter (STL9, STL10, NETL8) were highly reducing with little to no O_2 detected below the SWI and more diversity of reduced metals with core depth, while deeper sites and/or cores located further from the shore (STL15, ETL10 respectively) revealed greater O_2 penetration and somewhat less diversity in the reduced metal concentrations as a function of sediment depth (Figure A.6).

Further, at the shallow Toolik STL9 site, O_2 concentrations in the water column *above* the sediments (at ~ 12 mm above the SWI) were slightly undersaturated (< 200 µM: Figure 3.2a.) while oxygen levels in the deep-water site were at or close to saturation (Figure 3.2). At the sediment water interface of STL9 (2 mm above to the interface), O_2 decreased approximately 87.5 µM/mm as a function of depth. This rapid decrease in O_2 concentration below the SWI suggests higher inputs of allochthonous organic matter from the lake perimeter, as observed by others [54,61,74,75]. Further, based upon the reported very low rates of sedimentation observed in Toolik Lake (from a few to < 8 mg/cm^2/year) [60] we believe that inputs of additional metal oxides and organic matter from the pelagic zone to sediments does not fuel this consumption of dioxygen at the SWI. Finally, O_2 did not decrease as noticeably (14.3 µM/mm) in STL15, suggesting that the organic matter at our deeper site is less abundant and/or more refractory in composition.

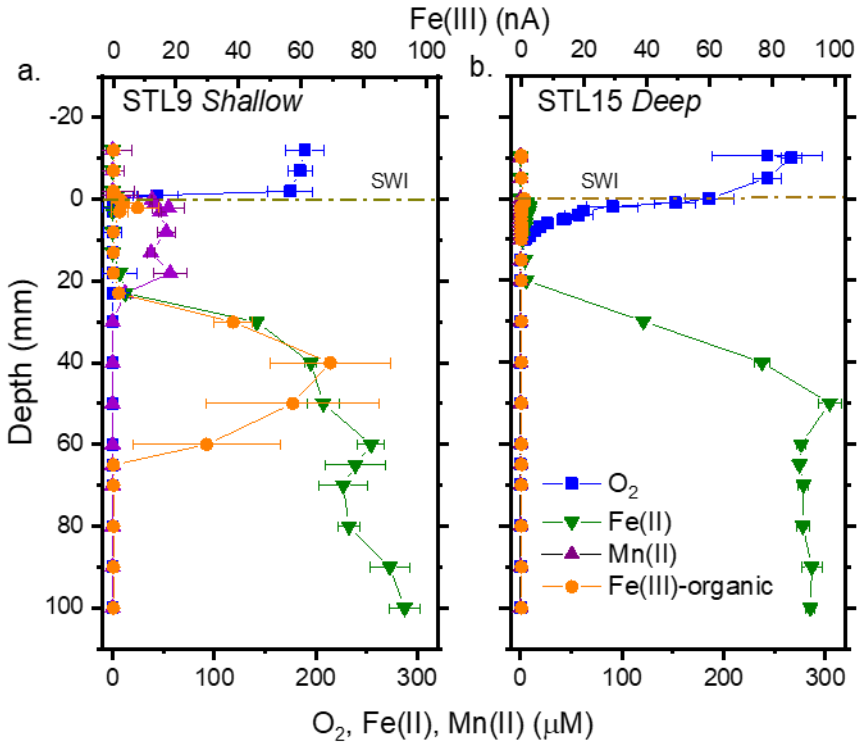

Figure 3.2 Profiles of O2, Mn(II), Fe(II), and Fe(III)-organic complexes (Fe(III)-organic) in STL9 and 15 from Toolik Lake. Note that Fe(III) is plotted only as an average of current response (nA) that is represented on the top x-axis. No error bars were included for current response. For all other species, error bars represent one standard deviation from the mean of three or more measurements and are sometimes smaller than the data point font size. The sediment water interface is abbreviated SWI.

Fe(II) and Mn(II) voltammetric peaks occurred at a potential of -1.43 V and -1.55 V, respectively, in the reduced porewaters (Figure A.4). Fe(II) and Mn(II) distributions in these sediment porewaters correspond to their expected free energies whereby manganese oxides are more thermodynamically favorable relative to iron oxides [80]. In STL9 Mn(II) appears in the surficial (~20 mm) sediment, and porewater Mn(II) concentrations increased from 0 to 39 µM at the SWI, reached a maximum of 57 µM at 18 mm of depth in the sediment, then sharply decreased to

below the detection limit through the rest of the core (Figure 3.2a.). While the decrease in Mn(II) is similar to sediment porewater profiles observed in other freshwater lakes [70,81], it is surprising given that there are no known sinks for Mn(II) under anoxic conditions below where Mn(III) can exist as organic complexes [82]. Carbonates at Toolik Lake are not present in sufficient quantities to influence the precipitation of the major redox species under reducing conditions [83]. One possible explanation is that diffusing Mn(II) from deep sediments accumulates near the SWI (upper 20 mm), as deeper O_2 penetration can act as a barrier for Mn(II) diffusion. Further, Mn(II) has slower oxidation rates with O_2 thereby facilitating accumulation in this sediment zone [70,81]. Because we are close to the limit of detection for Mn(II) in this core (~10 µM) we suspect that Mn(II) is present, but in quantities not detectable by our microelectrode. Mn(II) was also detected at much higher concentrations in the other shallow sediment cores (SI Figure A.6). In contrast to STL9, Mn(II) concentrations increased with depth, but concentrations varied widely (from 10's up to 800 µM) and reflects the heterogenous nature of TEA in the sediments of Toolik Lake.

Fe(II) was not present at detectable concentrations in the top cm of STL9 but increased significantly in concentration downcore. Concurrent low Fe(II) concentrations in the presence of Mn(II) in the top cm of STL9 could indicate inorganic Fe(II) oxidation by MnO_2, which would lead to the formation of fresh Fe(III)-oxides [70]. Additionally, a broad Fe(III) peak occurred at potentials ranging from -0.4 to -0.8 V and corresponds to Fe(III)-organic complexes (Figure A.4). The presence of these Fe(III)-organic complexes has been observed in anoxic sediment porewaters of both estuarine and freshwater wetlands and is attributable to the existence of organic ligands capable of stabilizing Fe(III) under reducing conditions

[84-86]. Because we could not quantify the Fe(III)-organic complexes due to the unknown composition of the responsible ligands, the values are reported as current generated (nA). These ligands are presumably comprised of functional groups (e.g., carboxylates and phenolates) known to stabilize Fe(III) under anaerobic conditions[86] and are ubiquitous in dissolved organic matter (DOM) [87-89]. Surprisingly, these Fe(III)-organic complexes were not observed in every core (Figure A.6), which again reflects the highly heterogeneous spatial nature of benthic porewater redox species, and it is unclear what biogeochemical processes control the existence of these Fe(III) stabilizing ligands.

In the only deep water core sample taken (STL15 Toolik located off the western shore of the lake), O_2 and Fe(II) were the only redox-active species detectable (Figure 3.2b.), although it is possible that Mn(II) existed below our electrode detection limit. O_2 in the water column decreased from 280 µM in the overlying water to 200 µM at the SWI, but unlike STL9, O_2 was observed *below* the sediment-water interface in the first 10 mm of the sediment column after which it became anoxic. Indeed, at this site the surface sediment had a distinctly orange hue, which is likely due to the presence of iron oxides (Figure 3.3B, Figure A.7). Fe(II) was present at detection limit concentrations (< 5 µM) a few millimeters below the SWI. Fe(II) concentrations did not increase until 20 mm depth suggesting that the presence of O_2 in the sediments prevented the net accumulation of Fe(II) in the porewater. However, it is also at these low levels of O_2 (< 50 µM) where the formation of reactive oxygen species (ROS) such as the hydroxyl radical (OH•) from the reaction with Fe(II) and reduced DOM can occur resulting in the formation of Fe(III)-oxides [62]. Thus, in this 10 mm zone just below the SWI the formation of ROS could play an important role in mediating

the oxidation of Fe(II) diffusing from below. Biological iron oxidation is also commonly prevalent in sediments with low O_2 [90]; and likely competes against abiotic ROS mediated reactions in Toolik sediments. It is likely, however, that both biological and ROS-mediated iron oxidation concurrently occur in these surface sediments, contributing to the large pool of poorly crystalline, microbially reducible Fe(III)-oxides found in the surface sediments (Figure 3.3b). Finally, it is possible that another TEA, such as nitrate, may have inhibited Fe(III)-oxide reduction even though it was not measured for this study. However, given the oligotrophic nature of Toolik Lake, nitrate levels are low and range from ~ 1 µM to < 0.1 µM below the euphotic zone [91]. Thus, below this redox active zone biological-mediated iron reduction presumably occurs and is facilitated primarily by iron-reducing bacteria [13,90] since we observed steadily increasing Fe(II) concentrations, up to 270 µM to 300 µM at 50 mm to 100 mm depth. Fe(III)-organic complexes were not present in any voltammograms of STL15, unlike STL9. As previously mentioned, if the Fe(III)-organic complexes observed in STL9 are of terrestrial organic matter origin, it is possible that organic matter input into deep sediments is much lower or of different quality than near shore environments. Previous reports of organic-rich groundwater and active zones above permafrost discharging into the perimeter areas of Toolik Lake [61,74,75] support this notion and could increase the abundance of ligands that can chelate Fe(III). These subsurface discharges can also be a source for other chemical species (e.g., macro- and micro-nutrients, other dissolved metal species, etc.) that may influence the distribution of redox active species into these shallow sediments. It is also possible that weak Fe(III)-organic complexes in this redox active zone are used as an alternative TEA to Fe(III)-oxides [92,93]. As such, the lack of a Fe(III)-organic

complex signal at STL15 could be due to the reduction of these weaker complexes by iron-reducing bacteria to below our detection limits, whereas at STL9 stronger Fe(III)-organic complexes (log K > 20) are the result of chelation with a different pool of ligands derived from allochthonous sources that cannot be readily used as a TEA by these same organisms [92].

3.3.2 Microbiological analysis in Toolik sediments

The second STL15 core was further analysed to link our biogeochemical data to microbial populations that may participate in the cycling of iron, manganese, and carbon in Toolik Lake sediment. The presence of an orange floc on the upper 2mm of STL15 sediment (Figure A.7) suggests the presence of Fe(III)-oxides and the possible presence of Fe-oxidizing bacteria (FeOB). Indeed, Fe(III)-oxide measurements of solid-phase minerals in STL15 indicated an abundance of highly reactive Fe(III)-oxides near the surface of the sediment (Figure 3B) and putative iron-cycling families of bacteria were relatively abundant (based on relative abundances of taxa that can cycle iron or methane) in the surficial sediment, but decreased with depth (Figure 3A). We found taxa related to known FeOB (*Gallionellaceae*) at a relative abundance of 0.7% at the SWI, which increased slightly to a peak relative abundance of 1% at 0.25 cm (Figure 3A). These FeOB then decreased in abundance with depth to <0.4%, concurrent with a loss of the visible Fe(III)-oxides, and extractable, highly-reactive, solid-phase Fe(III)-oxides concentrations (Figure 3B). The other well-known, freshwater FeOB, *Leptothrix*, was not an abundant member (<0.01%) of the microbial community in the Fe-oxidation region of these sediments. Microbial taxa with relative abundances >1% are generally considered abundant members of the microbial

community, while those with relative abundance <0.01% are generally considered rare [94-96].

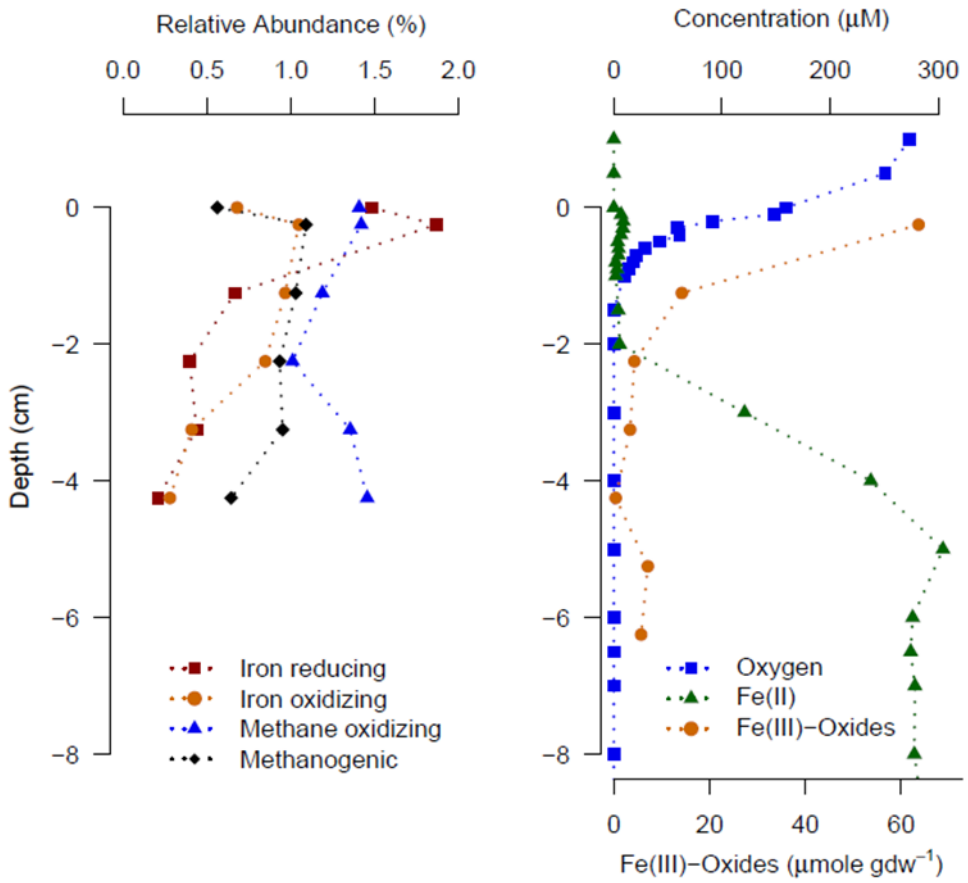

Figure 3.3 Relative abundance profiles of key taxa from STL15 containing known iron and methane cycling microorganisms (left panel) and a zoomed in representation of Fe(II) and O_2 data presented in Figure 2 (STL15), as well as solid phase measurements of Fe(III) (orange circles). The profiles are summed relative abundances of functional groups of organisms including iron reducing taxa (*Geobacteraceae* and *Geothrix*), iron oxidizing (*Gallionellaceae*), methane oxidizing (*Methylomonadaceae*, *Methylococcaceae*), and methanogenic (*Methanoregulaceae*). Fe(II) measurements a the SWI are at the limit of detection (5 µM). Fe(III)-oxides measurements are single measurements.

The Fe-reducing bacteria (FeRB) bacteria (*Geobacter*, *Geothrix*, *Anaeromyxobacter*, *Desulfuromonas*) were more abundant than the Fe-oxidizing

bacteria (*Gallionella, Sideroxydans, Leptothrix*) in the surficial sediment. These profiles of FeRB were driven by the relative abundances of the *Geobacter* genus, which peak (1.1%) at 0.25 cm depth, then decreased quickly donwcore, but maintained a relative abundance >0.05% (Figure 3.3). The genus of the FeRB, *Geothrix*, was also present in greatest relative abundance (0.6%) at 0.25 cm, then decreased downcore. The *Gallionellaceae* family is known to contain microaerophilic FeOB that tightly follows the oxygen-Fe(II) redox interface [13,97]. In order to sustain FeOB activity there must be a source of Fe(II), which appears to be spatially separated from the obvious Fe(II) source at depth (~5 cm). The Fe(III)-oxides decrease with depth, but the lack of Fe(II) increase until 2 cm depth reveals an apparent imbalance. This imbalance may be caused by loss of Fe(II) as a result of fast abiotic and biotic oxidation in the water column as well as Fe(III)-oxides acting as a sink and adsorbing Fe(II) [98]. The low Fe(II) concentrations captured in the upper 2 cm by the high resolution porewater data also imply that there is iron cycling on the surface of the Toolik Lake sediments between biological Fe(III)-oxide reduction that is fueled by coupled biotic and abiotic Fe(II) oxidation. This cycling of iron within biogenic Fe(III)-oxides is known to occur in laboratory experiments which mimic the conditions found in lake sediments [99], as well as in natural iron mats [100]. The low concentration of Fe(II) at our voltammetric detection limit within the orange floc at the sediment surface (Figure 3.2b, 3.3b) and within the pool of highly reactive Fe(III)-oxides suggests this process and is likely due to the relatively abundant population of FeRB present. Members of the *Geobacter* genus are known to be primarily obligate anaerobic organisms, so their abundance in the oxic, surficial 0.5 cm with O_2 concentrations in the range of 40 – 160 µM is noteworthy. There is evidence that

Geobacter sulfurreducens can grow with oxygen as the sole terminal electron acceptor [101], but our sequencing of the V4V5 region of the 16S rDNA gene sequence precluded taxonomic assignments to the species level. Furthermore, the relative abundance of *Geobacter* decreased with depth as the sediment became anoxic and Fe(II) concentrations increased (below 1.5 cm). The presence of *Geobacter* in the oxic, surficial sediment is likely due to the geochemical conditions promoting Fe-reduction such as, fresh, labile organic matter settling to the sediment surface and the presence of a poorly crystalline, energetically favorable Fe(III)-oxide produced by FeOB (Figure 3.3). Given the high quantity of Fe(II) in the porewater of Toolik Lake sediments (Figure 3.2), the habitat for the FeOB-FeRB consortia may be widespread across the Toolik Lake sediment surface. Since these consortia are present in Fe(III)-oxide rich layers, they may play a significant role in organic matter remineralized through Fe(III) reduction instead of its conversion to methane, especially in deep water sites where FeOB produce highly reactive Fe(III)-oxides for FeRB.

A potential for methanogenesis is indicated throughout the sediment core with the identification of putative methanogenic families of archaea (*Methanobacteriales*, *Methanococcales*, *Methanomicrobiales*, *Methanosarcinales*, *Methanopyrales*) [102] in uniform abundance from 0.5 to 1% down the entire core. The depth distribution of methanogenic taxa is primarily driven by the genus *Methanoregula*, which is known to be capable of metabolic activity and methanogenesis in acid conditions [103]. Based on our voltammetric data, this possibly indicates that methanogens near the sediment water interface are able to persist on H_2 and CO_2 generated from organic matter mineralization coupled to Fe(III) reduction (or abiotic reduction of Mn(III,IV)) [104]. Indeed, measured methogenic communities increased in abundance concurrently with

Fe-reducing communities in the upper mms of STL15 sediment (Figure 3a,b). While methane itself was not measured in this study and linked to the methanogenic communities, past research observed increases in dissolved methane concentration with depth and occur in Toolik Lake sediment from other deep water sites that are similar to STL15 [11].

Putative methane oxidizing bacteria are also present within STL15 sediment. The combination of putative methane-oxidizing families (*Methylobacteriaceae, Methylophilaceae, Methylomonadaceae, Methylococcaceae, Methylothermaceae, Methylocystaceae, Beijerinckiaceae, Methylacidophilaceae*) were abundant in the shallow sediment, persisting at >1.0% relative abundance throughout the sediment core and increase slightly with depth (Figure 3a). There is the potential for iron-mediated anaerobic oxidation of methane (AOM) in these sediments given the abundance of Fe(III)-oxides produced at the sediment surface coupled to methane production at depth [102]. We found one OTU (OTU00368) that was classified within the *Methanoperedenaceae* family, which is known to contain a species implicated in anaerobic iron- and manganese-mediated methane oxidation [101,103-106]. OTU00368 peaked in relative abundance (0.1%) at 0 cm depth, then decreased to 0.04% at 0.25 cm, which is within the surficial, flocculant layer of Fe(III)-oxides and corresponds to the layer where highly reactive Fe(III)-oxides were detected. Within the top 0.5 cm, the *Methanoperedenaceae* would get relatively fresh and thermodynamically-favorable Fe(III)-oxides from authigenic production by abundant FeOB and methane diffusing upwards from depth [103]. A mass balance at STL15 further indicates that solid-phase Fe(III) is in excess of porewater Fe(II) by many orders of magnitude, which shows that favorable conditions for iron-reducing bacteria,

as well as methanotrophs using Fe(III), exist (refer to the appendix for a sample calculation). The biogeochemical profiles of non-overlapping Fe(II) and O_2 seen at STL15 in Toolik Lake also occur at shallower depths and are observed at STL9 and other sites in Toolik Lake (Figure A.6). The redox species profiles and 16S rRNA microbial community data corroborates observations made by other investigators in Arctic and sub-Arctic lakes [110-112]. Cumulatively, this implies that iron abundance and cycling coupled with biological methane oxidation, may play a role in regulating the release of methane from the sediments and is occurring over much of the Toolik Lake benthic zone.

3.3.3 Iron cycling in a tundra seep

As a contrast to lake sediment, we investigated an iron-rich, reducing system situated in a pool of water on the banks of the Oksrukuyik Creek (North Slope, Alaska, Figure 3.1c.), which contained a thick (~20-40 cm) biogenic Fe(III)-oxide mat produced by FeOB (Figure A.2, A.3). The *Gallionellaceae* family of FeOB, with a relative abundance 5.1% of the total microbial community in this sample were the dominant group of FeOB in this Fe-oxide mat, similar to the Fe(III)-rich, orange, surficial sediments of Toolik Lake. FeRB from the *Geobacter* and *Geothrix* genera were also present in the Fe-oxide mat at 1.2% relative abundance (Figure 3.4B). The co-occurrence of these two functional groups in a Fe(III)-oxide mat from another aquatic habitat indicates that the consortia of FeOB and FeRB potentially fuel an iron cycle within the Fe(III)-oxide mat. Taxa closely related to methane oxidizing microorganisms were found in the Fe-oxide mat at 1.2% relative abundance (Figure 3.4B). The small gully was in a low lying-area surrounded by organic-rich soils and characterized by thermokarst topography. It receives water from a small wetland

upgradient and discharges downstream into the Oksrukuyik Creek. The gully may also receive groundwater from a large wet sedge meadow located upgradient from the riverbank. These inputs from the surrounding environment likely provide the organic matter needed to fuel Fe reduction. The water within the gully contains dissolved Fe(II) and Fe(III) (the later existing as stable organic complexes per our previous observations). The seep water is also suboxic (O_2 <1 μM) and possessed circumneutral pH (6.8) (Figure 3.4). For these field analyses, we measured O_2 concentrations with a dissolved oxygen potentiometric electrode, as the voltammetric O_2 peak overlaps with a broad Fe(III)-organic complex signal in these samples, making quantification more difficult. Further, like our measurements in STL9, we reported Fe(III) as current response (nA). Despite the overlying water being suboxic, there were few methanogenic taxa (<0.04%) within the biogenic iron mat (Figure 3.4b).

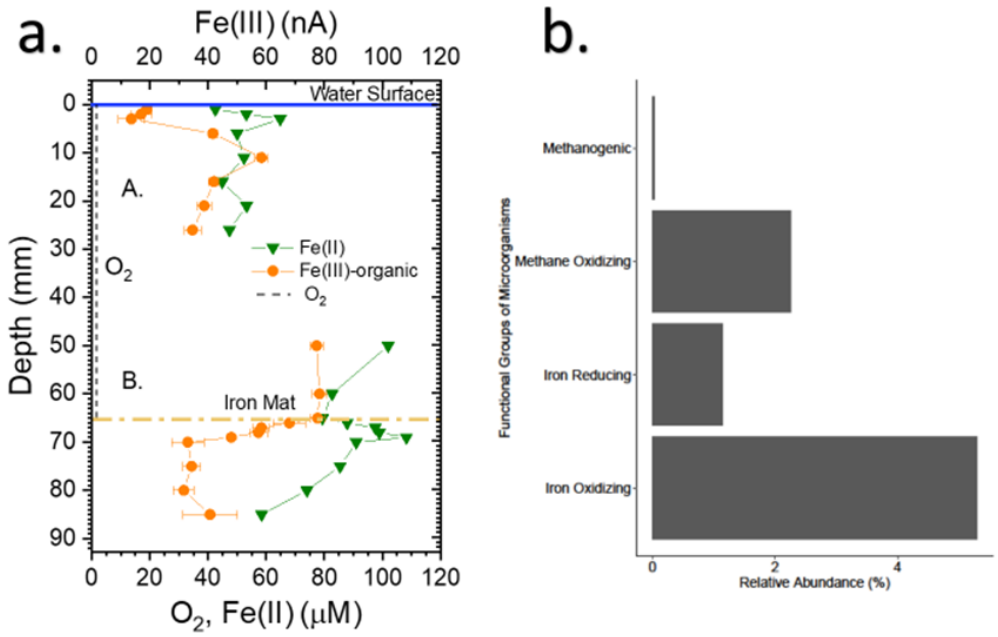

Figure 3.4 a. Fe(II) and Fe(III)-organic complex (Fe(III)-organic) profiles of A) the water column of an iron seep near Oksrukuyik Creek, located directly above a biogenic iron-oxide mat, and B) through the biogenic iron-oxide mat (denoted by the brown horizontal dashed line). Note the O_2 concentration is plotted as a vertical dashed line. Fe(III)-organic complex is plotted as an average of current response (nA). Error bars for Fe(III)-organic complex and Fe(II) indicate one standard deviation from the mean of three or more measurements. . b. Abundances of iron and methane cycling bacteria present in iron mat. Reported measurements are an aggregate of a sample taken within the iron mat (5 cm vertical resolution) in the water column.

Fe(II) concentrations increase from 41 µM at 1 mm of depth to 62 µM at 3 mm below the surface while the Fe(III)-organic complex current response similarly increases and tracks the Fe(II) profile from 19 nA at 1 mm to 47 nA at 6 mm of depth (Figure 4). In contrast, an *inverse* profile trend was observed between Fe(II) and Fe(III)-organic complex *within* the microbial iron mat, which occurs between 65 to 70 mm of depth within the mat (Figure 4). A concomitant increase in the Fe(III)-organic

complex signal (nA) with a decrease in Fe(II) concentration at the top of the iron mat may correspond to FeOB communities (i.e. *Gallionella spp* and *Leptothrix ochracea)* consuming Fe(II) through cellular respiration, coupled to the stabilization of generated Fe(III) by strong ligands (e.g., siderophores or DOM) [86,90,112,113]. Additionally, biological data indicates that methanogen communities in the iron mat were low in abundance, possibly due to unfavorable thermodynamic conditions where Fe(III) reduction is the dominant redox process. Interestingly, the presence of methane-oxidizing communities in the seep shows that there is the *potential* for methanogenesis and methane removal by AOM in a manner similar to observations in Toolik sediments. While details of our findings of methanogenesis and methane oxidizing communities lie beyond the scope of this paper, they clearly highlight the need for future investigations into this process in lotic and lentic Arctic environments [115,116].

3.3.4 Environmental implications

To the best of our knowledge, data reported here are the first high vertical resolution *in situ* measurements of redox active substances in Arctic sediment porewaters captured in their native oxidation states coupled to an assessment of the microbial communities as determined by 16S rRNA. Sediment core data from Toolik Lake and an iron mat seep showed spatial variability in redox species, as the iron seep showed reducing behavior (< 3 µM O_2) with Fe(II) and Fe(III) species, while sediment cores collected from shallow and deep water depths appeared to have variability in redox-active species with depth (Figure 2, A.6, respectively). Microbiological data and solid phase geochemistry in a sediment core at a deep water site illustrate that coupled iron cycling between FeOB and FeRB result in our observed

porewater redox species profile and indicates a different cycling pattern in the iron mat. FeRB, aided by the byproduct of FeOB metabolism, may contribute to organic matter mineralization at deeper lake spots within suboxic sediments and suppress methanogenesis. Conversely, shallower areas near the lake perimeter that exhibit slightly more reducing conditions and may be less inhibitory to methanogenesis due to incomplete organic matter mineralization. Future studies from our group at this field site will corroborate voltammetric measurements with pH and other (e.g., methane, DIC, and DOC if possible) measurements.

Our preliminary data in Arctic lacustrine sediments highlights the redox chemistry that results from the unique environment where they exist. For example, Toolik Lake spends the majority of the year under ice cover, which can promote lower oxygen conditions, and even anoxia, in the water column near the sediment surface, leading to more reducing conditions in the sediment and a potentially higher flux of reduced solutes from sediment [117]. While we are currently unaware of existing Arctic sediment methane measurements under the ice, these reducing conditions could promote methanogenesis [117,118]. Conversely, methanotrophs may persist on alternative electron acceptors (i.e. Fe(III)-oxides) during ice-induced low oxygen periods [118]. Although our measurements captured only the ice-free summer behavior of redox-active solutes, it is highly likely that they are influenced by winter hydrodynamics [117,119]. Future studies will be paramount in linking winter hydrodynamics, mixing, and hydrology to biogeochemical cycling in order to determine the effect of decreasing ice cover on methane production within Arctic lake sediments. Previous studies have linked methane transport from active layers of permafrost thaw and ground water into near shore, shallow areas of Toolik Lake

[74,75].This implies that Toolik Lake, along with other Arctic lakes, could receive higher loadings of methane in the future as permafrost thaw continues.

This study demonstrates the versatility of utilizing voltametric microelectrodes in remote field studies, due to the portability and durability of both the electrodes and controlling potentiostat. Voltammetry is a potentially powerful tool to assess how redox reactions in Arctic lacustrine systems impact greenhouse gas production and elemental cycling in the Arctic, which is highly sensitive to climate change.

Chapter 4

INFLUENCE OF ORGANIC LIGANDS ON THE REDOX PROPERTIES OF FE(II) AS DETERMINED BY MEDIATED ELECTROCHEMICAL OXIDATION

This chapter is a reprinted version of an article that is currently in review at Environmental Science and Technology: "Hudson, J.M., Luther, G.W., Chin, Y.P., Influence of Organic Ligands on the Redox Properties of Fe(II) as Determined by Mediated Electrochemical Oxidation"

4.1 Introduction

Iron is one of the most abundant elements in earth's crust and exists primarily in (+II) and (+III) oxidation states in environmental compartments [120]. Under aerobic conditions, Fe^{III} predominates over Fe^{II} in the form of insoluble iron-oxyhydroxides [21,121], while Fe^{II} predominates in anaerobic or low pH environments [21,90]. Aqueous Fe^{II} has been extensively studied due to its importance as a reductant in biogeochemical cycles and contaminant attenuation [122-124]. Growing attention has been specifically paid to Fe^{II} complexes, as complexation of Fe^{II} by ubiquitous natural organic matter in the environment is prevalent and expected at most redox interfaces including soils, sediment porewaters, and water column redoxclines [76,85,125,126].

Both inorganic and organic ligands have been shown to alter the redox reactivity of Fe^{II} [122,127-129]. Soluble Fe^{II}-organic complexes, such as those present in dissolved organic matter (DOM), can alter the reactivity of Fe^{II} as a reductant

[122,128,130,131]. Organic ligands that preferentially *stabilize* Fe^{III} as opposed to Fe^{II} decrease its standard state electron reduction potential (E_{H}^{0}) and can increase its ability to reduce inorganic and organic contaminants, e.g., chromium [130], nitroaromatics [132,133], and pesticides [129]. The decrease in E_{H}^{0} of the $Fe^{III}L/Fe^{II}L$ redox couple is caused by the larger thermodynamic stability constants for Fe^{III} relative to Fe^{II} (i.e., $\log K_{Fe(III)} > \log K_{Fe(II)}$) (Eq. 1) [132,133].

$$E_{\mathrm{H}}^{0} = 0.77 - 0.059 log(\frac{K_{Fe(III)L}}{K_{Fe(II)L}}) \tag{4.1}$$

Fe^{III}-stabilizing ligands induce a high spin iron electron configuration [134,135] and are typically comprised of low molecular weight acids, which include functional groups rich in oxygen, (carboxylates, catecholates, hydroxymates and phenolates) [132,136-142], sulfur (cysteine, thiol) [133,143-145], and nitrogen (porphyrins) [146]. Some strong ligands, such as nitrilotriacetic acid (NTA) and ethylenediaminetetraacidic acid (EDTA) have both oxygen and nitrogen bonding ligands [134,147,148]. Fe^{II}-stabilizing ligands, such as ferrozine and phenanthroline, are known to be bipyridyl in structure and contain only N ligating atoms and induce low spin iron [134,149,150]. Recent studies have either modeled or experimentally determined that the majority of Fe^{II} complexed to DOM binds to carboxylate and phenolate groups due to their abundance as DOM moieties. Conversely, while sulfur and nitrogen-containing ligands are stronger they are much less abundant in DOM [136,137].

While results from previous studies have shown how organic complexation can alter the reactivity of Fe^{II} [122,128-133,141-413] as a reductant, the effects of complexation on the oxidation of Fe^{II} remain unclear. Most studies employ probe compounds, which link calculated metal-ligand stability (and henceforth, E_H) constants to experimentally-derived, compound specific reduction kinetics to produce linear free-energy relationships [128-130,132,133]. Kinetics indicate reactivity, but often times redox kinetics do not match expected rates calculated from linear free energy relationships due to the nature of the electron transfer (i.e., inner vs. outer sphere) [128,129,141]. Furthermore, probe experiments are limited in their ability to profile Fe^{II} oxidation over a range of oxidizing potentials because these compounds have a single, fixed potential [128-130,133]. Limiting the experimental potential range over which Fe^{II} oxidation can occur constrains our ability to holistically interpret the redox reactivity of Fe^{II} in the environment [90,128,169].

For our study, we applied mediated electrochemical analysis (MEA) to *directly* investigate and compare the effect of model organic ligands on Fe^{II} redox properties. This approach has been previously used to study the reactivity of humic substances and mineral phases [3,4,16,52], and redox reactions can be conducted under highly constrained thermodynamic conditions (i.e., fixed E_H and pH) inside the electrochemical cell [11]. Specifically, we used mediated electrochemical oxidation (MEO) to study Fe^{II} oxidation in the absence and presence of two model organic Fe^{III} stabilizing ligands, citrate and nitrilotriacetic acid (NTA), as well as one model Fe^{II} stabilizing ligand, ferrozine, across a range of E_H and pH. In MEO, a reduced species undergoes oxidation within the cell in the presence of a mediating compound [4] and its ability to donate electrons is quantified by integrating the oxidative current peaks

[4,16]. To the best of our knowledge, this is the first study that provides direct experimental evidence on how organic ligands alter the redox properties of Fe^{II} under different E_H and pH conditions. We believe our work compliments previous Fe^{III} reduction work by Aeppli et al [11] as we complete the investigation of Fe redox transformations across the E_H-pH stability region [11]. Following our profiling work with citrate, NTA, and ferrozine, we used Fe^{III}/Fe^{II} ratios obtained via current peak integration [4,153,154] (i.e., number of electrons transferred from Fe^{II} to Fe^{III}) to determine apparent reduction potentials, E^{Φ}_{H}, [4,153,154] of other model organic iron-ligand complexes in the electrochemical cell. Redox potentials measured via MEO formed a linear relationship when plotted vs. known thermodynamic stability constants and allowed us to estimate unknown iron-DOM stability constants for Suwannee River Natural Organic Matter (SRNOM).

4.2 Materials and Methods

4.2.1 Chemicals

Chemicals used in our experimental work can be found in the supporting information (Appendix A.5).

4.2.2 Solutions

Solutions were prepared from deionized water, and deoxygenated by purging with argon (99.9% purity) on a heat plate at 100°C. All MEO experiments, as well as cyclic voltammetry (CV) experiments, were performed in aqueous solutions containing pH buffers (all 0.01 M; acetic acid for pH 4 and 5; 2-(N-morpholino) ethanesulfonic acid (MES) for pH 6, and 2-[4-(2-hydroxyethyl)piperazin-1-yl]-

ethanesulfonic acid (HEPES) for pH 7 and 8, CHES for pH 9) in a background electrolyte of 0.1 M KCl.

4.2.3 Mediated Electrochemical Oxidation

Mediated electrochemical oxidation (MEO) of Fe^{II} in the presence and absence of organic ligands was performed using well-established chronoamperometric methods [168,170-173]. Electrochemical experiments were performed inside an anaerobic, N_2-atmosphere glovebox (Plas Labs, Lansing, MI) (95% N/5% H). We used electrochemical cells comprised of 40 ml glassy carbon cylinders (GAZ 4, HTW Germany), which served both as the reaction vessel and working electrode (WE). The solution in each WE cylinder was stirred continuously with a Teflon-coated stir bar. Potential (E_H^{MEO}) measurements were against Ag/AgCl reference electrodes (BASi) and are corrected to the standard hydrogen electrode (SHE) and reported as such hereafter. Each cell contained a platinum wire counter electrode (BASi) that was separated from the WE compartment by a porous glass frit (PORE E tubes; ACE glass). The cells were controlled by Blue-Tooth enabled potentiostats (Dropsens, Metrohm). Current data were collected with a 4 s sampling frequency.

The *extent* of Fe^{II} oxidation was profiled (triplicate experiments) in the absence and presence of citrate, NTA, and Ferrozine at fixed E_H^{MEO} and solution pH. We chose these ligands to profile Fe^{II} oxidation, as they can bind Fe^{II} across a wide range of pH values (i.e. they have low pK_a values), contain a different number of ligands that occupy a range of Fe^{II} octahedral coordination positions (2 to 6), have different ligand donor atoms (oxygen and nitrogen donors), and represent both Fe^{III} and Fe^{II} stabilizing complexes (Figure 4.1) [128,130]. In addition to citrate, NTA, and ferrozine, we added oxalate, EDTA, and SRNOM as ligands for the experimental determination of iron-

ligand redox potentials (see below) to complement our profiling work and provide more variation in ligand binding modes. Further, at pH 4 and 5, our acetate buffer also acted as a very weak ligand for Fe^{II}.

After filling the working electrode cylinder and counter electrode compartment with 32ml and 4ml, respectively, of one of the pH buffered solutions, experiments were initiated by applying a constant E_H^{MEO} to the working electrode. After the background current in the cell decreased and stabilized to values close to 0 µA, an electron transfer mediator was spiked into the working electrode cell (Figure 4.1a). We investigated five mediators (Figure A.8) and chose four (2,2'-azinobis(3-ethylbenzthiazoline-6-sulfonic acid) diammonium salt (ABTS), hydroquinone (HQ), 2,6-Dichlorophenol-indophenol (DCPIP), and hexaammineruthenium(II) chloride (Ru)), to cover our range of experimental E_H^{MEO} (+0.3V to +0.77V at pH 4, +0.1V to +0.3V at pH 7; Figure 4.2a.). The choice of mediator reflected both the E_H^{MEO} controlled by the cell and other factors discussed elsewhere (Section A.5 to A.7). Total mediator concentrations within the cell (300 to 450 µM) in all experiments were always in excess of the total Fe^{II} to be added into the cell and were effective at facilitating electron transfer in our experiments (SI Section S2.4). Following addition of the mediators, the target organic ligand was spiked directly into the cell (Figure 4.1a). For profiling work across multiple E_H^{MEO} and pH, the ligand concentration in the cell was selected to be 10 times (~300 µM) in excess of the initial Fe^{II} to be spiked into the cell (~30 µM) in order to ensure complete complexation of Fe^{II}. In other speciation experiments, added ligand concentrations were adjusted to experimentally determine reduction potentials of both mono and bis complexes (A.7, A.8). Apart from SRNOM, all model ligands added to the cell were *not* electroactive, resulting in no

change of current (Figure 4.1a). Fe^{II} was added to the cell in three triplicate spikes following ligand addition to the cell. The reduction of the oxidized mediator by Fe^{II} caused a current response that was a result of the change in the ratio of the oxidized to reduced mediator within the cell. The current response was analyzed for the number of electrons donated by Fe^{II}, $q_{(Fe^{II})}$, and represents the extent of Fe^{II} oxidized at a fixed E_H^{MEO} and pH.

4.2.4 Data analysis

The extent of Fe(II) oxidation, $q_{(Fe^{II})}$ [mol_e-], was quantified as the number of electrons transferred from Fe^{II} as it was oxidized to Fe^{III} (on a per mass basis) and was calculated by integrating the area underneath the current peak and is represented by equation (4.2):

$$q_{(Fe^{II})} = \frac{1}{F}\int_{t_0}^{t_{end}} I(t)dt \tag{4.2}$$

where *I(t)* is the baseline-corrected oxidative current in amperes (A), *F* is the Faraday constant (96,485 J/mol), and t_0 and t_{end} are the initial and final integration boundaries of the individual current peak (in seconds). Integration was performed using the peak analyzer tool in Origin® 2019. Because our $FeCl_2$ stock solution concentrations were approximately 10 mM, injecting 110 µL of $FeCl_2$ into the cell resulted in a total mass and $q_{(Fe^{II}max)}$ that equaled 1.1 µMoles of electrons if every mole of Fe^{II} was oxidized to Fe^{III}. For profiling experiments across multiple E_H^{MEO} and pH, triplicate experiments of Fe^{II} oxidation peaks were all analyzed and averaged for $q_{Fe(II)}$.

4.2.5 Thermodynamic calculations and modeling

Known stability constants from literature were checked using the Visual MINTEQ database under our solution conditions (A.9, A.10, A.11). From these values, redox potentials for Fe-L complexes were calculated using the Nernst equation (A.12). For ferrozine, we measured the redox potential of the Fe(III)L_3 complex using potentiometry as it has never been reported (A.13). This potential was used to calculate the thermodynamic and conditional constant for the Fe(III)L_3 complex as the conditional constant for the Fe(II)L_3 complex is known (A.10, Table A.2, Table A.3) [149]. We determined reduction potentials for Fe^{II}-ligand complexes in our experiments by combining Visual MINTEQ calculations of speciation and stability constants with experimental results from Fe^{II} oxidation peaks. Using MINTEQ calculations, we first chose specific experimental parameters (ligand concentration, pH, E_H^{MEO}) where our targeted Fe^{II}-ligand complex would be both redox-active (i.e. oxidizable) and present as the abundant species (i.e. our stability constants are thermodynamic as opposed to conditional, Section A.8). Following triplicate Fe^{II} additions into the cell, the first Fe^{II} oxidation peak only was analyzed for $q_{(Fe^{II})}$, as any Fe^{III} generated upon oxidation from the first peak alters the reduction potentials inside the cell (A.15) [11]. Reduction potentials for each Fe^{III}-L/Fe^{II}-L complex were obtained from integrating the current response of peaks using Eq 4.2. (A.15). Integration of the peaks yielded $q_{(Fe^{II})}$, provided the ratio of Fe^{III}-L to Fe^{II}-L (%), which was then used in the Nernst equation to calculate E_H^{Φ}:

$$E_H = E_H^{\phi} - \frac{RT}{F} \ln \frac{\{Fe^{II}\}}{\{Fe^{III}\}} \tag{4.3}$$

where (E_H^{Φ}) (volts) is the apparent standard reduction potential of the redox couple under our solution conditions, which includes ligand complexation at a given pH. R [J/(mol K)] is the universal gas constant, T [K] is the absolute temperature, F is the Faraday constant [96485 C/mol], and $\{Fe^{II}\}$ and $\{Fe^{III}\}$ denote activity respectively. We assumed $q_{Fe(II)}$ was equivalent to Fe^{III} generated upon the oxidation of Fe^{II}.

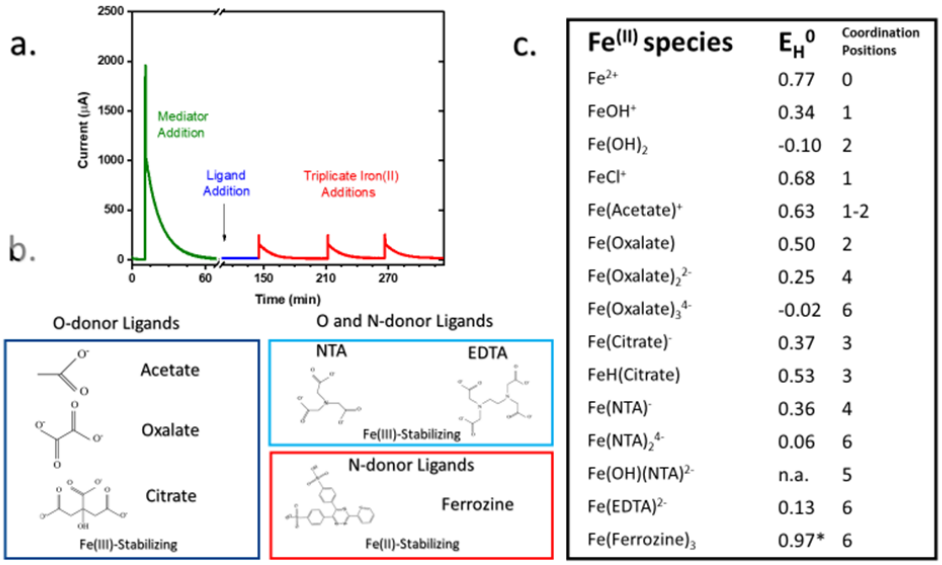

$Fe^{(II)}$ species	E_H^0	Coordination Positions
Fe^{2+}	0.77	0
$FeOH^+$	0.34	1
$Fe(OH)_2$	-0.10	2
$FeCl^+$	0.68	1
$Fe(Acetate)^+$	0.63	1-2
Fe(Oxalate)	0.50	2
$Fe(Oxalate)_2^{2-}$	0.25	4
$Fe(Oxalate)_3^{4-}$	-0.02	6
$Fe(Citrate)^-$	0.37	3
FeH(Citrate)	0.53	3
$Fe(NTA)^-$	0.36	4
$Fe(NTA)_2^{4-}$	0.06	6
$Fe(OH)(NTA)^{2-}$	n.a.	5
$Fe(EDTA)^{2-}$	0.13	6
$Fe(Ferrozine)_3$	0.97*	6

Figure 4.1 Overview of experimental spiking scheme and ligands chosen for Fe(II) oxidation experiments. a. Experimental spiking scheme for MEO experiments. Green represents the addition of a mediator, while blue and red colors represent ligand addition and triplicate iron additions to the cell, respectively. Ligands were not electroactive resulting in a lack of current response upon addition to the cell. b. Structures of organic ligands used in our study, divided by both ligand atom-donor properties, as well as the ligands Fe^{III} or Fe^{II} stabilizing properties. c. Previously reported standard one-electron reduction potentials and coordination positions of some common Fe^{II} complexing ligands that are present in our study. The asterisk by Ferrozine denotes the value we obtained using mediated potentiometry (A.13 and A.14).

4.3 Results and Discussion

4.3.1 Profiling Fe(II) oxidation extent

The extent of Fe^{II} oxidation was measured in the absence and presence of citrate and NTA across multiple E_H^{MEO} and pH, thus manipulating Fe^{II} oxidation over fixed thermodynamic conditions (Figure 4.2a). Figure 2 shows $q_{(Fe^{II})}$ profiled across a range of E_H^{MEO}, +0.3 to +0.77V at pH 4 (Figure 2b), and +0.1 to +0.3V at pH 7 (Figure 4.2d), as well as a range of pH, 4 to 8, at a fixed E_H^{MEO} (+0.3V) (Figure 4.2c). Trends show an increase in $q_{(Fe^{II})}$ occurs when moving from a less-positive to a more-positive oxidizing potential, E_H^{MEO} (i.e. $\Delta G << 0$, Figure 4.2a), regardless of whether or not Fe^{II} existed as a hexa-aquo species ($Fe(H_2O)_6^{2+}$) or was complexed by other ligands (e.g. $Fe(H_2O)_5(OH)^+$, $Fe(H_2O)_5(cit)^-$). This trend exists because oxidation becomes more favorable as E_H^{MEO} increases towards or above the half-potentials of the $Fe^{(III)}/Fe^{(II)}$-L redox couples. The exception to this was experiments with ferrozine (Fz), where $q_{(Fe^{II})}$ remained zero at all conditions tested (Figure 4.2b-d). A lack of $Fe(Fz)_3^{4-}$ oxidation at various E_H^{MEO} was anticipated because nitrogen donor groups on ferrozine and other bipyridyl compounds stabilize Fe^{II} through its low spin electron configuration [32,134,149,150]. The resulting redox potential of the low spin ferrozine complex is much higher than $Fe^{(II)}/Fe^{(III)}$ (E_H = 0.97 V at pH 5, Figure 4.1c), which makes Fe^{II} oxidation thermodynamically unfavorable [32]. Increasing pH also increased $q_{(Fe^{II})}$ (Figure 4.2c), for both $Fe(H_2O)_6^{2+}$ species and complexes with citrate and NTA (e.g. $Fe(H_2O)_5(cit)^-$, $Fe(NTA)_2^{4-}$. At pH 7 under our experimental conditions (total Fe^{II} concentration = 30 µM), $Fe(H_2O)_6^{2+}$ is stable only over a lower E_H range (E_H < +0.3 V) and therefore is readily oxidized in the absence of ligands at applied redox potentials within ± 120 mV of + 0.3V (A.16) [155,156] . Additionally,

hydroxide (mono and di) plays an important role in Fe^{II} oxidation at higher pH [156] as the complexes [$Fe(H_2O)_5(OH)^+$, $Fe(H_2O)_4(OH)_2$] possess redox potentials as low or lower than many organic ligands (e.g. $Fe(H_2O)_4(OH)_2$ = -0.1V) that promote rapid oxidation [133,134,156].

Differences between ligands were apparent, where at pH 4, $q_{(Fe^{II})}$ was larger in NTA experiments than citrate at potentials from +0.3 up to +0.61V (Figure 4.2b). This indicates that $Fe(H_2O)_2(NTA)^-$ was more reactive relative to $Fe(H_2O)_3(cit)^-$ or $Fe(H_2O)_3(Hcit)$ across these E_H^{MEO}, and correlates well to what would be expected from lower redox potentials for Fe^{III}/Fe^{II} ligand complexes with NTA (+0.31V vs. SHE for $Fe(H_2O)_2(NTA)^-$) vs. citrate (+0.33V for $Fe(H_2O)_3(cit)^-$) (A.17) [130,134]. Further, previous literature shows NTA more strongly stabilizes Fe^{III} than Fe^{II} with respect to citrate [130,134,157]. Increasing pH from 4 to 6 opens up available binding spots in both citrate and NTA, assuring more complete oxidation of Fe^{II} species as these ligands become increasingly deprotonated and more able to complex Fe^{II}. This effect is noticeable even at lower E_H^{MEO} (+0.3V), where the higher degree of Fe^{II} binding on citrate and NTA at higher pH leads to larger $q_{(Fe^{II})}$ than $Fe(H_2O)_6^{2+}$ alone (Figure 4.2c).

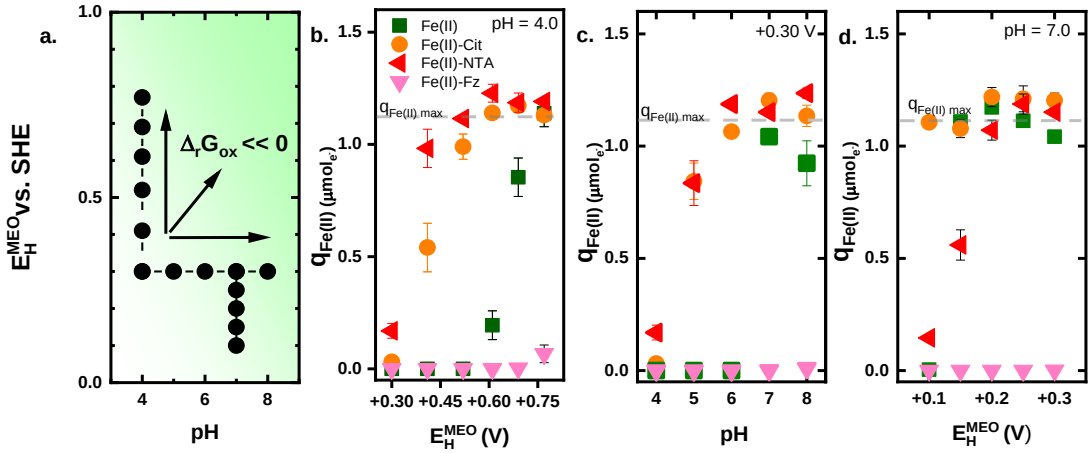

Figure 4.2 a. Overview of experiments. Darker green areas in panel 1 represent experiments where peak response ($q_{Fe(II)}$) was generated. $q_{Fe(II)}$ in Fe(II) - alone, citrate and NTA experiments increased at higher E_H^{MEO} and pH due to a more favorable Gibbs free energy of oxidation ($\Delta_r G_{ox}$, denoted by arrows) that is caused by applying a higher E_H^{MEO} to the electrode or by a decrease in the reduction potential of the iron redox couple and introduction of ligating hydroxide species at higher pH. b. $q_{Fe(II)}$ vs E_H^{MEO} at pH 4. Note that $q_{Fe(II)max}$ (grey dashed line) refers to the maximum number of electrons expected to be donated from the Fe(II) species. (i.e., if every mol of Fe(II) was oxidized to Fe(III)). Fe^{II} (donated by the green symbol) represents scenarios where Fe^{II} is added to the cell in the absence of an organic ligand. c. $q_{Fe(II)}$ vs pH at E_H^{MEO} +0.3V. d. $q_{Fe(II)}$ vs E_H^{MEO} at pH 7. All experiments were performed with a ligand to Fe(II) molar ratio of 10:1.

We decided to further investigate $q_{Fe(II)}$ at lower E_H^{MEO} and pH 7 since many natural waters are close to circumneutral (Figure 2d). Fe^{II} in the absence of organic ligands is readily oxidized at this pH even at potentials as low as +0.15V (Figure 2d). This is not surprising due to the presence of hydroxide complexes (e.g., $Fe(H_2O)_5(OH)^+$ as well as polymeric species), which are strong π donor ligands that enhance Fe^{II} oxidative reactivity (Figure 3c). NTA produced a smaller $q_{(Fe^{II})}$ than

Fe(II) alone when oxidized at +0.15V and +0.2V (Figure 2d). Because carboxyl ligating groups in NTA have smaller π donating effects than hydroxide, the higher (i.e. more positive) redox potentials of Fe^{II} measured in our NTA experiments relative to $[Fe(H_2O)_5(OH)]^+$ at pH 7 indicate that the Fe^{II} speciation in our NTA experiments was $Fe(NTA)_2^{4-}$, as the presence of a hydroxide ligand with NTA would likely enhance reactivity beyond $Fe(H_2O)_5(OH)^+$ alone [134]. 2:1 NTA to Fe complexes would bind Fe^{II} with oxygen atoms in all 6 octahedral positions and prevent binding from strong hydroxide groups that form complexes with low E_H values [130,134,147,148,157]. Finally, citrate enabled $q_{(Fe^{II})}$ across all potentials at pH 7 (Figure 2d). The high reactivity of Fe^{II} is surprising, if one assumes that all Fe^{II} bound to citrate at pH 7 would be in the form of a 1:1 $Fe(H_2O)_3(Cit)^-$ complex ($E_H \approx +0.34V$), but the presence of strong hydroxide ligands at pH 7 and the lability of citrate (i.e. weaker log K compared to NTA) enhances the reactivity of Fe^{II} through π donor effects with OH^- [134]. Several studies of Fe-citrate complexes have either suggested or shown the formation of strong complexes influenced by hydroxide, including ternary bi-nuclear complexes resulting in lower than anticipated E_H values for ($[Fe_2(OH)_2Cit]$) [93,158,159]. Under our experimental conditions, formation of these Fe(III) complexes would be likely upon Fe(II) oxidation given the circumneutral pH and excess ligand added. Additionally, rapid formation of Fe^{III}-hydroxides upon oxidation are possible due to the weaker stability of Fe^{III}-citrate complexes compared to NTA, which could promote heterogenous Fe^{II} oxidation [10,122,155]. While precipitation of Fe^{III} hydroxides is possible, we suspect that this is unlikely due to the time frame of our experiments and the lack of Fe^{III}-hydroxides present in the electrochemical cell at

the onset of the experiment (i.e., Fe^{III}-hydroxides have to be formed first though oxidation of Fe^{II}).

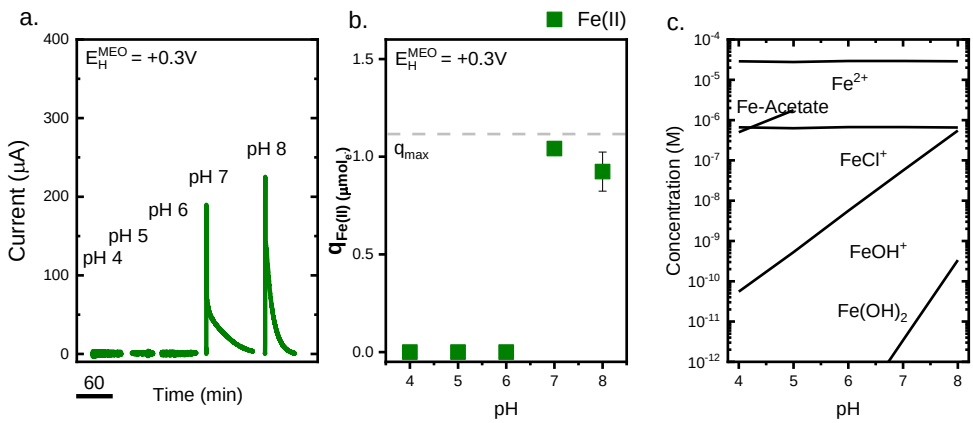

Figure 4.3 Fe^{II} oxidation profiled across pH 4 to 8 at $E_H^{MEO} = +0.30V$. a. Current response for Fe^{II} oxidation from pH 4 to 8 at $E_H^{MEO} = +0.30V$. b. $q_{Fe(II)\ max}$ = the maximum number of electrons of Fe^{II} to be donated if every mole of Fe^{II} in the electrochemical cell (1.1 μmole e-) was oxidized c. Speciation of Fe^{II} species present in the experimental parameters tested from pH 4 to 8 in the absence of other organic ligands (acetate excepted as it was used as a buffer). Note that weak Fe-Acetate complexes were only present in abundance at pH 4 and 5.

4.3.2 Effect of speciation on Fe^{II} oxidation

Variations in $q_{Fe(II)}$ can be explained by examining the effects of citrate and NTA on Fe^{II} speciation. Using Visual Minteq, we predicted Fe^{II} speciation conditions in the absence and presence of different concentrations of citrate and NTA and at different pHs, and then linked these calculations directly to experimental data where we directly manipulated ligand to iron ratios and pH (Figures 4.3 and 4.4).

Oxidation experiments in the absence of any organic ligands were performed from pH 4 to 8 at E_H^{MEO} = +0.3V in order to model the effect of inorganic ligands (i.e., hydroxide species) on Fe^{II} oxidation current response. From pH 4 to 6, no current was

generated at E_H^{MEO} = +0.3V (Figure 4.3a), indicating that the dominant species present was $Fe(H_2O)_6^{2+}$. This matched speciation modeling (Figure 4.3c), which resulted in no electrons being donated (Figure 4.3b). At pH 7, a sharp current response was observed, indicating an increase in Fe^{II} reactivity at E_H^{MEO} = +0.3V (Figure 4.3a) and $q_{(Fe^{II})}$ (Figure 4.3b). Speciation modeling at pH 7 showed nM concentrations of $Fe(H_2O)_5(OH)^+$ (Table A.18) , which would greatly influence Fe^{II} oxidation as stated earlier (A.18). A sharper response was visible at pH 8 (Figure 4.3a), which corresponded to higher concentrations of $Fe(H_2O)_5(OH)^+$ (~550 nM, Table A.18) based on our speciation modeling.

For citrate, $Fe(H_2O)_3(Cit)^-$ and $Fe(H_2O)_3(HCit)$ are the two main complexes expected to be in abundance under varying solution conditions (Figure 4.4i, 4.4j). At pH 5, $Fe(H_2O)_3(Cit)^-$ is important relative to $Fe(H_2O)_6^{2+}$ only at ligand to iron ratios greater than 10:1 (Figure 4.4i.) Across a pH range from 4 to 8, $Fe(H_2O)_3(Cit)^-$ dominates as the main complex at or above pH 5 (Figure 4.4j). Although speciation of $Fe(H_2O)_3(Cit)^-$ and Fe $(H_2O)_3(HCit)$ varies across solution conditions in both cases, a visual comparison of current peaks and experimental data with trends in Fe^{II} speciation suggests a parallel between $q_{Fe(II)}$ and Fe-Cit (Figures 4.4e, 4.4f). This suggests that Fe-Cit is the *main complex* responsible for Fe^{II} reactivity (oxidation) across most experimental parameters, although Fe-HCit may contribute to $q_{Fe(II)}$ at higher ligand to Fe(II) ratios at pH 5 (Figure 4.4e). Increased q values at higher pH in the absence of Fe-HCit correlate with the appearance of OH^- and indicate its influence as a ligand for Fe^{II} (Figures 4.4b, 4.4f, 4.4j) as stated previously [160-162]. This is more likely with citrate than NTA due the liability of citrate only occupying 3 out of 6 octahedral coordination positions of Fe^{II}, as opposed to NTA or NTA_2, which can occupy 4 and 6

[157]. Additionally, qualitative analysis of current generated from Fe^{II} oxidation shows an increase in peak size, corresponding to a reported increase in $q_{Fe(II)}$ (Figures 4.4e, 4.4f) with citrate concentration and pH (Figures 4.3a, 4.3b). While we did not analyze current response in this study for oxidation kinetics, it is interesting to note that peak heights increase along with tailing patterns with increasing ligand concentration, and pH i.e., peaks became sharper with less tailing. This likely indicates changes in Fe^{II} oxidation kinetics that are parallel with these increasing experimental parameters (particularly pH), which would match previous work looking at Fe^{II}-citrate oxidation kinetics [130, 160-162].

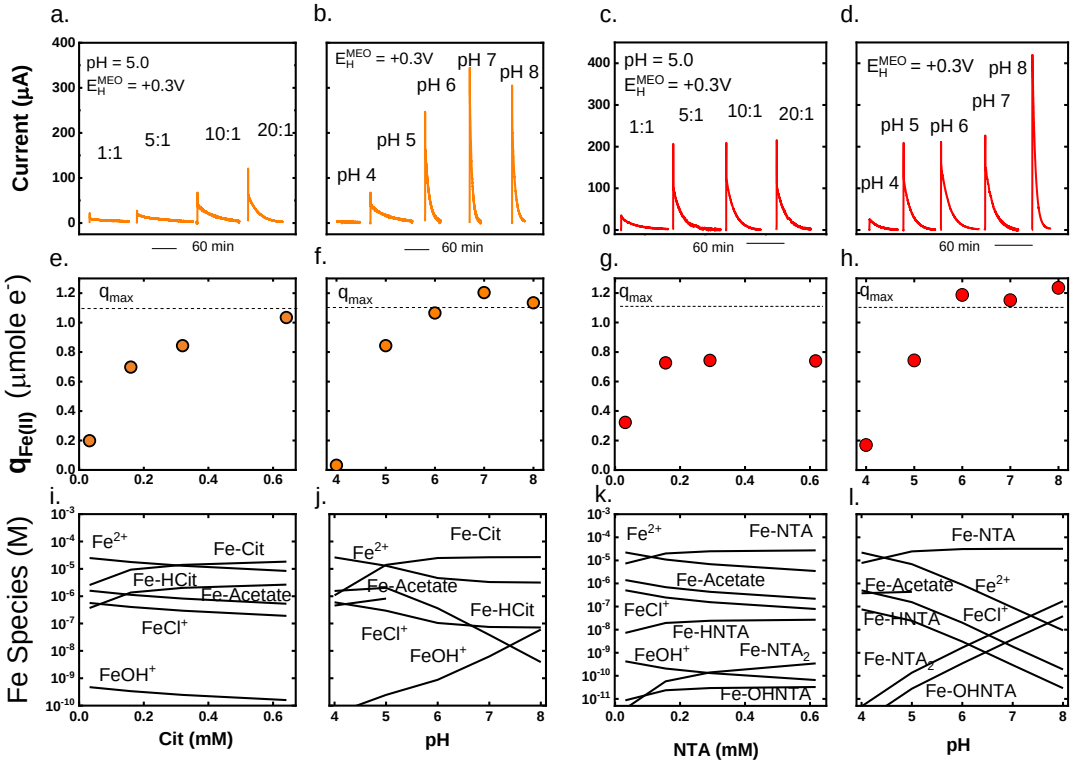

Figure 4.4 Fe^{II} oxidation experiments in the presence of citrate and NTA at various ligand to iron ratios and across different pH's. Experiments using different ligand to iron ratios were performed at pH 5.0 in 10 mM acetate buffer with fixed $FeCl_2$ concentrations of 30 μM with ligand concentrations of approximately 30, 150, 300, and 600 μM (equating to roughly 1:1,5:1, 10:1, and 20:1 ratios). Experiments ranging from pH 4 to 8 were all performed at 10:1 ligand to iron ratios. a-d. Current responses for peaks across all experimental conditions. All experiments were performed at E_H^{MEO} = +0.3V, as this potential was close to reported redox potentials of both Fe-L complexes. e-h. Reported $q_{Fe(II)}$ for MEO experiments across all experimental conditions. The dotted lines correspond to the expected maximum q values assuming complete oxidation of Fe^{II} on a per mole basis. i-l. Speciation modeling of Fe-Citrate and Fe-NTA complexes at pH 5 and across different pH values.

For NTA, our modeling showed that the most predominant complex present across solution conditions was a mono $Fe(H_2O)_2(NTA)^-$ complex, with bis $Fe(NTA)_2^{4-}$ complexes appearing at pH 7 and increasing in abundance at pH 8 (Figures 4.4k, 4.4l). Unlike citrate, the 1 to 1 Fe-NTA complex prevailed over free Fe(II) at lower ligand to iron ratios (Figure 4.4k). While citrate and NTA are both tricarboxylic acids, the nitrogen in NTA increases the ligand stability and allows NTA to occupy 4 coordination positions on Fe(II) in a 1 to 1 Fe-NTA complex as opposed to 3 for citrate [157]. This is reflected in its higher stability constant (log $K_{Fe(II)}$ = 10.18) than citrate (log $K_{Fe(II)}$ = 5.89) (Table A.1). A comparison of experimental data with trends in Fe^{II}-NTA speciation suggests a parallel between $q_{Fe(II)}$ and Fe-NTA (Figures 4.4g, 4.4h). Fe^{II} oxidation extent and current peaks associated with NTA experiments do not increase with increasing NTA concentration (Figure 4.4c, 4.4g), as it does in the case with citrate (Figure 4.4e), which is due to the 1 to 1 Fe-NTA complex being the only abundant complex present in all solution conditions. While increasing pH increased $q_{Fe(II)}$ and oxidation peak sizes in our NTA experiments (Figure 4.4d, 4.4h), our modeling shows that peak size increases are due to the formation of reactive $Fe\text{-}NTA_2$ complexes (log K = 12.62) with increasing pH, which differs from citrate experiments at higher pH, where modeling confirmed an influence from OH^- ligands (Figure 4.4j). 2 to 1 NTA complexes coordinate Fe^{II} in all six positions with oxygen donor atoms thereby prevents interaction with OH^-, which increases Fe^{II} oxidation [137,156].

4.3.3 Relationship between experimentally derived redox-potentials and stability constants

We used our data to develop a correlation between the redox potentials of iron-ligand complexes and the thermodynamic stability constants of the complexes based

upon the Nernst equation. Measurements of $q_{Fe(II)}$ indicate the ratio (%) of Fe^{II} initially added to the cell that was oxidized to Fe^{III}. Quantifying the ratio of Fe^{II} and Fe^{III} in our system enables us to calculate E_H^{ϕ} using equation 3 (A.5). Our measured redox potentials correlated with previously reported redox potentials in the literature (Table A.5) [128,130,134]. Figure 4.5a shows that redox potentials obtained experimentally for multiple complexes were linearly correlated with the ratio between Fe^{III} log K_{Therm} and Fe^{II} log K_{Therm}. This indicates that ligands that are more strongly inclined to complex Fe^{III} with respect to Fe^{II} decrease the E_H of the Fe^{III}/Fe^{II} couple, which matches previous studies that have found the same relationship using probe compound reduction kinetics [130,132,133]. Our correlation shows that the effect of ligands on Fe(II) and Fe(III) potentials is Nernstian with a slope of -0.056 ± 0.002, which is not significantly different from the theoretical slope of -0.059 for a one electron transfer; thus, any kinetic effects are minimal [164]. The y-intercept, +0.76 ± 0.02, also corresponds to the standard one electron reduction potential of the Fe^{III}/Fe^{II} couple (+0.77V). Experimentally determined potentials in our Nernstian relationship were primarily at the lower pH values (5) or at explicitly chosen conditions (i.e., E_h, pH, ligand to iron ratio) to capture thermodynamic stability constants. Further, measured redox potentials of iron complexes with highly labile ligands, such as oxalate and citrate, are easily influenced by side reactions involving hydroxide ligands, which preclude their measurement at high pH [134], while weaker 1:1 complexes tend to have higher potentials, bis-oxalate and bis-NTA were among two of the strongest Fe(II)-ligand organic complexes with lower potentials in our experiments. Stronger bonding from more π donor ligands enhances metal basicity, which forces Fe^{II} to donate its electron thereby stabilizing Fe^{III} [134]. This effect may be analogous to Fe^{II}

complexation in the aquatic environment, where 2 to 1 or 3 to 1 complexes are formed with oxalate or other low molecular weight carboxylic acids when ligands (e.g., DOM) exist in excess of Fe(II) [165,166].

We used our linear relationship to predict the unknown stability constants of iron with an aquatic DOM isolate, Suwanee River Natural Organic Matter at pH 4. We chose pH 4 to capture the binding behavior of carboxylic (Type-A) functionalities based on humic binding models developed by Tipping et al [166]. The experimental E_H^{ϕ} value for the SRNOM- complexed Fe^{III}/Fe^{II} couple was +0.583 ± 0.036V, which correspondingly yielded a $\log(K_{Fe(III)}/K_{Fe(II)})$ value of 3.06 ± 0.60. This value correlates well with other iron-humic or iron-fulvic-acid values in the literature [165,166] and indicates that in the presence of SRNOM at pH 4, Fe^{II} oxidation extent is increased only very modestly. Our observation suggests that Fe^{II}-SRNOM is a weak reductant at this pH [86,167]. We are currently using the generated Nernstian relationship to work with other fulvic and humic acid standards as well as from a variety of surface water DOM collected globally to elucidate their stability constants.

Previous work utilizing MEA to investigate the reducibility of solid-phase Fe^{III}-species were able to link reduction kinetics pseudo-first order rate constants from current response (i.e., k_{obs} (s^{-1})) in addition to the amount of Fe^{III} reduced (q_{Tot}^{Fe3+}, *extent*) obtained by peak integration [171]. While our study did not attempt to fit current kinetics from oxidation peaks in experiments in a similar manner, it is interesting to note that a qualitative relationship between peak height and redox potential was observed at low pH (Figure 5b) and with Fe(II)-ligand species when increasing pH (Figure 4.3a, 4.4b, 4.4d). Good correlations between potentials of iron-ligand redox couples obtained in our experiments vs. calculated potentials and

potentials in the literature (Table A.5) indicates that electron transfer obeys Marcus theory (Eq. 4.4)

$$\alpha = \frac{1}{2} + \frac{F(E-E^{\circ})}{2\lambda} \tag{4.4}$$

where E is the potential (V) of complexes found in our experiment, E° is the potential (V) of complexes reported in the literature, F is the Faraday constant, and λ (J $mole^{-1}$) represents the reorganization energy associated with the electron transfer from the Fe(II)-L complex to the oxidized mediator [1,134]. Due to the good agreement between expected and measured potentials (Table A.5), the maximum value of the transfer coefficient term, α, was estimated to be 0.512 from the t_{2g} to e_g absorption peak (or λ) of $Fe(H_2O)_6^{2+}$ (1000 nm or 119, 640 J mol^{-1}, Appendix A.19) [134], and the maximum ΔE of 0.03V for $Fe(NTA)_2$ from Table A.5. All other Fe^{II} absorption peaks are higher energy indicating that the second term approaches 0 and that α is close to 0.5 (Figure A.17, A.19). An α value of 0.5 is a typical value that indicates the measure of symmetry of the energy barrier at the electrode [1]; in our case, the α value indicates small internal reorganization (λ) of the Fe(II)-complex upon oxidation by the oxidized mediator species, which is suggestive of an outer sphere electron transfer [1,134].

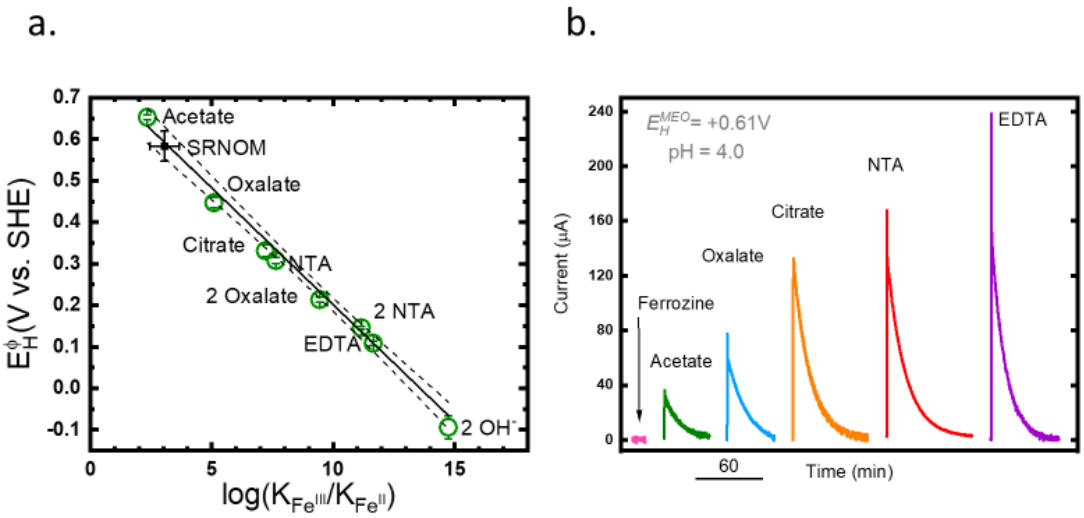

Figure 4.5 Relationships between experimental data obtained and reduction potentials measured for individual ligand complexes. a. Nernstian linear relationship between experimental E_H^{ϕ} and known stability constants of model ligands (green circles). Some error bars are small and hidden within the plotted points. Solid and dotted lines represent the linear regression through the data and the 95% confidence interval, respectively. The fit yielded a slope of -0.056 ± 0.002, a y-intercept of +0.76 ± 0.02, and r^2 = 0.99. Fe-SRNOM log K values at pH 4 were experimentally derived using the slope of the linear relationship and plotted (black square). b. Current response derived from E_H^{MEO} experiments at +0.61V, pH 4 with 6 ligands. Increases in peak response correlate with calculated reduction potentials of Fe-L complexes.

4.3.4 Environmental implications

This work provides the first direct experimental evidence of the effect of organic ligands on the extent of Fe^{II} oxidation under constrained E_H and pH conditions. Previous studies investigating Fe^{II} reactivity utilize probe compounds, which are limited to a single, fixed potential. Our experimental setup allowed us to selectively chose and manipulate multiple oxidizing potentials enabling us to explore the effects of ligands on Fe^{II} oxidation across a range of E_H^{MEO} and pH. Additionally, we were able to *directly* measure E^{Φ}_H of our target complexes. This differs from

previous studies [128-130,132,133,141-143] that *indirectly* link calculated redox potentials of Fe-complexes to the reduction kinetics of probe compounds, which can be influenced by the inner sphere or outer sphere nature of the electron transfer to the probe compound.

Our findings in this study have a few important implications. The first of which, our work highlights the flexible capability of ligands to be able to effect Fe^{II} reactivity across a range of thermodynamic conditions, including those conditions which are known to stabilize Fe(II) against oxidation (i.e., low $E_{H,}$ pH) [122,169,170]. Depending on the E_H of the electron acceptor, certain ligands may promote or enhance electron transfer under unfavorable circumstances. Additionally, we show that some Fe^{III}-stabilizing chelates, such as NTA, may stabilize Fe(II) species against oxidation at pH 7 and higher due to the inhibition of hydroxide ligands from forming complexes with Fe^{II} (Figure 4.2d.) This process, along with reduced moieties in DOM [137], may play an important role in maintaining the persistence of Fe(II) in otherwise (sub)oxic environments at circumneutral pH [171,172].

Finally, because we were able to accurately derive E^{Φ}_{H} of complexes from our experimental data, we successfully built a linear Nernstian relationship that directly correlated E^{Φ}_{H} to stability constants of several model ligands, which closely obeys the Nernst equation. This relationship spans a large range of redox potentials and stability constants, which will allow us to use this scale to estimate stability constants of other unknown ligands, especially those associated with DOM [5]. This work once again highlights the versatility of MEA as an analytical tool and provides a new application of the technology in investigation of redox properties of Fe(II)-ligand complexes. We

anticipate the use of MEA in the future to help us better understand redox processes in the environment.

Chapter 5

ASSESSING IRON COMPLEXATION BY DISSOLVED ORGANIC MATTER USING MEDIATED ELECTROCHEMICAL OXIDATION

5.1 Introduction

Aqueous ferrous iron (Fe^{II}) is an abundant, reduced form of iron that predominates over Fe^{III} in anaerobic and/or low pH environments [21]. Fe^{II} oxidation reactions play an important role in biogeochemical processes that regulate nutrient and metal cycles, carbon cycling, and the degradation of redox-active pollutants [57,122]. Complexation of Fe^{II} by organic ligands that induce a high-spin electron configuration decrease the thermodynamic stability of Fe^{II}, thereby enabling Fe^{II} oxidation in unfavorable conditions (low E_H, pH) and/or increasing the rate (kinetics) of Fe^{II} oxidation [134]. Numerous studies have derived linear relationships between kinetics of probe compound studies and the ratio of Fe^{III}/Fe^{II} stability constants (log K), where model organic ligands with a known log K that preferentially stabilize Fe^{III} over Fe^{II} decrease the redox potential (E_H) of the Fe^{III}/Fe^{II} couple upon complexation [128-134]. In general, many studies show a Marcus relationship where kinetic rates increase with decreasing E_H of the Fe-ligand complex, although certain cases involving inner-sphere electron transfer from the Fe^{II}-ligand complex to the probe compound obstruct this relationship and are a limitation of probe compound studies [128].

Dissolved organic matter (DOM) is ubiquitous in aquatic environments and contains a diverse array of organic functional moieties that can influence Fe^{II}

oxidation, including quinones, carboxylic, and phenolic acids [165,166]. Reduced quinones act as an iron "redox-buffer" by donating electrons to Fe^{III} [137]. Alternatively, carboxylic and phenolic acid moieties in DOM have a strong affinity (log K) for iron, and therefore can act as an iron redox-buffering agent by manipulating the redox reactivity of iron (i.e. enhancing Fe^{II} reactivity or stabilizing Fe^{II} against oxidation) [128,165,166]. While probe compound studies with model ligands have shed some light on the effect of metal complexation on Fe^{II} reactivity as a reductant, the stability constants of ligands in DOM that influence Fe^{II} oxidation are difficult to determine due to the unknown and heterogeneous structure of DOM, as well as the simultaneous presence of multiple different ligands [165,166]. Generally, most metal DOM complexation studies have approximated binding behavior by simplifying DOM into a 2 ligand system (i.e. strong and weak ligand) [165,166] where ligand systems account for the overall stability of multiple ligands with similar behavior. Electrochemical techniques, including competitive ligand equilibration – cathodic stripping voltammetry (CLE-CSV), anodic stripping voltammetry (ASV), and pseudo-voltammetry have been utilized with success in the past to determine unknown conditional or thermodynamic stability constants of metal-ligand (ML) complexes in marine dissolved organic matter and/or siderophores [164,173-175]. While some of these methods have been useful for Fe-ligand (FeL) complexes in marine DOM, stability constants for terrigenous DOM or soil organic matter have yet to be determined in a similar manner. The stability constants of ligands in DOM not only dictate the redox reactivity of Fe^{II}, but also determine the bioavailability of both Fe^{II} and Fe^{III}, reinforcing the importance of knowing the stability constants for Fe-DOM complexes.

In the previous chapter, mediated electrochemical oxidation (MEO) was used to measure the apparent reduction potentials (E_H^{ϕ}) of iron-model ligand complexes. A Nernstian relationship was developed between E_H^{ϕ} and the ratio of Fe^{III}/Fe^{II} complexes ($\log K_{Fe(III)}/\log K_{Fe(II)}$). Because we directly measured E_H^{ϕ}, we were able to overcome previous limitations of probe compound studies that try to match probe compound kinetics to inferred E_H values [128]. Subsequently, the purpose of this study is apply measured E_H^{ϕ} of $Fe^{III/}Fe^{II}$ redox couples in the presence of three DOM isolates and apply this value to our Nernstian linear relationship to estimate the ratio of Fe^{III} to Fe^{II} stability constants. Preliminary results show that our Nernstian relationship is capable of predicting stability constant ratios of strong and weak binding sites in DOM and measured redox potentials of Fe-DOM complexes are similar to previously reported values [173-175]. Additionally, a weaker correlation between Fe^{III} log K values of model ligands and measured potentials suggest that we may be able to determine the thermodynamic log K values of Fe^{III}-DOM complexes, and our values match well with previously reported values in the literature.

5.2 Materials and Methods

5.2.1 Chemicals and solutions

A list of all chemicals used are provided in the appendix (A.5). Solutions were prepared from deionized water, and deoxygenated by purging with argon (99.9% purity) on a heat plate at 100°C. All MEO experiments, as well as cyclic voltammetry (CV) experiments, were performed in aqueous solutions containing pH buffers (all 0.01 M; acetic acid for pH 4 and 2-[4-(2-hydroxyethyl)piperazin-1-yl]-ethanesulfonic

acid (HEPES) for pH 7 and 8, CHES for pH 9) in a background electrolyte of 0.1 M KCl.

5.2.2 Mediated Electrochemical Oxidation

Mediated electrochemical oxidation (MEO) of Fe^{II} in the presence and absence of three IHSS isolates (i.e. acting as organic ligands) was performed using well-established chronoamperometric methods [3]. Electrochemical experiments were performed inside an anaerobic, N_2-atmosphere glovebox (Plas Labs, Lansing, MI) (95% N/5% H). We used electrochemical cells comprised of 40 ml glassy carbon cylinders (GAZ 4, HTW Germany), which served both as the reaction vessel and working electrode (WE). The solution in each WE cylinder was stirred continuously with a Teflon-coated stir bar. Potential (E_H^{MEO}) measurements were against Ag/AgCl reference electrodes (BASi) and are corrected to the standard hydrogen electrode (SHE) and reported as such hereafter. Each cell contained a platinum wire counter electrode (BASi) that was separated from the WE compartment by a porous glass frit (PORE E tubes; ACE glass). The cells were controlled by Blue-Tooth enabled potentiostats (Dropsens, Metrohm). Current data were collected with a 5 s sampling frequency.

As with previous experiments, Fe^{II} oxidation *extent* was profiled in the absence and presence of ligands at fixed E_H^{MEO} and solution pH conditions. Instead of model ligands, we opted to use DOM in the form of three International Humic Substance Society (IHSS) reference standards; Suwannee River Fulvic Acid (SRFA), Suwannee River Humic Acid (SRHA), and Suwannee River Natural Organic Matter (SRNOM) (Table 5.1). We chose these DOM isolates to examine Fe^{II} oxidation as all isolates are well defined, allowing for easy comparison between experiments [176,177].

Additionally, the isolates differ slightly in composition and contain a different number or distribution of ligands (carboxylates, phenolic acids) that act as favorable binding spots for octahedral Fe^{II} (Table 5.1) [174,176,177]. We chose to run experiments in two specific thermodynamic conditions in order to capture DOM binding behavior across reported pKa distributions; at pH 4 and E_H^{MEO} = +0.61V to capture behavior of weak carboxylate binding spots, and pH 8 and E_H^{MEO} = +0.00V to capture the effect of Fe binding to stronger phenolic acids on Fe^{II} oxidation.

Experiments were initiated by applying a constant E_H^{MEO} (+0.61V or 0.0V) to the working electrode after filling the working cell and counter electrode compartment with one of our pH buffered (4 or 8) solutions. After the background current in the cell decreased and stabilized to values close to 0 µA, an electron transfer mediator, 2,2'-azinobis(3-ethylbenzthiazoline-6-sulfonic acid) diammonium salt (ABTS) for pH 4 experiments, or hexaamminerutheniumm(II) chloride (Ru) for pH 8 experiments, was spiked into the working electrode cell. Total mediator concentrations within the cell (600 µM) in all experiments were always in excess of the total Fe^{II} (30 µM). Following addition of the mediators, one of the three DOM isolates was spiked directly into the cell. For speciation work at pH 4, the DOM concentration in the cell (mg C/L) was modulated from 0 to approximately 50 mg C/L. These various conditions represented differed C to Fe molar ratios, as well as different reported carboxyl to Fe molar ratios (Table 5.1). For determination of DOM stability constants, DOM concentrations in all experiments at pH 4 and 8 were equal to approximately 25 mg C/L, which represents roughly a carboxyl to Fe molar ratio of 10 to 1 (Table 5.1). In contrast from previous experiments with model ligands, all DOM isolates in our experiments were electroactive, resulting in current responses upon addition into our

electrochemical cells. This is due to the significant electron donating capacity of various DOM samples [178]. While this electron donating capacity can re-reduce Fe^{III} in other Fe^{II} oxidation experiments, this was not an issue in our electrochemical setup because all reversible reduced DOM moieties (i.e. quinones) were presumably permanently oxidized upon addition of Fe^{II}. Fe^{II} was added to the cell in single spike increments following re-attainment of the DOM current to the baseline. The reduction of the oxidized mediator by Fe^{II} caused a current response that was a result of the change in the ratio of the oxidized to reduced mediator within the cell. The current response was analyzed for the number of electrons donated by Fe^{II}, $q_{(Fe^{II})}$, and represents the extent of Fe^{II} oxidized at a fixed E_H^{MEO} and pH. All experiments were carried out in triplicate (i.e. three separate experiments each of one Fe^{II} addition).

5.2.3 Data analysis and speciation modeling

Integration of Fe^{II} oxidation peaks allowed us to calculate q, which is equivalent to the moles of Fe^{II} oxidized (Equation 5.1):

$$q_{(Fe^{II})} = \frac{1}{F}\int_{t_0}^{t_{end}} I(t)dt \tag{5.1}$$

where *I(t)* is the baseline-corrected oxidative current in amperes (A), *F* is the Faraday constant (96,485 J/mol), and t_0 and t_{end} are the initial and final integration boundaries of the individual current peak (in seconds). Integration was performed using the peak analyzer tool in Origin® 2019. Reduction potentials for each Fe^{III}-DOM/Fe^{II}-DOM complex were obtained from integrating the current response of peaks using Eq. 5.2. Integration of the peaks yielded $q_{(Fe^{II})}$, provided the ratio of Fe^{III}-L to Fe^{II}-L (%), which was then used in the Nernst equation to calculate E_H^{Φ}:

$$E_H = E_H^{\phi} - \frac{RT}{F} \ln \frac{\{Fe^{II}\}}{\{Fe^{III}\}} \quad (5.2)$$

where (E_H^{Φ}) (volts) is the apparent standard reduction potential of the redox couple under our solution conditions, which includes ligand complexation at a given pH. R [J/(mol K)] is the universal gas constant, T [K] is the absolute temperature, F is the Faraday constant [96485 C/mol], and $\{Fe^{II}\}$ and $\{Fe^{III}\}$ denote activity respectively. We assumed $q_{Fe(II)}$ was equivalent to Fe^{III} generated upon the oxidation of Fe^{II}.

Fe^{II} binding to fulvic and humic acids were modeled using a general NICA-Donnan model in Visual Minteq. Measured reduction potentials of our Fe-DOM complexes were plotted using our previous Nernstian relationship to obtain ratios of Fe^{III}/Fe^{II} stability constants. We assume that the stability constants of Fe-DOM complexes generated in our experiments are thermodynamic since the Nernstian relationship used to determine the stability constants is built with thermodynamic stability constants of model ligands.

Table 5.1 Overview of IHSS standards and concentrations used in our experiments. Molar carbon to iron and carboxyl to iron ratios are based on Fe concentrations of 30 µM.

SRNOM (SR2R101N) [mg/L]	**[mg C/L]**	**Molar ratio [µM C/µM Fe]**	**carboxyl: iron molar ratio**
47	24	68	10
SRFA (2S101F) [mg/L]	**SRFA [mg C/L]**	**Molar ratio [µM C/µM Fe]**	**carboxyl: iron molar ratio**
0	0	0	0.0
7	4	10	1.3
23	12	34	4.5
47	24	68	9.0
92	48	134	17.9
SRHA (3S101H) [mg/L]	**SRHA [g C/L]**	**Molar ratio [µM C/µM Fe]**	**carboxyl: iron molar ratio**
0	0	0	0.0
7	4	10	1.1
23	12	35	3.7
46	25	69	7.3
92	50	139	14.7

5.3 Results and Discussion

5.3.1 Effect of DOM concentration on MEO current response

Electrochemical Fe^{II} oxidation experiments in the presence of DOM were initially performed to qualitatively assess the influence of DOM and increasing dissolved organic carbon (DOC) concentrations on MEO current response. Fe^{II} oxidation peaks at E_H^{MEO} = +0.61V in the presence of SRFA are shown Figure 5.1a. In the absence of SRFA, current reaches a peak of approximately 50 µA, corresponding to oxidation of roughly 16% of the original Fe^{II} added to the cell and indicating minimal oxidation at pH 4. Indeed, our previous work shows that weak complexation by our acetate buffer at pH 4 allows for some oxidation of Fe^{II}, and it is relatively

limited at pH 4. Interestingly, lower concentrations of SRFA decreased current response, possibly indicating the presence of exceedingly weak carboxylate ligands (e.g., COO^- groups) that stabilize Fe^{II} against oxidation at pH 4 compared to acetate. Previous studies have shown that DOM can accelerate, retard, or have no effect of Fe^{II} oxidation kinetics [179,180]. The contradictory nature of these results demonstrates the amorphous nature of DOM, which includes ligands that accelerate Fe^{II} oxidation while others can stabilize Fe^{II} from oxidation [176-180]. Our experimental system avoids this later effect, as our electrochemical cells and redox mediator (ABTS at pH 4) are poised at a fixed potential that oxidizes any previously reduced moieties from in DOM before we add Fe^{II} into the cell. At higher SRFA concentrations, peaks grow larger, indicating that SRFA is enhancing the extent of Fe^{II} oxidation compared to Fe^{II} in the absence of SRFA (Figure 5.1a). This effect is not surprising and due to the DOM binding Fe^{III} more favorably from its higher charge than Fe^{II}. an increased availability of Fe^{III} stabilizing binding sites at higher DOM concentrations that can outcompete Fe^{II} stabilizing sites. Favorable Fe^{III} binding sites are most likely deprotonated carboxylic acid functional groups, due to their high reported abundance in SRFA [176-177].

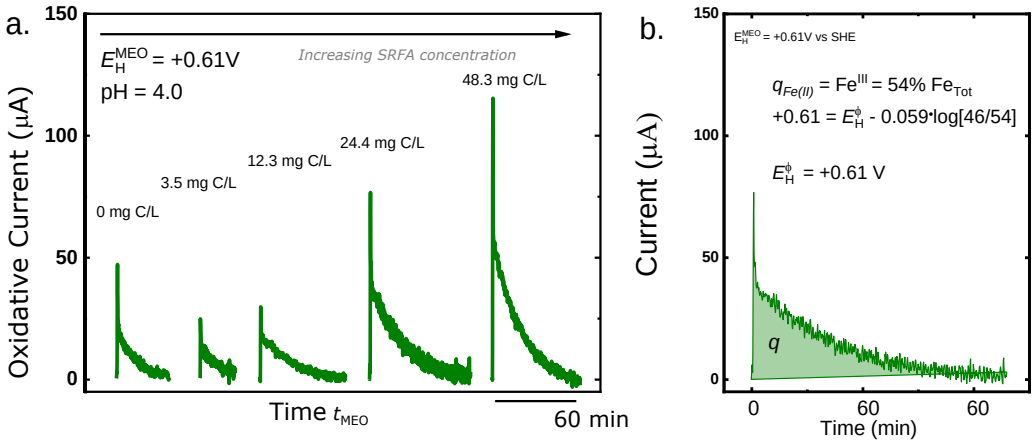

Figure 5.1a.Current response for Fe^{II} oxidation at an applied potential of +0.61V and pH 4. Concentrations of SRFA used in experiments are located above their corresponding current responses for Fe^{II} oxidation. Each oxidation peak corresponds to a single spike of Fe^{II} that equates to a concentration of 30 µM Fe^{II}. b. Example of a current response and integration producing q following Fe^{II} oxidation. A calculation of apparent reduction potential (E_H^{ϕ}) based on the current response is included

In order to further explore the effect of DOM speciation on Fe^{II} oxidation, peaks were integrated to quantify the extent of oxidation and paired with speciation calculations in Visual Minteq using a generic NICA-Donnan model to estimate the distribution of Fe^{II} bound to DOM. In addition to SRFA, SRHA was used as an alternative DOM to profile Fe^{II} oxidation extent. Figure 5.1b. shows an example integration of peak current that results from Fe^{II} oxidation in the presence of SRFA. Integration of peaks yields electrons transferred ($q_{Fe(II)}$), which is directly equal to Fe^{III} formed upon oxidation of Fe^{II} and therefore related to iron ratios that can be used to calculate reduction potentials using the Nersnt equation (Eq 5.1, Figure 5.1b.). Figures

5.2a and 5.2b show the fraction of Fe^{II} oxidized from initial Fe^{II} added to the cell in the presence of various concentrations of SRFA and SRHA. In both cases, small concentrations of DOM *decrease* oxidation extent, corroborating qualitative results observed from our peaks. As with SRFA, SRHA likely contains weak carboxylate ligands that inhibit Fe^{II} oxidation at low DOM concentrations with respect to acetate [176,177]. In both cases, increasing concentrations of DOM lead to an increase in $q_{Fe(II)}$, as evidenced by an increase in peak response (Figure 5.1a). Interestingly, comparable additions of SRHA with respect to SRFA increased $q_{Fe(II)}$, indicating that stronger Fe^{III} stabilizing ligands exist in SRHA than SRFA at pH 4 that contribute to an increase in Fe^{II} oxidation extent as concentrations of DOM increased.

When paired with a NICA-Donnan speciation modeling (Figure 5.2c, d), increased reactivity of Fe^{II} becomes more evident because less Fe^{II} is bound per mg C/L to SRHA than SRFA. Indeed, SRFA is known to contain a higher percentage and distribution of carboxylic acids compared to SRHA (Table 5.1), while SRHA contains a higher percentage of phenolic acids that are stronger Fe^{III}-stabilizing ligands than carboxylic acids and henceforth increase the redox- reactivity of Fe^{II}. Although measurements are performed pH 4, which doesn't allow for the deprotonation of phenolic acids, this difference in Fe^{II} oxidation extent between the two humic substances is still significant, particularly at higher concentrations of DOM (Figure 5.2d). Modeling in Figures 5.2c and 5.2d only show total DOM binding spots for Fe^{II}, which account for both strong and weak complexation to the DOM. However, closer inspection of speciation modeling (Table A.8) show that a small percentage (0.2 %) of Fe^{II} bound to SRHA at pH 4 is bound to strong sites (HA2-Fe(II)) that confirm our

results of increased reactivity in comparison to SRFA, which primarily has only one type (FA1-Fe(II)) of binding site available at pH 4.

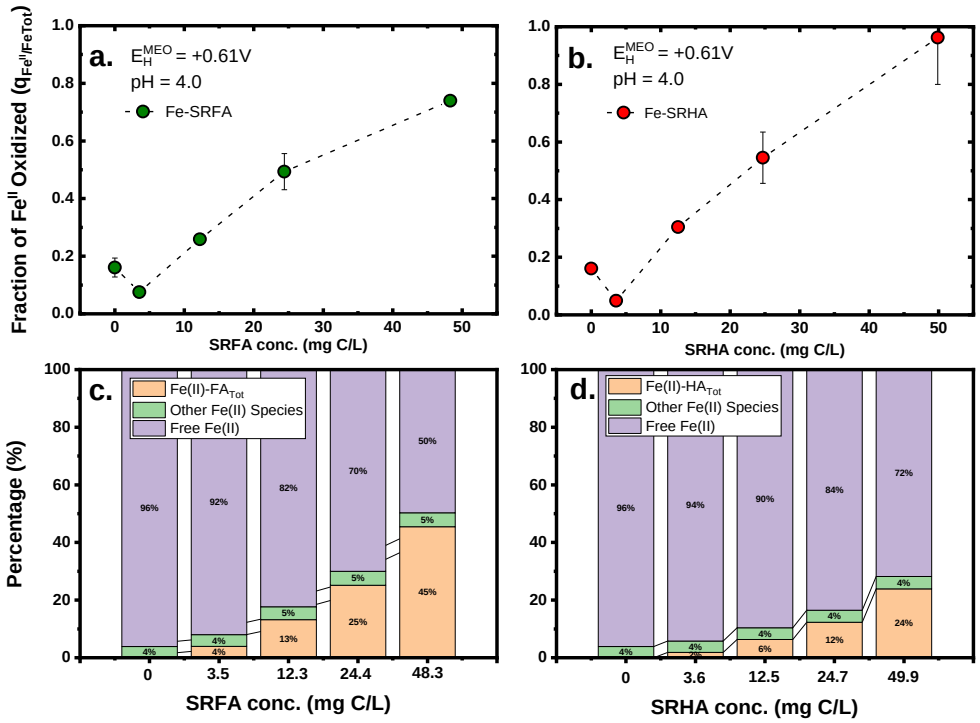

Figure 5.2 a. Fraction of q_{FeII} oxidized from initial Fe^{II} added in experiments in the presence of increasing concentrations of SRFA at an applied potential of +0.61V and pH 4. b. Fraction of q_{FeII} oxidized from initial Fe^{II} added in experiments in the presence of increasing concentrations of SRHA at an applied potential of +0.61V and pH 4 c. Modeling of Fe^{II}-SRFA that exists in our experimental conditions. Fe(II)-FA_{Tot} accounts for binding to FA1-Fe(II), while other Fe(II) species include $FeCl^+$, FeAcetate, and Fe^{II} that is weakly electrostatically bound to DOM (Fe^{2+}D (aq)). d. Modeling of Fe^{II}-SRHA that exists under our experimental conditions. Fe(II)-HA_{Tot} accounts for HA1-Fe(II) and HA2-Fe(II), which are weak and strong binding spots on this humic acid.

5.3.2 Determination of Fe^{III}/Fe^{II} stability constant ratios using the Nernstian relationship

Fe^{II} oxidation extent ($q_{Fe(II)}$) in the presence of 3 IHSS standards were measured at pH 4 and pH 8 in order to capture different binding strengths within my target DOM. For all DOM samples in these experiments, we chose a concentration of approximately 25 mg C/L, to maintain consistent C to Fe molar ratios across all experimental conditions. Although DOM samples vary in carboxyl content, the 3 DOM samples chosen possess similar carboxyl to Fe molar ratios (~10:1), which ensures that all the Fe^{II} is complexed during experiments.

Experimental reduction potentials of Fe-DOM complexes (E_H^{ϕ}) were measured at pH 4 and pH 8 (Table 5.2). Reduction potentials at pH 4 of SRFA, SRHA, and SRNOM cluster around +0.60 V, which indicates that these DOM standards form weak complexes with Fe^{II} under acidic conditions and support previously reported literature values [151]. When Fe-DOM E_H^{ϕ} values are plotted on the linear relationship previously derived (Chapter 4) with model ligand compounds, DOM standards plot between acetate and oxalate, two weaker Fe^{III}-stabilizing ligands, and appear to be more similar in character to acetate, the weakest ligand on the Nernstian relationship (Figure 5.3). This possibly implies that the majority of ligands available to bind Fe^{II} at pH 4 are simple, monodentate carboxylic acids (COO^-) that preferentially stabilize Fe^{III} over Fe^{II}. Although these ligands are weak, they still enhance Fe^{II} oxidation extent relative to Fe^{II} in the presence of acetate. Using our obtained E_H^{ϕ} and the linear relationship, the determined ratio ($\log K_{FeIII}/\log K_{FeII}$) of stability constants for our 3 DOM isolates at pH 4 are roughly 2.5 to 3 (Table 5.2, Figure 5.3), indicating that these DOM isolates are more likely to bind Fe^{III} than Fe^{II} by roughly two to three orders of magnitude.

Reduction potentials of SRFA, SRHA, and SRNOM at pH 8 all lie between +0.0 and +0.1V on our Nernstian linear relationship (Figure 5.3). This result indicates that at higher pH, our DOM isolates are highly effective at Fe^{II} complexation and significantly reduce the redox potential of the Fe^{III}/Fe^{II} couple. When plotted on our Nernstian slope, results show that log K ratios of Fe^{III} to Fe^{II} range from 12 to 13, indicating that iron-DOM chelates at higher pH are very strongly Fe^{III} binding and inclined to enhance Fe^{II} oxidation (Figure 5.3, Table 5.2). In contrast to conditions present at pH 4, other binding sites are likely to be more available at pH 8, due to complete deprotonation of strong (i.e. weaker iron-binding) poly-carboxylic acids (e.g. CDTA), as well as partial deprotonation of some phenolic acids (e.g. catechols) that have a strong affinity for iron [165,166,176,177].

Table 5.2 Measured redox potentials of model ligand complexes and Fe-DOM complexes along with the reported ratios of their thermodynamic stability constants.

Complex	Measured E_H^{Φ}	log K (Fe^{III}/Fe^{II})
Model Ligands		
1. Acetate	0.653 ± 0.007	2.35
2. Oxalate	0.447 ± 0.013	5.09
3. Citrate	0.331 ± 0.015	7.21
4. NTA	0.308 ± 0.007	7.64
5. $Oxalate_2$	0.214 ± 0.006	9.45
6. NTA_2	0.146 ± 0.003	11.16
7. EDTA	0.109 ± 0.006	11.65
8. OH_2	–0.094 ± 0.028	14.74
DOM pH 4		
9.SRNOM	0.589 ± 0.034	2.96 ± 0.55
10. SRFA	0.611 ± 0.006	2.67 ± 0.12
11. SRHA	0.605 ± 0.009	2.76 ± 0.17
DOM pH 8		
12. SRNOM	0.043 ± 0.011	12.81 ± 0.20
13. SRFA	0.043 ± 0.007	12.80 ± 0.13
14. SRHA	0.071 ± 0.028	12.31 ± 0.50

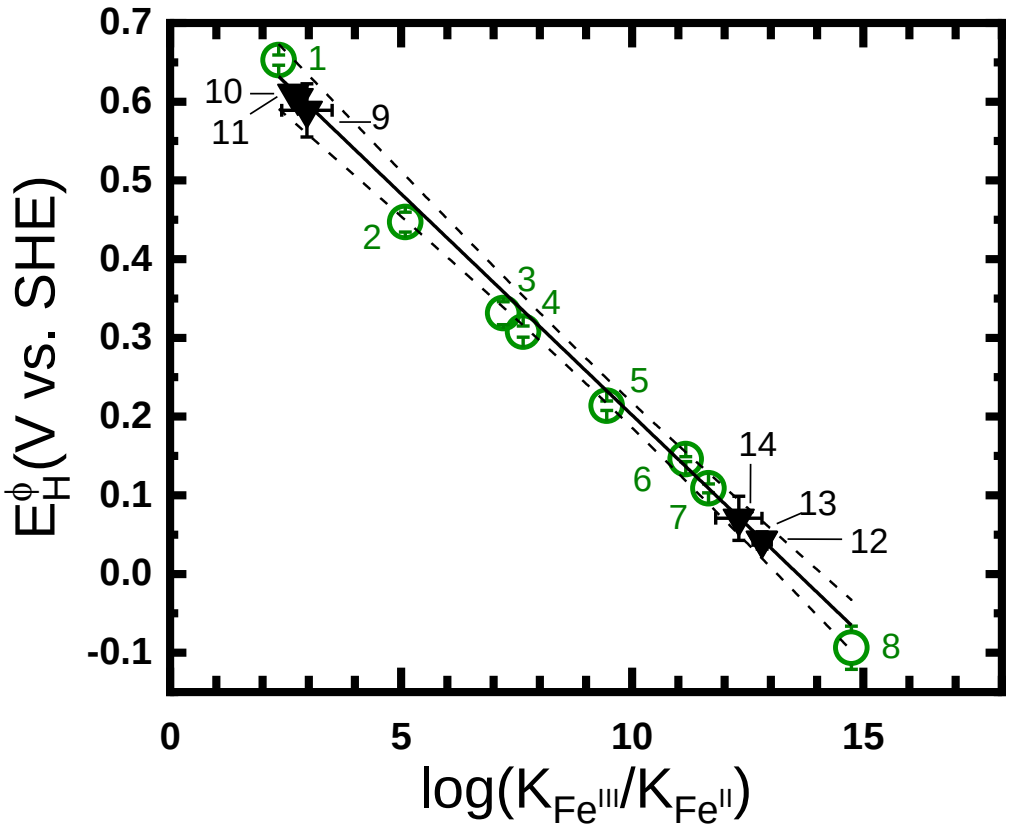

Figure 5.3 Nernstian relationship previously generated with model iron-binding ligands (green open circles) that relates measured reduction potentials to the ratio of their known thermodynamic stability constants. Measured reduction potentials of three IHSS isolates (black filled-in triangles) at pH 4 and 8 are plotted on the relationship to determine the ratio of iron stability constants. The solid black line represents the linear regression of the model ligands, while the dotted line represent the 95% confidence interval. Numbers by data points correspond to ligands listed in Table 5.2.

5.3.3 Determining individual stability constants for Fe^{II} and Fe^{III} from our original Nernstian relationship.

Using our Nernstian linear regression allows us to precisely predict the *ratio* of stability constants of unknown iron-ligand complexes, given that the slope and

intercept (-0.56x, +0.76 respectively) follow Nernstian behavior for one electron transfer processes (Figure 5.3) [1]. While the ratio of stability constants gained from our relationship are useful for predicting abiotic redox-reactivity of Fe^{II}, it precludes the ability to directly estimate individual the individual log K values for Fe^{II} or Fe^{III} stability constants. To estimate individual log K values for Fe^{II} or Fe^{III} complexes, measured E_H^{ϕ} of model ligands can be plotted versus their known individual thermodynamic stability constants (Table 5.3). This practice has been applied in previous electrochemical studies using polarography and pseudovoltammetry for metal complexation, with marine DOM, proteins, and siderophores [164,173-175]. Figure 5.4 shows individual relationships obtained by plotting measured E_H^{ϕ} of model ligand complexes vs known stability constants for Fe^{II} and Fe^{III}. Slopes obtained for Fe^{III} differ from Fe^{II}, as do the coefficients of determination. In contrast to our original relationship that combines the ratio of log K values, both slopes exhibited non-Nernstian behavior. Interestingly, our correlation between measured E_H^{ϕ} and model ligand Fe^{III} log K values is markedly better (R^2= 0.89) than the poor correlation for Fe^{II} complexes (R^2 = 0.77). This is due to the lability of Fe^{II}-DOM complexes, which have been reported to experience slower formation (k_f) and more rapid dissociation kinetics (k_d) from ligands in comparison to Fe^{III} complexes [164]. Additionally, it is possible that in the presence of a redox mediator these disequilibrium effects may be magnified, leading to a poorer R^2, although our measured E_H^{ϕ} values correlated well with reported values in the literature [134].

Because our Fe^{III} data has a tighter correlation, we decided to rely only on this relationship as the basis for developing an Fe^{III} linear scale to estimate stability constants for Fe^{III} DOM complexes (Figure 5.5). We opted to improve the Fe^{III}

regression by removing the $Fe(Oxalate)_2^-$ complex, as this point lies outside our 95% confidence interval in the original Fe^{III} slope (Figure 5.4). $Fe(Oxalate)_2^-$ and other carboxylic ligands likely lie outside our linear regression due to their unstable nature and lability [164]. When $Fe(Oxalate)_2^-$ was removed, our regression became much improved (Figure 5.5, $R^2 = 0.98$). Table 5.3 shows the values of the estimated Fe^{III} stability constants for iron DOM complexes at pH 4 and 8. Our log K values for Fe^{III} are significantly lower at pH 4 (log K ranging from 4.8 to 6.0), indicating relatively weak complexation, although these DOM Fe^{III} log K values are greater than our acetate buffer (4.24). At pH 8, our Fe^{III} log K values are significantly larger for all 3 IHSS standards (Table 5.3). As discussed with our original Nernstian relationship, it is probable that iron binding in our experiments captured at pH 8 are strong ligand sites (analogous to L1 ligands commonly reported in the literature) [173-175]. From the estimated log K values obtained via our new slope for Fe^{III}-DOM complexes, log K values for Fe^{II} are calculated from the known ratios of log K (Fe^{III}/ Fe^{II}) (Table 5.2), since two out of three variables are known. Estimated stability constants for Fe^{II}-DOM complexes follow a similar trend to Fe^{III}, with exceedingly weak complexation occurring at pH 4, while stronger complexes form at higher pH.

Table 5.3 Known and predicted stability constants for Fe^{II} and Fe^{III} ligands in our study, along with their stability constant ratios. Reported stability constants for model ligands and DOM isolates are thermodynamic.

Model Ligand	**log K_{FeII}**	**log K_{FeIII}**	**log K (Fe^{III}/Fe^{II})**
1. Acetate	**1.4**	**4.24**	**2.35**
2. Oxalate	**3.97**	**9.15**	**5.09**
3. Citrate	**5.89**	**13.13**	**7.21**
4. NTA	**10.18**	**17.82**	**7.64**
5. $Oxalate_2$	**5.9**	**15.45**	**9.45**
6. NTA_2	**12.62**	**25.92**	**11.16**
7. EDTA	**16.01**	**27.66**	**11.65**
pH 4			
8. SRNOM	**2.81**	**5.77**	**2.96**
9. SRFA	**2.12**	**4.79**	**2.67**
10. SRHA	**2.27**	**5.03**	**2.76**
pH 8			
11. SRNOM	**17.58**	**30.25**	**12.67**
12. SRFA	**17.79**	**30.59**	**12.80**
13 .SRHA	**17.02**	**29.33**	**12.31**

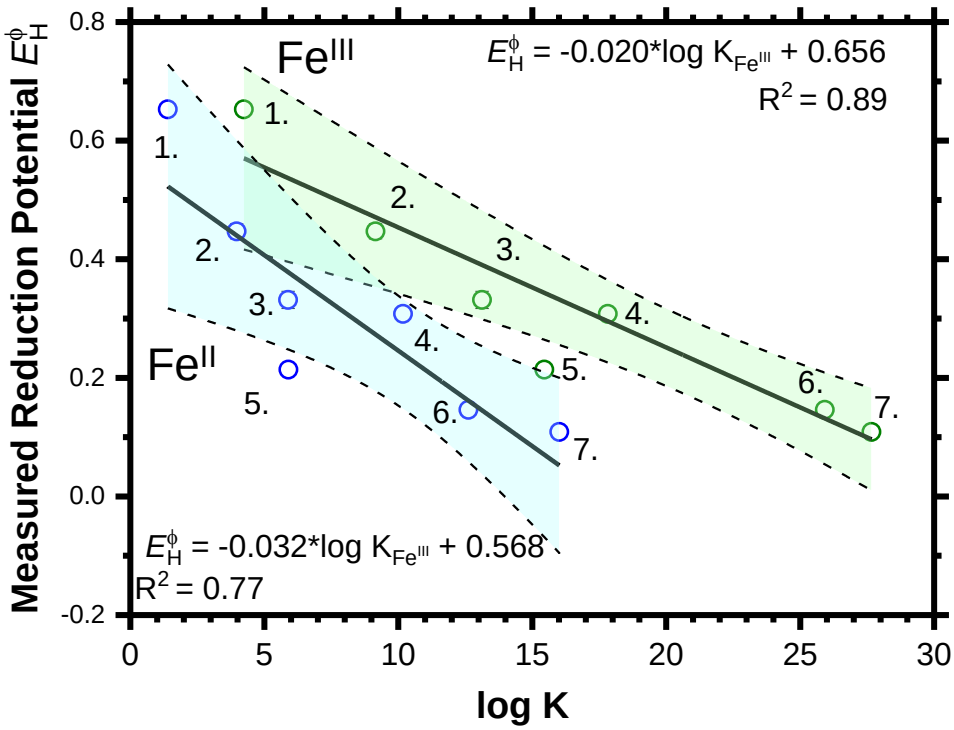

Figure 5.4 Linear relationships obtained for individual Fe-model ligand complexes. Slopes obtained for each linear regression are reported below and above their regressions, respectively. Green circles represent log K values for 7 model ligands with Fe^{III}, while blue circles represent log K values for 7 model ligands with Fe^{II}. Error bars, which represent one standard deviation, are hidden within circles in most cases. Numbers next to associated data points represent model ligands listed in Table 5.3

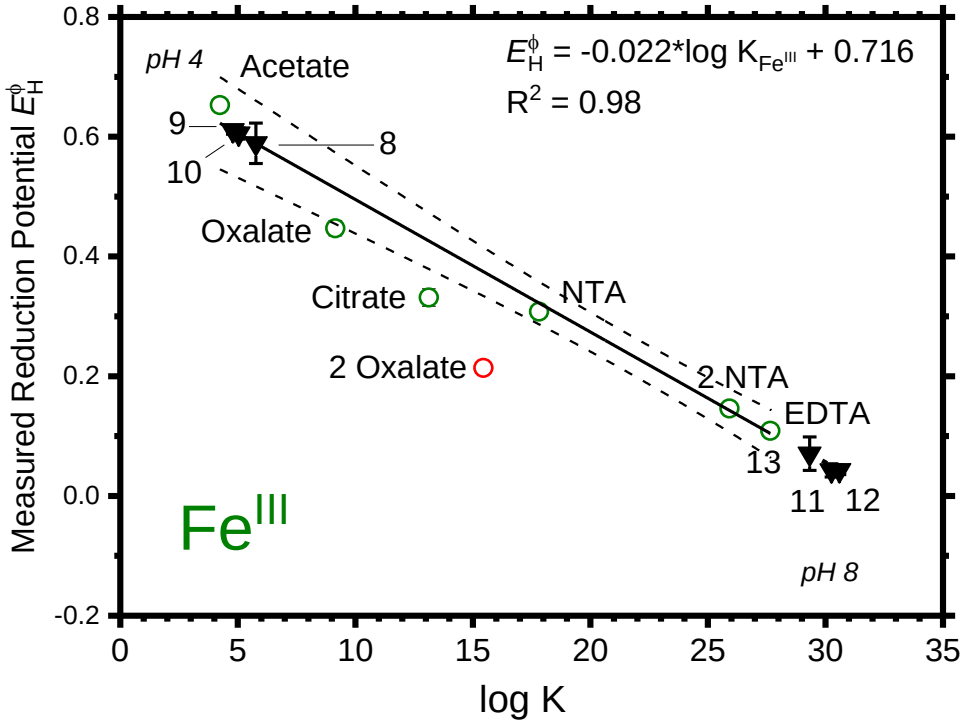

Figure 5.5 Optimized linear regression with log K values for Fe^{III}-DOM complexes as determined by measured reduction potentials against the slope (equation in top right) reported with thermodynamic stability constants of model ligands (green circles). The red circle for the bisoxalatoferrate complex was omitted from the analysis to optimize the regression. Our data set at pH 8 lies slightly outside the linear regression, although likely are within the reported 95% confidence interval (dotted lines). Error bars in some cases are within circles..

5.3.4 Conclusion and environmental implications

Our preliminary data shows that DOM can influence abiotic Fe^{II} oxidation extent in two different pH conditions. Additionally, a previously obtained relationship with model organic ligands that relates measured reduction potentials of Fe-L complexes to the ratio of their reported thermodynamic stability constants can be

exploited to estimate unknown thermodynamic stability constants of individual Fe^{III} and Fe^{II} DOM complexes. Future work will survey more DOM isolates that vary in their composition using our obtained linear relationships. Additionally, some subsamples of DOM will be pre-treated with cation exchange resins to remove pre-existing cations (e.g., iron, manganese, etc.) that are naturally present before use in experiments. Other experiments with DOM could be performed in the presence of different buffers or solution conditions (e.g. varying ionic strength, carbonate) to simulate natural aquatic environments. Overall, we feel that this work represents a step forward in understanding the nature iron binding and redox-reactivity in the environment, which are critical for controlling biogeochemical processes that influence carbon and nutrient cycling, as well as pollutant dynamics [57,128,130].

Chapter 6

SUMMARY AND OUTLOOK

This dissertation primarily focused on the application of two electrochemical methods to study large (global) and small (molecular) scale biogeochemical processes as summarized in Chapter 1. In the second chapter, voltammetric microelectrodes were used with a pump profiling system to measure redox gradients and other constituents in Chesapeake Bay. Spatiotemporal relationships in gradients related to stratification were observed and large-scale biogeochemical processes were observed. In the third chapter, high vertical resolution benthic redox gradients were once again measured using voltammetric microelectrodes in order to look at relationships between sediment geochemistry and native microbial communities in Arctic porewaters. Results from *in situ* analyses shed light into the influence of iron redox cycling on carbon cycles. In the fourth chapter, MEO is used as a tool to directly observe Fe^{II} oxidation extent in the presence of organic ligands across a range of thermodynamic boundary conditions (i.e., E_H and pH). Measured redox potentials from experiment oxidation peaks formed a Nernstian relationship with reported ratios of iron stability constants (log K_{FeIII}/logK_{FeII}) that allow for the determination of stability constant ratios of unknown ligands. Finally, in the fifth chapter, Fe^{II} oxidation in the presence of three DOM isolates is performed at two fixed E_H (+0.61, +0.0V) and pH (4, 8) conditions. Using E_H^{ϕ} values of Fe-DOM complexes obtained from experiments, an individual linear relationship is developed and enables for the determination of unknown log K values for Fe^{III}-DOM stability constants. The ability

to determine stability constants for Fe-DOM complexes is critical for predicting iron speciation and its bioavailability in aquatic environments.

Application of these two electrochemical methods is anticipated in the future to advance our understanding of large- and small-scale biogeochemical processes. Some direct applications of voltammetry and MEA that will likely be used are the following:

6.1 Relationships between iron and carbon cycles in Arctic lacustrine porewaters and permafrost thaw zones

Given the ability of voltammetry to measure in situ redox gradients with high vertical resolution (<1 mm), it is likely that voltammetry measurements will be paired with other analyses (e.g., metagenomics, dissolved organic carbon concentration and composition) in many future investigations in order to decipher the relationships between iron and carbon cycles. The relationships between these two cycles are important due to the deleterious effects of greenhouse gas emissions that are associated with shifting carbon cycles due to climate change. For instance, reducing conditions in soil porewaters promoted by the onset of permafrost thaw would lead to the reductive dissolution of iron minerals and a release of organic carbon, which could lead to an increase in dissolved Fe(II) and aqueous Fe(III)-organic complexes, both which could be detected and measured via voltammetry. The interplay between microbially-mediated organic carbon oxidation, promoted by Fe(III) reduction, as well as abiotic and biologically-mediated Fe(II) oxidation, may determine the type and amount of GHGs emitted (e.g. CO2, CH4). Additionally, voltammetric microelectrodes can be employed in laboratory column studies (pseudo in situ) that further constrain factors encountered in the field. When coupled with metagenomic analyses of methanotrophic or methanogenic communities, pH, and DOC

measurements, high-resolution TEA measurements at redox interfaces will enable investigators to determine if iron reduction suppresses or enhances methane and carbon dioxide formation [181].

6.2 Influence of organic acids on dissolution of iron minerals

MEA can be utilized as a tool to investigate the influence of organic acids and DOM on the reductive dissolution of iron(oxyhydro-)oxide minerals, or conversely, the oxidative dissolution of pyrite [208]. While the work presented in this dissertation focused on aqueous Fe(II) organic complexes, it is likely that ligands can be employed into electrochemical cells in a similar manner to investigate how redox-properties of these ligand complexes effect dissolution of solid-phase iron minerals. Indeed, previous studies that have studied iron oxide reducibility under fixed thermodynamic boundary conditions have used mediated electrochemical reduction to reduce ferrihydrite, goethite, and hematite in the presence of phenanthroline, an Fe(II)-stabilizing ligand [11]. Phenanthroline increased reducibility of the iron oxides because Fe(II) was bound to the ligand instead of being associated with Fe(III)-oxide surfaces (i.e., increased the thermodynamic driving force behind reduction). In a similar manner, pyrite oxidation in the presence of model organic ligands could be investigated using MEA. Previous kinetic studies have indicated that model organic ligands can catalyze pyrite oxidative dissolution, depending on the redox potential of the iron-ligand complex [182]. MEO could be utilized as an experimental system to observe these effects under fixed thermodynamic boundary conditions (i.e., pH, E_H).

6.3 Redox properties of iron-organic matter associations

Amorphous iron oxides and poorly crystalline ferrihydrite commonly forms at redox interfaces in aquatic and soil environments. Measured redox potentials (EH) of ferrihydrite are higher than crystalline Fe(III) mineral phases due to the thermodynamic instability associated with the amorphous structure as opposed to more ordered minerals. In the environment, organic carbon coexists and often coprecipitates with iron at redox interfaces. These iron-organic matter (Fe-OM) associations play a pivotal role in carbon stabilization, which have large implications for climate change research. Additionally, organic carbon can alter iron mineral crystallinity, which could change redox properties (EH) of the Fe-OM associations. Understanding the redox properties of these Fe-OM associations is crucial, as they could control abiotic and biotic reductive dissolution and phase transformations, which could influence the bioavailability and fate of coprecipitated organic carbon, as well as attenuation of pollutants [20]. Using MEA (both MEO and MER), the redox properties of these iron-OM associations, which are largely unknown, can be measured. Fe-OM associations or coprecipitates can systematically be built with model ligands used in the previous chapters in this dissertation and measured redox properties could be paired with synchrotron analyses in order to understand the crystallinity and coordination environment of iron within coprecipitates.

REFERENCES

1. Bard, A.J. and Faulkner, L.R. (2000) Electrochemical Methods: Fundamentals and Applications. 2nd Edition, Wiley, New York.

2. Luther III, G.W., Glazer, B.T., Ma, S., Trouwborst, R.E., Moore, T.S., Metzger, E., Kraiya, C., Waite, T.J., Druschel, G., Sundby, B. and Taillefert, M., 2008. Use of voltammetric solid-state (micro) electrodes for studying biogeochemical processes: laboratory measurements to real time measurements with an in situ electrochemical analyzer (ISEA). Marine Chemistry, 108(3-4), pp.221-235.

3. Aeschbacher, M., Sander, M. and Schwarzenbach, R.P., 2010. Novel electrochemical approach to assess the redox properties of humic substances. Environmental science & technology, 44(1), pp.87-93.

4. Sander, M., Hofstetter, T.B. and Gorski, C.A., 2015. Electrochemical analyses of redox-active iron minerals: a review of nonmediated and mediated approaches. Environmental science & technology, 49(10), pp.5862-5878.

5. Luther III, G.W., Mullaugh, K.M., Hauser, E.J., Rader, K.J. and Di Toro, D.M., 2021. Determination of ambient dissolved metal ligand complexation parameters via kinetics and pseudo-voltammetry experiments. Marine Chemistry, 234, p.103998.

6. Ceresa, A., Bakker, E., Hattendorf, B., Günther, D. and Pretsch, E., 2001. Potentiometric polymeric membrane electrodes for measurement of environmental samples at trace levels: New requirements for selectivities and measuring protocols, and comparison with ICPMS. Analytical chemistry, 73(2), pp.343-351.

7. Bakker, E. and Pretsch, E., 2007. Modern potentiometry. Angewandte Chemie International Edition, 46(30), pp.5660-5668.

8. Croot, P.L. and Johansson, M., 2000. Determination of iron speciation by cathodic stripping voltammetry in seawater using the competing ligand 2-(2-Thiazolylazo)-p-cresol (TAC). Electroanalysis: An International Journal Devoted to Fundamental and Practical Aspects of Electroanalysis, 12(8), pp.565-576.

9. Donat, J.R., Lao, K.A. and Bruland, K.W., 1994. Speciation of dissolved copper and nickel in South San Francisco Bay: a multi-method approach. Analytica Chimica Acta, 284(3), pp.547-571.

10. Gorski, C.A., Edwards, R., Sander, M., Hofstetter, T.B. and Stewart, S.M., 2016. Thermodynamic characterization of iron oxide–aqueous Fe2+ redox couples. Environmental science & technology, 50(16), pp.8538-8547.

11. Aeppli, M., Voegelin, A., Gorski, C.A., Hofstetter, T.B. and Sander, M., 2018. Mediated electrochemical reduction of iron (oxyhydr-) oxides under defined thermodynamic boundary conditions. Environmental science & technology, 52(2), pp.560-570.

12. Yücel, M., Gartman, A., Chan, C.S. and Luther, G.W., 2011. Hydrothermal vents as a kinetically stable source of iron-sulphide-bearing nanoparticles to the ocean. *Nature Geoscience*, *4*(6), pp.367-371.

13. MacDonald, D.J., Findlay, A.J., McAllister, S.M., Barnett, J.M., Hredzak-Showalter, P., Krepski, S.T., Cone, S.G., Scott, J., Bennett, S.K., Chan, C.S. and Emerson, D., 2014. Using in situ voltammetry as a tool to identify and characterize habitats of iron-oxidizing bacteria: from fresh water wetlands to hydrothermal vent sites. *Environmental Science: Processes & Impacts*, *16*(9), pp.2117-2126.

14. Jones, M.E., Nico, P.S., Ying, S., Regier, T., Thieme, J. and Keiluweit, M., 2018. Manganese-driven carbon oxidation at oxic–anoxic interfaces. *Environmental science & technology*, *52*(21), pp.12349-12357.

15. Brendel, P.J. and Luther, G.W.I., 1995. Development of a gold amalgam voltammetric microelectrode for the determination of dissolved Fe, Mn, O2, and S (-II) in porewaters of marine and freshwater sediments. *Environmental science & technology*, *29*(3), pp.751-761.

16. Gorski, C.A., Aeschbacher, M., Soltermann, D., Voegelin, A., Baeyens, B., Marques Fernandes, M., Hofstetter, T.B. and Sander, M., 2012. Redox properties of structural Fe in clay minerals. 1. Electrochemical quantification of electron-donating and-accepting capacities of smectites. *Environmental science & technology*, *46*(17), pp.9360-9368.

17. Lau, M.P., Sander, M., Gelbrecht, J. and Hupfer, M., 2015. Solid phases as important electron acceptors in freshwater organic sediments. *Biogeochemistry*, *123*(1), pp.49-61.

18. Hudson, J.M., MacDonald, D.J., Estes, E.R. and Luther III, G.W., 2019. A durable and inexpensive pump profiler to monitor stratified water columns with high vertical resolution. *Talanta*, *199*, pp.415-424.

19. Hudson, J.M., Michaud, A.B., Emerson, D. and Chin, Y.P., 2022. Spatial distribution and biogeochemistry of redox active species in arctic sedimentary porewaters and seeps. *Environmental Science: Processes & Impacts*.

20. Poggenburg, C., Mikutta, R., Sander, M., Schippers, A., Marchanka, A., Dohrmann, R. and Guggenberger, G., 2016. Microbial reduction of ferrihydrite-organic matter coprecipitates by Shewanella putrefaciens and Geobacter metallireducens in comparison to mediated electrochemical reduction. *Chemical Geology*, *447*, pp.133-147.

21. Stumm, W., & Morgan, J. J. (1996). Aquatic Chemistry, John Wiley & Sons. *Inc., New York*.

22. Glazer, B. T., Marsh, A. G., Stierhoff, K., & Luther III, G. W. (2004). The dynamic response of optical oxygen sensors and voltammetric electrodes to temporal changes in dissolved oxygen concentrations. *Analytica chimica acta*, *518*(1-2), 93-100.

23. Findlay, A. J., Di Toro, D. M., & Luther, G. W. (2017). A model of phototrophic sulfide oxidation in a stratified estuary. *Limnology and Oceanography*, *62*(5), 1853-1867.

24. Findlay, A. J., Bennett, A. J., Hanson, T. E., & Luther, G. W. (2015). Light-dependent sulfide oxidation in the anoxic zone of the Chesapeake Bay can be explained by small populations of phototrophic bacteria. *Applied and environmental microbiology*, AEM-02062.

25. Oldham, V. E., Jones, M. R., Tebo, B. M., & Luther III, G. W. (2017). Oxidative and reductive processes contributing to manganese cycling at oxic-anoxic interfaces. *Marine Chemistry*, *195*, 122-128.

26. Field, E. K., Kato, S., Findlay, A. J., MacDonald, D. J., Chiu, B. K., Luther III, G. W., & Chan, C. S. (2016). Planktonic marine iron oxidizers drive iron mineralization under low-oxygen conditions. *Geobiology*, *14*(5), 499-508.

27. Luther III, G. W., Catalano, G., De Lange, G. J., & Woittiez, J. R. W. (1990). Reduced sulfur in the hypersaline anoxic basins of the Mediterranean Sea. *Marine Chemistry*, *31*(1-3), 137-152.

28. Herman, A. W., Mitchell, M. R., & Young, S. W. (1984). A continuous pump sampler for profiling copepods and chlorophyll in the upper oceanic layers. *Deep Sea Research Part A. Oceanographic Research Papers*, *31*(4), 439-450

29. Codispoti, L. A., Friederich, G. E., Murray, J. W., & Sakamoto, C. M. (1991). Chemical variability in the Black Sea: implications of continuous vertical profiles that penetrated the oxic/anoxic interface. *Deep Sea Research Part A. Oceanographic Research Papers, Suppl. 2*, *38*, S691-S710.

30. Friederich, G. E., & Codispoti, L. A. (1987). An analysis of continuous vertical nutrient profiles taken during a cold-anomaly off Peru. *Deep Sea Research Part A. Oceanographic Research Papers*, *34*(5-6), 1049-1065.

31. Cline, J. D. (1969). Spectrophotometric determination of hydrogen sulfide in natural waters. *Limnology and Oceanography*, *14*(3), 454-458.

32. Stookey, L. L. (1970). Ferrozine---a new spectrophotometric reagent for iron. *Analytical chemistry*, *42*(7), 779-781.

33. Carpenter, J. H. (1965). The accuracy of the Winkler method for dissolved oxygen analysis. *Limnology and Oceanography*, *10*(1), 135-140.

34. McAdams, B. C., Adams, R. M., Arnold, W. A., & Chin, Y. P. (2016). Novel insights into the distribution of reduced sulfur species in prairie pothole wetland pore waters provided by bismuth film electrodes. *Environmental Science & Technology Letters*, *3*(3), 104-109.

35. Luther III, G. W., Glazer, B. T., Hohmann, L., Popp, J. I., Taillefert, M., Rozan, T. F., Brendel, P.J., Theberge, S.M. & Nuzzio, D. B. (2001). Sulfur speciation monitored in situ with solid state gold amalgam voltammetric microelectrodes: polysulfides as a special case in sediments, microbial mats and hydrothermal vent waters Presented at the Whistler 2000 Speciation Symposium, Whistler Resort, BC, Canada, June 25–July 1, 2000. Electronic Supplementary Information available. See http://www. rsc. org/suppdata/em/b0/b006499h. *Journal of Environmental Monitoring*, *3*(1), 61-66.

36. Luther, G. W., Bono, A. B., Taillefert, M., Cary, S. C., Taillefert, M., & Rozan, T. (2002). A Continuous Flow Electrochemical Cell for Analysis of Chemical Species and Ions at High Pressure: Laboratory, Shipboard, and Hydrothermal Vent Results. In *ACS SYMPOSIUM SERIES* (Vol. 811, pp. 54-72). Washington, DC; American Chemical Society; 1999.

37. Luther III, G. W., Rozan, T. F., Taillefert, M., Nuzzio, D. B., Di Meo, C., Shank, T. M., Lutz, R.A. & Cary, S. C. (2001). Chemical speciation drives hydrothermal vent ecology. *Nature*, *410*(6830), 813.

38. Dayton, M. A., Brown, J. C., Stutts, K. J., & Wightman, R. M. (1980). Faradaic electrochemistry at microvoltammetric electrodes. *Analytical Chemistry*, *52*(6), 946-950.

39. Oldham, V. E., Owings, S. M., Jones, M. R., Tebo, B. M., & Luther, G. W. (2015). Evidence for the presence of strong Mn (III)-bindidng ligands in the water column of the Chesapeake Bay. *Marine Chemistry*, *171*, 58-66.

40. K. Grasshoff, "Determination of Nitrite, Nitrate, Oxygen, Thiosulphate," In: K. Grasshoff, M. Ehrhardt and K. Kremling, Eds., *Methods of Seawater Analysis*, Verlag Chemie Weinheim, New York, 1983, pp. 61-72, 81-84, 139-150.

41. Brendel, P. J. (1995). Development of a mercury thin film voltammetric microelectrode for the determination of biogeochemically important redox species in porewaters of marine and freshwater sediments. PhD dissertation, University of Delaware.

42. Weiss, R. F. (1970, August). The solubility of nitrogen, oxygen and argon in water and seawater. In *Deep Sea Research and Oceanographic Abstracts* (Vol. 17, No. 4, pp. 721-735). Elsevier.

43. Bellmyer, J. (2018, July 23). Official: Dam gates opening no cause for concern. *Cecil Daily*. Retrieved December 13, 2018, from https://www.cecildaily.com/spotlight/official-dam-gates-opening-no-cause-for-concern/article_17c17a37-ef58-516d-bf10-a6afa0145ede.html

44. Luther, G. W., & Popp, J. I. (2002). Kinetics of the abiotic reduction of polymeric manganese dioxide by nitrite: an anaerobic nitrification reaction. *Aquatic Geochemistry*, *8*(1), 15-36.

45. Yücel, M., Beaton, A. D., Dengler, M., Mowlem, M. C., Sohl, F., & Sommer, S. (2015). Nitrate and nitrite variability at the seafloor of an oxygen minimum zone revealed by a novel microfluidic in-situ chemical sensor. *PloS one*, *10*(7), e0132785.

46. Giblin, A. E., Tobias, C. R., Song, B., Weston, N., Banta, G. T., & H. RIVERA-MONROY, V. I. C. T. O. R. (2013). The importance of dissimilatory nitrate reduction to ammonium (DNRA) in the nitrogen cycle of coastal ecosystems. *Oceanography*, *26*(3), 124-131.

47. Moore, T. S., Nuzzio, D. B., Di Toro, D. M., & Luther III, G. W. (2009). Oxygen dynamics in a well mixed estuary, the lower Delaware Bay, USA. *Marine Chemistry*, *117*(1-4), 11-20.

48. Konovalov, S. K., Luther, G. I. W., Friederich, G. E., Nuzzio, D. B., Tebo, B. M., Murray, J. W., Oguz, T., Glazer, B., Trouwborst, R.E., Clement, B. & Murray, K. J. (2003). Lateral injection of oxygen with the Bosporus plume—fingers of oxidizing potential in the Black Sea. *Limnology and Oceanography*, *48*(6), 2369-2376.

49. Glazer, B. T., Luther III, G. W., Konovalov, S. K., Friederich, G. E., Nuzzio, D. B., Trouwborst, R. E., Tebo, B.M., Clement, B., Murray, K. & Romanov, A. S. (2006). Documenting the suboxic zone of the Black Sea via high-resolution real-time redox profiling. *Deep Sea Research Part II: Topical Studies in Oceanography*, *53*(17-19), 1740-1755.

50. A. Trusiak, L.A. Treibergs, G.W. Kling, and R.M. Cory, The role of iron and reactive oxygen species in the production of CO_2 in arctic soil waters, *Geochim. Cosmochim. Acta*, 2018, **224**, 80-95.

51. S. MacIntyre, A. Cortés, and S. Sadro, Sediment respiration drives circulation and production of CO_2 in ice-covered Alaskan Arctic lakes, *Limnol. Oceanogr. Lett.*, 2018, **3**, 302-310.

52. L. Klüpfel, A. Piepenbrock, A. Kappler, and M. Sander, Humic substances as fully regenerable electron acceptors in recurrently anoxic environments, *Nat. Geosci.*, 2014, **7**, 195-200.

53. K.M. Walter, S.A. Zimov, J.P. Chanton, D. Verbyla, and F.S. Chapin, Methane bubbling from Siberian thaw lakes as a positive feedback to climate warming, *Nature*, 2006, **443**, 71-75.

54. P.B. Matheus Carnevali, M. Rohrssen, M.R. Williams, A.B. Michaud, H. Adams, D. Berisford, G.D. Love, J.C. Priscu, O. Rassuchine, K.P. Hand, and A.E. Murry, Methane sources in arctic thermokarst lake sediments on the North Slope of Alaska, *Geobiology*, 2015, **13**, 181-197.

55. B. Braune, J. Chételat, M. Amyot, T. Brown, M. Clayden, M. Evans, A. Fisk, A. Gaden, C. Girard, A. Hare, and J. Kirk, Mercury in the marine environment of the Canadian Arctic: review of recent findings, *Sci. Total Environ*, 2015, **509**, 67-90.

56. D. Emerson, J.J. Scott, J. Benes, and W.B. Bowden, Microbial iron oxidation in the arctic tundra and its implications for biogeochemical cycling, *Appl. Environ. Microbiol.*, 2015, **81**, 8066-8075.

57. T. Borch, R. Kretzschmar, A. Kappler, P.V. Cappellen, M. Ginder-Vogel, A. Voegelin, and K. Campbell, Biogeochemical redox processes and their impact on contaminant dynamics, *Environ. Sci. Technol.*, 2010, **44**, 15-23.

58. D.A. Lipson, M. Jha, T.K. Raab, and W.C. Oechel, Reduction of iron (III) and humic substances plays a major role in anaerobic respiration in an Arctic peat soil. *J. Geophys. Res.: Biogeosci*, 2010, **115**, 1-13.

59. K.E. Miller, C.T. Lai, E.S. Friedman, L.T. Angenent, and D.A. Lipson, Methane suppression by iron and humic acids in soils of the Arctic Coastal Plain, *Soil Biol. Biochem*., 2015, **83**, 176-183.

60. J.C. Cornwell, Ph.D. Thesis, University of Alaska Fairbanks, 1983.

61. J.C. Cornwell and G.W. Kipphut, Biogeochemistry of manganese-and iron-rich sediments in Toolik Lake, Alaska, In *Toolik Lake. Developments in Hydrobiology*, **78**, 45-59.

62. S.E. Page, G.W. Kling, M. Sander, K.H. Harrold, J.R. Logan, K. McNeill, and R.M.Cory, Dark formation of hydroxyl radical in Arctic soil and surface waters, *Environ. Sci. Technol.*, 2013, **47**, 12860-12867.

63. M. Keiluweit, P.S. Nico, M. Kleber, and S. Fendorf, Are oxygen limitations under recognized regulators of organic carbon turnover in upland soils? *Biogeochemistry*, 2016, **127**, 157-171.

64. J.L. Wilmouth, J.K. Schaefer, D.R. Schlesinger, S.W. Roth, P.G. Hatcher, J.K. Shoemaker, and X. Zhang, The role of oxygen in stimulating methane production in wetlands, *Global Change Biology*, 2021, **27**, 5831-5847.

65. K. Laufer, A.B. Michaud, H. Røy, and B.B. Jørgensen, Reactivity of Iron Minerals in the Seabed Toward Microbial Reduction–A Comparison of Different Extraction Techniques, *Geomicrobiol. J*., 2020, **37**, 170-189.

66. J. Seeberg-Elverfieldt, M. Schlüter, T. Feseker, and M. Kölling, Rhizon sampling of porewaters near the sediment-water interface of aquatic systems, *Limnol. Oceanogr. Methods*, 2005, **3**, 361-371.

67. G.W. Luther, P.J. Brendel, B.L. Lewis, B. Sundby, L. Lefrançois, N. Silverberg, D.B. Nuzzio, Simultaneous measurement of O_2, Mn, Fe, I^-, and S (—II) in marine pore waters with a solid-state voltammetric microelectrode, *Limnol. Oceanogr.*, 1998, **43**, 325-333.

68. G.W. Luther, T.F. Rozan, M. Taillefert, D.B. Nuzzio, C. Di Meo, T.M. Shank, R.A. Lutz, and S.C. Cary, Chemical speciation drives hydrothermal vent ecology, *Nature*, 2001, **410**, 813-816.

69. D.B. Nuzzio, M. Taillefert, S.C. Cary, A.L. Reysenbach, and G.W. Luther, *In situ* voltammetry at deep-sea hydrothermal vents, *Environmental Electrochemistry, ACS Symposium Series*, 2002, **811**, 40-51.

70. S. Ma, G.W. Luther, J. Keller, A.S. Madison, E. Metzger, D. Emerson, and J.P. Megonigal, Solid-State Au/Hg Microelectrode for the Investigation of Fe and Mn Cycling in a Freshwater Wetland: Implications for Methane Production, *Electroanalysis*, 2008, **20**, 233-239.

71. L. Smith, M.C. Watzin, and G. Druschel, Relating sediment phosphorus mobility to seasonal and diel redox fluctuations at the sediment–water interface in a eutrophic freshwater lake, *Limnol. Oceanogr.*, 2011, **56**, 2251-2264.

72. A.W. Schroth, C.D. Giles, P.D. Isles, Y. Xu, Z. Perzan, and G.K. Druschel, Dynamic coupling of iron, manganese, and phosphorus behavior in water and sediment of shallow ice-covered eutrophic lakes, *Environ. Sci. Technol.*, 2015, **49**, 9758-9767.

73. C.D. Giles, P.D. Isles, T. Manley, Y. Xu, G.K. Druschel, and A.W. Schroth, The mobility of phosphorus, iron, and manganese through the sediment–water continuum of a shallow eutrophic freshwater lake under stratified and mixed water-column conditions, *Biogeochemistry*, 2016, **127**, 15-34.

74. A. Paytan, A.L. Lecher, N. Dimova, K.J. Sparrow, F.G.T. Kodovska, J. Murray, S. Tulaczyk, and J.D. Kessler, Methane transport from the active layer to lakes in the Arctic using Toolik Lake, Alaska, as a case study, *PNAS*, 2015, **112**, 3636-3640.

75. A.L. Lecher, P.C. Chuang, M. Singleton, and A. Paytan, Sources of methane to an Arctic lake in Alaska: An isotopic investigation, *J. Geophys. Res.: Biogeosci*, 2017, **122**, 753-766.

76. M. Taillefert, A.B. Bono, and G.W. Luther, Reactivity of freshly formed Fe (III) in synthetic solutions and (pore) waters: voltammetric evidence of an aging process, *Environ. Sci. Technol.*, 2000, **34**, 2169-2177.

77. K. Porsch, and A. Kappler, Fe(II) oxidation by molecular O_2 during HCl extraction, *Environ. Chem.*, 2011, **8**, 190-197.

78. P.D. Schloss, S.L. Westcott, T. Ryabin, J.R. Hall, M. Hartmann, E.B. Hollister, R.A. Lesniewski, B.B. Oakley, D.H. Parks, C.J. Robinson, and J.W. Sahl, Introducing mothur: open-source, platform-independent, community-supported software for describing and comparing microbial communities, *Appl. Environ. Microbiol.*, 2009, **75**, 7537-7541.

79. C. Quast, E. Pruesse, P. Yilmaz, J. Gerken, T. Schweer, P. Yarza, J. Peplies, and F.O. Glöckner, The SILVA ribosomal RNA gene database project: improved data processing and web-based tools, *Nucleic Acids Res.*, 2013, **41**, D590-D596.

80. R.A. Berner, in *Early diagenesis: a Theoretical Approach*, ed. Princeton University Press, 1980, vol. 1.

81. D. Joung, M. Leduc, B. Ramcharitar, Y. Xu, P.D. Isles, J.D. Stockwell, G.K. Druschel, T. Manley, and A.W. Schroth, Winter weather and lake-watershed physical configuration drive phosphorus, iron, and manganese dynamics in water and sediment of ice-covered lakes, *Limnol. Oceanogr.*, 2017, **62**, 1620-1635.

82. A.S. Madison, B.M. Tebo, A. Mucci, B. Sundby, and G.W. Luther, Abundant porewater Mn (III) is a major component of the sedimentary redox system, *Science*, 2013, **341**, 875-878.

83. T.D. Hamilton, Ph.D. Thesis, University of Alaska Institute of Arctic Biology, 2003.

84. G.W. Luther, P.A. Shellenbarger, and P.J. Brendel, Dissolved organic Fe (III) and Fe (II) complexes in salt marsh porewaters, *Geochim. Cosmochim. Acta*, 1996, **60**, 951-960.

85. M. Taillefert, V.C. Hover, T.F. Rozan, S.M. Theberge, and G.W. Luther, The influence of sulfides on soluble organic-Fe (III) in anoxic sediment porewaters, *Estuaries*, 2002, **25,** 1088-1096.

86. J.A. Hakala, R.L. Fimmen, Y.P. Chin, S.G. Agrawal, and C.P. Ward, Assessment of the geochemical reactivity of Fe-DOM complexes in wetland sediment pore waters using a nitroaromatic probe compound, *Geochim. Cosmochim. Acta*, 2009, **73**, 1382-1393.

87. A.E. Mutschlecner, J.J. Guerard, J.B. Jones, and T.K. Harms, Regional and intra-annual stability of dissolved organic matter composition and biolability in high-latitude Alaskan rivers, *Limnol. Oceanogr.*, 2018, **63**, 1605-1621.

88. K.R. Gagné, S.C. Ewers, C.J. Murphy, R. Daanen, K.W. Anthony, and J.J. Guerard, Composition and photo-reactivity of organic matter from permafrost soils and surface waters in interior Alaska, *Environ. Sci.: Processes Impacts*, 2020, **22**, 1525-1539.

89. E.N. MacDonald, S.E. Tank, S.V. Kokelj, D.G. Froese, and R.H. Hutchins, Permafrost-derived dissolved organic matter composition varies across permafrost end-members in the western Canadian Arctic, *Environ. Res. Lett.*, 2021, **16**, 024036

90. A. Kappler and K.L. Straub, Geomicrobiological cycling of iron, *Rev. Mineral. Geochem.*, 2005, **59**, 85-108.

91. S.C. Whalen and V. Alexander, Seasonal inorganic carbon and nitrogen transport by phytoplankton in an arctic lake, *Can. J. Fish. Aquat. Sci.*, 1986, **43**,1177-1186.

92. J.R. Haas and T.J. Dichristina, Effects of Fe (III) chemical speciation on dissimilatory Fe (III) reduction by Shewanella putrefaciens, *Environ. Sci. Technol.*, 2002, **36**, 373-380.

93. M. Taillefert, J.S. Beckler, E. Carey, J.L. Burns, C.M. Fennessey, and T.J. DiChristina, Shewanella putrefaciens produces an Fe (III)-solubilizing organic ligand during anaerobic respiration on insoluble Fe (III) oxides, *J. Inorg. Biochem*., 2007, **101**, 1760-1767.

94. B.J. Campbell, L. Yu, J.F. Heidelberg and D.L. Kirchman, Activity of abundant and rare bacteria in a coastal ocean, *PNAS*, 2011, **108**, 12776-12781.

95. M.D. Lynch and J.D. Neufeld, Ecology and exploration of the rare biosphere, *Nat. Rev. Microbiol.*, 2015, **13**, 217-229.

96. R. Props, F.M. Kerckhof, P. Rubbens, J. De Vrieze, E.H. Sanabria, W. Waegeman, P. Monsieurs, F. Hammes, and N. Boon, Absolute quantification of microbial taxon abundances, *ISME J.*, 2017, **11**, 584-587.

97. G.K. Druschel, D. Emerson, R. Sutka, P. Suchecki, and G.W. Luther, Low-oxygen and chemical kinetic constraints on the geochemical niche of neutrophilic iron (II) oxidizing microorganisms, *Geochim. Cosmochim. Acta*, 2008, **72**, 3358-3370.

98. M.M. Urrutia, E.E. Roden and J.M. Zachara, Influence of aqueous and solid-phase Fe (II) complexants on microbial reduction of crystalline iron (III) oxides, *Environ. Sci. Technol.*, 1999, **33**, 4022-4028.

99. D. Sobolev and E.E. Roden, Evidence for rapid microscale bacterial redox cycling of iron in circumneutral environments, *Antonie Van Leeuwenhoek*, 2002, **81**, 587-597.

100. E. Roden, J.M. McBeth, M. Blothe, E.M. Percak-Dennet, E.J. Flemming, R.R. Holyoke, G.W. Luther and D. Emerson, The microbial ferrous wheel in a neutral pH groundwater seep, *Frontiers in Microbiology*, 2012, **3**, 172.

101. W.C. Lin, M.V. Coppi and D.R. Lovley, Geobacter sulfurreducens can grow with oxygen as a terminal electron acceptor, *Appl. Environ. Microbiol.*, 2004, **70**, 2525-2528.

102. Y. Liu, in Taxonomy of Methanogens. Handbook of Hydrocarbon and Lipid Microbiology, ed. Springer Berlin Heidelberg , 2010, pp. 547-558.

103. S. Bräuer, H. Cadillo-Quiroz, E. Yashiro, J.B. Yavitt and S.H. Zinder, Isolation of a novel acidophilic methanogen from an acidic peat bog, *Nature*, 2006, **442**, 192-194.

104. M. Patzner, M. Logan, A. McKenna, R. Young, Z. Zhou, H. Joss, C. Mueller, C. Hoschen, T. Scholten, D. Straub and S. Kleindienst, Microbial iron (III) reduction during palsa collapse promotes greenhouse gas emissions before complete permafrost thaw, *Eartharxiv*, 2021, DOI: 10.21203/rs.3.rs-691992/v1.

105. K.A. Bretz and S.C. Whalen, Methane cycling dynamics in sediments of Alaskan Arctic Foothill lakes, *Inland Waters*, 2014, **4**, 65-78.

106. J.D. Coates, D.J. Ellis, C.V. Gaw and D.R. Lovley, Geothrix fermentans gen. nov., sp. nov., a novel Fe (III)-reducing bacterium from a hydrocarbon-contaminated aquifer, *Int. J. Syst. Evol. Microbiol.*, 1999, **49**, 1615-1622.

107. C. Knief, Diversity and habitat preferences of cultivated and uncultivated aerobic methanotrophic bacteria evaluated based on pmoA as molecular marker, *Frontiers in Microbiology*, 2015, **6**, 1-38.

108. A.O. Leu, C. Cai, S.J. McIlroy, G. Southam, V.J. Orphan, Z. Yuan, S. Hu and G.W. Tyson, Anaerobic methane oxidation coupled to manganese reduction by members of the Methanoperedenaceae, *ISME J.*, 2020, **14**, 1030-1041.

109. A. Pienkowska, M. Glodowska, M. Mansor, D. Buchner, D. Straub, S. Kleindienst and A. Kappler, Isotopic Labeling Reveals Microbial Methane Oxidation Coupled to Fe (III) Mineral Reduction in Sediments from an As-Contaminated Aquifer, *Environ. Sci. Technol. Lett.*, 2021, **8**, 832-837.

110. N. Riedinger, M.J. Formolo, T.W. Lyons, S. Henkel, A. Beck and S. Kasten, An inorganic geochemical argument for coupled anaerobic oxidation of methane and iron reduction in marine sediments, *Geobiology*, 2014, **12**, 172-181.

111. K. Martinez-Cruz, M.C. Leewis, I.C. Herriott, A. Sepulveda-Jauregui, K.W. Anthony, F. Thalasso and M.B. Leigh, Anaerobic oxidation of methane by aerobic methanotrophs in sub-Arctic lake sediments, *Sci. Total Environ.*, 2017, **607**, 23-31.

112. L. Cabrol, F. Thalasso, L. Gandois, A. Sepulveda-Jauregui, K. Martinez-Cruz, R. Teisserenc, N. Tananaev, A. Tveit, M.M. Svenning and M. Barret, Anaerobic oxidation of methane and associated microbiome in anoxic water of Northwestern Siberian lakes, *Sci. Total Environ.*, 2020, **736**, 139588.

113. D. Emerson and N.P. Revsbech, Investigation of an iron-oxidizing microbial mat community located near Aarhus, Denmark: laboratory studies, *Appl. Environ. Microbiol.*, 1994, **60**, 4032-4038.

114. K.P. Nevin and D.R. Lovley, Mechanisms for accessing insoluble Fe (III) oxide during dissimilatory Fe (III) reduction by Geothrix fermentans, *Appl. Environ. Microbiol.*, 2002, **68**, 2294-2299.

115. O. Sivan, M. Adler, A. Pearson, F. Gelman, I. Bar-Or, S.G. John and W. Eckert, Geochemical evidence for iron-mediated anaerobic oxidation of methane, *Limnol. Oceanogr.*, 2011, **56**, 1536-1544.

116. O. Sivan, G. Antler, A.V. Turchyn, J.J. Marlow and V.J. Orphan, Iron oxides stimulate sulfate-driven anaerobic methane oxidation in seeps, *PNAS*, 2014, **111**, E4139-E4147.

117. S.C. Whalen and J.C. Cornwell, Nitrogen, phosphorus, and organic carbon cycling in an arctic lake, *Can. J. Fish. Aquat. Sci.*, 1985, **42**, 797-808.

118. R. He, J. Wang, J.W. Pohlman, Z. Jia, Y.X. Chu, M.J. Wooller and M.B. Leigh, Metabolic flexibility of aerobic methanotrophs under anoxic conditions in Arctic lake sediments, *ISME J.*, 2021, DOI: 10.1038/s41396-021-01049-y.

119. J. Jansen, S. MacIntyre., D.C. Barrett, Y.P. Chin, A. Cortés, A.L. Forrest, A.R. Hrycik, R. Martin, B.C. McMeans, M. Rautio and R. Schwefel, Winter limnology: how do hydrodynamics and biogeochemistry shape ecosystems under ice? *J. Geophys. Res.: Biogeosci*, 2021, **126**, p.e2020JG006237.

120. Cornell, R. M.; Schwertmann, U. The Iron Oxides: Structure, Properties, Reactions,Occurrences and Uses; *Wiley-VCH*: Berlin, 2003.

121. Morel, F. M., & Hering, J. G. (1993). Principles and applications of aquatic chemistry. *John Wiley & Sons.*

122. Theis, T. L.; Singer, P. C. Complexation of iron(II) by organic matter and its effect on iron(II) oxidation. *Environ. Sci. Technol. 1974,8, 569−573*

123. Hofstetter, T.B., Heijman, C.G., Haderlein, S.B., Holliger, C. and Schwarzenbach, R.P., 1999. Complete reduction of TNT and other (poly) nitroaromatic compounds under iron-reducing subsurface conditions. *Environmental science & technology*, *33*(9), pp.1479-1487

124. Schwarzenbach, R.P., Gschwend, P.M. and Imboden, D.M., 2005. *Environmental organic chemistry*. John Wiley & Sons

125. Jones, M.E., LaCroix, R.E., Zeigler, J., Ying, S.C., Nico, P.S. and Keiluweit, M., 2020. Enzymes, manganese, or iron? Drivers of oxidative organic matter decomposition in soils. *Environmental Science & Technology*, *54*(21), pp.14114-14123.

126. Klar, J.K., Homoky, W.B., Statham, P.J., Birchill, A.J., Harris, E.L., Woodward, E.M.S., Silburn, B., Cooper, M.J., James, R.H., Connelly, D.P. and Chever, F., 2017. Stability of dissolved and soluble Fe (II) in shelf sediment pore waters and release to an oxic water column. *Biogeochemistry*, *135*(1), pp.49-67.

127. Tamura, H., Goto, K. and Nagayama, M., 1976. Effect of anions on the oxygenation of ferrous ion in neutral solutions. *Journal of Inorganic and Nuclear Chemistry, 38(1), pp.113-117*

128. Strathmann, T.J., 2011. Redox reactivity of organically complexed iron (II) species with aquatic contaminants. In *Aquatic redox chemistry* (pp. 283-313). American Chemical Society.

129. Strathmann, T.J. and Stone, A.T., 2002. Reduction of the pesticides oxamyl and methomyl by FeII: effect of pH and inorganic ligands. *Environmental science & technology*, *36*(4), pp.653-661.

130. Buerge, I.J. and Hug, S.J., 1998. Influence of organic ligands on chromium (VI) reduction by iron (II). *Environmental science & technology*, *32*(14), pp.2092-2099.

131. Rose, A.L. and Waite, T.D., 2003. Effect of dissolved natural organic matter on the kinetics of ferrous iron oxygenation in seawater. *Environmental science & technology, 37(21), pp.4877-4886.*

132. Naka, D., Kim, D. and Strathmann, T.J., 2006. Abiotic reduction of nitroaromatic compounds by aqueous iron (II)− catechol complexes. *Environmental science & technology*, *40*(9), pp.3006-3012.

133. Naka, D., Kim, D., Carbonaro, R.F. and Strathmann, T.J., 2008. Abiotic reduction of nitroaromatic contaminants by iron (II) complexes with organothiol ligands. *Environmental Toxicology and Chemistry: An International Journal, 27(6), pp.1257-1266.*

134. Luther III, G.W., 2016. Inorganic chemistry for geochemistry and environmental sciences: fundamentals and applications. John Wiley & Sons.

135. Stumm, W. and Sulzberger, B., 1992. The cycling of iron in natural environments: considerations based on laboratory studies of heterogeneous redox processes. *Geochimica et Cosmochimica Acta*, *56*(8), pp.3233-3257.

136. Catrouillet, C., Davranche, M., Dia, A., Bouhnik-Le Coz, M., Marsac, R., Pourret, O., & Gruau, G. (2014). Geochemical modeling of Fe (II) binding to humic and fulvic acids. *Chemical Geology, 372, 109-118*.

137. Daugherty, E.E., Gilbert, B., Nico, P.S. and Borch, T., 2017. Complexation and redox buffering of iron (II) by dissolved organic matter. *Environmental science & technology*, *51*(19), pp.11096-11104.

138. Fritzsche, A., Bosch, J., Sander, M., Schröder, C., Byrne, J.M., Ritschel, T., Joshi, P., Maisch, M., Meckenstock, R.U., Kappler, A. and Totsche, K.U., 2021. Organic matter from redoximorphic soils accelerates and sustains microbial Fe (III) reduction. *Environmental Science & Technology*, *55*(15), pp.10821-10831.

139. Curti, L., Moore, O.W., Babakhani, P., Xiao, K.Q., Woulds, C., Bray, A.W., Fisher, B.J., Kazemian, M., Kaulich, B. and Peacock, C.L., 2021. Carboxyl-richness controls organic carbon preservation during coprecipitation with iron (oxyhydr) oxides in the natural environment. *Communications Earth & Environment*, *2*(1), pp.1-13.

140. Kim, D., Duckworth, O.W. and Strathmann, T.J., 2009. Hydroxamate siderophore-promoted reactions between iron (II) and nitroaromatic groundwater contaminants. *Geochimica et Cosmochimica Acta*, *73*(5), pp.1297-1311.

141. Duckworth, O.W. and Sposito, G., 2005. Siderophore− manganese (III) interactions. I. Air-oxidation of manganese (II) promoted by desferrioxamine B. *Environmental science & technology*, *39*(16), pp.6037-6044.

142. Rush, J.D. and Koppenol, W.H., 1987. The reaction between ferrous polyaminocarboxylate complexes and hydrogen peroxide: An investigation of the reaction intermediates by stopped flow spectrophotometry. *Journal of inorganic biochemistry*, *29*(3), pp.199-215.

143. Joe-Wong, C., Shoenfelt, E., Hauser, E.J., Crompton, N. and Myneni, S.C., 2012. Estimation of reactive thiol concentrations in dissolved organic matter and bacterial cell membranes in aquatic systems. *Environmental science & technology*, *46*(18), pp.9854-9861.

144. Strathmann, T.J. and Stone, A.T., 2002. Reduction of oxamyl and related pesticides by FeII: influence of organic ligands and natural organic matter. *Environmental science & technology*, *36*(23), pp.5172-5183.

145. Yu, H., Zhang, P., Liu, J., Zheng, Y. and Mustapha, N.A., 2021. Effects of low-molecular-weight organic acids/thiols on hydroxyl radical production from natural siderite oxidation. *Chemical Geology*, *584*, p.120537.

146. Batinić-Haberle, I., Spasojević, I., Hambright, P., Benov, L., Crumbliss, A.L. and Fridovich, I., 1999. Relationship among redox potentials, proton dissociation constants of pyrrolic nitrogens, and in vivo and in vitro superoxide dismutating activities of manganese (III) and iron (III) water-soluble porphyrins. *Inorganic chemistry*, *38*(18), pp.4011-4022.

147. Sada, E., Kumazawa, H. and Machida, H., 1987. Oxidation kinetics of FeII-EDTA and FeII-NTA chelates by dissolved oxygen. *Industrial & engineering chemistry research*, *26*(7), pp.1468-1472.

148. Seibig, S. and van Eldik, R., 1997. Kinetics of [FeII (edta)] oxidation by molecular oxygen revisited. New evidence for a multistep mechanism. *Inorganic Chemistry*, *36*(18), pp.4115-4120.

149. Thompsen, J.C. and Mottola, H.A., 1984. Kinetics of the complexation of iron (II) with ferrozine. *Analytical Chemistry*, *56*(4), pp.755-757.

150. Viollier, E., Inglett, P.W., Hunter, K., Roychoudhury, A.N. and Van Cappellen, P., 2000. The ferrozine method revisited: Fe (II)/Fe (III) determination in natural waters. *Applied geochemistry*, *15*(6), pp.785-790.

151. Kappler, A., Bryce, C., Mansor, M., Lueder, U., Byrne, J.M. and Swanner, E.D., 2021. An evolving view on biogeochemical cycling of iron. *Nature Reviews Microbiology*, *19*(6), pp.360-374.

152. Miller, C. J., Vincent Lee, S. M., Rose, A. L., & Waite, T. D. (2012). Impact of natural organic matter on H2O2-mediated oxidation of Fe (II) in coastal seawaters. Environmental science & technology, 46(20), 11078-11085.

153. Gorski, C.A., Klüpfel, L., Voegelin, A., Sander, M. and Hofstetter, T.B., 2012. Redox properties of structural Fe in clay minerals. 2. Electrochemical and spectroscopic characterization of electron transfer irreversibility in ferruginous smectite, SWa-1. *Environmental science & technology*, *46*(17), pp.9369-9377.

154. Gorski, C.A., Klüpfel, L.E., Voegelin, A., Sander, M. and Hofstetter, T.B., 2013. Redox properties of structural Fe in clay minerals: 3. Relationships between smectite redox and structural properties. *Environmental science & technology*, *47*(23), pp.13477-13485.

155. Hem, J.D. and Cropper, W.H., 1962. Chemistry of iron in natural water. *USGS Water Supply Papers*, (1459).

156. Santana-Casiano, J. M.; González-Dávila, M.; Millero, F. J. Oxidation of nanomolar levels of Fe(II) with oxygen in natural waters. Environ. Sci. Technol. 2005, 39, 2073−2079.

157. Zhou, N., Luther, G.W. and Chan, C.S., 2021. Ligand Effects on Biotic and Abiotic Fe (II) Oxidation by the Microaerophile Sideroxydans lithotrophicus. *Environmental Science & Technology*.

158. Königsberger, L.C., Königsberger, E., May, P.M. and Hefter, G.T., 2000. Complexation of iron (III) and iron (II) by citrate. Implications for iron speciation in blood plasma. *Journal of inorganic biochemistry*, *78*(3), pp.175-184.

159. Hamada, Y.Z., Bayakly, N., Peipho, A. and Carlson, B., 2006. Accurate Potentiometric Studies of Chromium-Citrate and Ferric-Citrate Complexes in Aqueous Solutions at Physiological and Alkaline pH Values. *Synthesis and Reactivity in Inorganic, Metal-Organic and Nano-Metal Chemistry*, *36*(6), pp.469-476.

160. Pham, A.N. and Waite, T.D., 2008. Modeling the kinetics of Fe (II) oxidation in the presence of citrate and salicylate in aqueous solutions at pH 6.0− 8.0 and 25 C. *The Journal of Physical Chemistry A*, *112*(24), pp.5395-5405.

161. Pham, A.N. and Waite, T.D., 2008. Oxygenation of Fe (II) in the presence of citrate in aqueous solutions at pH 6.0− 8.0 and 25 C: Interpretation from an Fe (II)/citrate speciation perspective. *The Journal of Physical Chemistry A*, *112*(4), pp.643-651.

162. Jones, A.M., Griffin, P.J. and Waite, T.D., 2015. Ferrous iron oxidation by molecular oxygen under acidic conditions: the effect of citrate, EDTA and fulvic acid. *Geochimica et Cosmochimica Acta*, *160*, pp.117-131.

163. González-Davila, M., Santana-Casiano, J.M. and Millero, F.J., 2005. Oxidation of iron (II) nanomolar with H2O2 in seawater. *Geochimica et Cosmochimica Acta*, *69*(1), pp.83-93.

164. Taylor, S.W., Luther III, G.W. and Waite, J.H., 1994. Polarographic and spectrophotometric investigation of iron (III) complexation to 3, 4-dihydroxyphenylalanine-containing peptides and proteins from Mytilus edulis. *Inorganic Chemistry*, *33*(25), pp.5819-5824.

165. Tipping, E., 2002. *Cation binding by humic substances* (Vol. 12). Cambridge University Press

166. Tipping, E., 1998. Humic ion-binding model VI: an improved description of the interactions of protons and metal ions with humic substances. *Aquatic geochemistry*, *4*(1), pp.3-47.

167. Hakala, J.A., Chin, Y.P. and Weber, E.J., 2007. Influence of dissolved organic matter and Fe (II) on the abiotic reduction of pentachloronitrobenzene. *Environmental science & technology*, *41*(21), pp.7337-7342.

168. Bard, A.J. and Faulkner, L.R., 2001. Fundamentals and applications. *Electrochemical methods*, *2*(482), pp.580-632.

169. Kappler, A., Bryce, C., Mansor, M., Lueder, U., Byrne, J.M. and Swanner, E.D., 2021. An evolving view on biogeochemical cycling of iron. *Nature Reviews Microbiology*, *19*(6), pp.360-374.

170. Huang, J., Jones, A., Waite, T.D., Chen, Y., Huang, X., Rosso, K.M., Kappler, A., Mansor, M., Tratnyek, P.G. and Zhang, H., 2021. Fe (II) Redox Chemistry in the Environment. *Chemical Reviews*.

171. Klar, J.K., Homoky, W.B., Statham, P.J., Birchill, A.J., Harris, E.L., Woodward, E.M.S., Silburn, B., Cooper, M.J., James, R.H., Connelly, D.P. and Chever, F., 2017. Stability of dissolved and soluble Fe (II) in shelf sediment pore waters and release to an oxic water column. *Biogeochemistry*, *135*(1), pp.49-67.

172. Herrmann, A.J., Sorwat, J., Byrne, J.M., Frankenberg-Dinkel, N. and Gehringer, M.M., 2021. Diurnal Fe (II)/Fe (III) cycling and enhanced O 2 production in a simulated Archean marine oxygen oasis. *Nature communications*, *12*(1), pp.1-11.

173. Lewis, B.L., Holt, P.D., Taylor, S.W., Wilhelm, S.W., Trick, C.G., Butler, A. and Luther III, G.W., 1995. Voltammetric estimation of iron (III) thermodynamic stability constants for catecholate siderophores isolated from marine bacteria and cyanobacteria. *Marine Chemistry*, *50*(1-4), pp.179-188.

174. Ibisanmi, E., Sander, S.G., Boyd, P.W., Bowie, A.R. and Hunter, K.A., 2011. Vertical distributions of iron-(III) complexing ligands in the Southern Ocean. *Deep Sea Research Part II: Topical Studies in Oceanography*, *58*(21-22), pp.2113-2125.

175. Hunter, K.A. and Boyd, P.W., 2007. Iron-binding ligands and their role in the ocean biogeochemistry of iron. *Environmental Chemistry*, *4*(4), pp.221-232.

176. Ritchie, J.D. and Perdue, E.M., 2003. Proton-binding study of standard and reference fulvic acids, humic acids, and natural organic matter. *Geochimica et cosmochimica acta*, *67*(1), pp.85-96.

177. Driver, S.J. and Perdue, E.M., 2014. Acidic functional groups of Suwannee River natural organic matter, humic acids, and fulvic acids. In *Advances in the Physicochemical Characterization of Dissolved Organic Matter: Impact on Natural and Engineered Systems* (pp. 75-86). American Chemical Society.

178. Aeschbacher, M., Graf, C., Schwarzenbach, R.P. and Sander, M., 2012. Antioxidant properties of humic substances. *Environmental science & technology*, *46*(9), pp.4916-4925.

179. Rose, A.L. and Waite, T.D., 2002. Kinetic model for Fe (II) oxidation in seawater in the absence and presence of natural organic matter. *Environmental Science & Technology*, *36*(3), pp.433-444.

180. Rose, A.L. and Waite, T.D., 2003. Kinetics of iron complexation by dissolved natural organic matter in coastal waters. *Marine chemistry*, *84*(1-2), pp.85-103.

181. Patzner, M.S., Mueller, C.W., Malusova, M., Baur, M., Nikeleit, V., Scholten, T., Hoeschen, C., Byrne, J.M., Borch, T., Kappler, A. and Bryce, C., 2020. Iron mineral dissolution releases iron and associated organic carbon during permafrost thaw. *Nature communications*, *11*(1), pp.1-11.

182. Peiffer, S. and Stubert, I., 1999. The oxidation of pyrite at pH 7 in the presence of reducing and nonreducing Fe (III)-chelators. *Geochimica et cosmochimica acta*, *63*(19-20), pp.3171-3182.

Appendix A

SUPPORTING INFORMATION

A.1 Working Electrode Fabrication

Hg/Au electrodes were tailored for use in both sediment and aquatic environments. To construct the electrodes, BNC cable (Newark Electronics) was stripped down to copper conductor wiring, which was then fixed and soldered to 100 µM gold wire (Alfa). The length of the BNC cable that was stripped and soldered to the gold wire was based on preference, although at least 10 inches total is preferable for sediment work. PEEK™ tubing (0.125”) of the same length as the stripped down copper plus gold wiring was used to house soldered copper and gold wiring and provide protection to the wire. Before placing the soldered wiring into the PEEK™ tubing, a two-part epoxy mix made of 105 resin and 205 hardener (West Marine) in a 4:1 ratio was mixed and immediately injected via syringe into a sectioned piece of PEEK™ tubing. PEEK™ tubing was clamped into a ring stand vertically, and special care was taken to inject the epoxy mix into the bottom of the tubing upwards slowly enough to ensure that no air bubbles formed in the epoxy. The soldered copper and gold wire from the BNC cable was then slowly lowered into the PEEK™, with the gold wire tip was positioned to be either flush or slightly past the bottom of the PEEK™ tubing. Pulling the wire through the PEEK™ tubing allowed the BNC cable to become flush with the top tip of the PEEK™, ensuring a good connection.

Following this step, fresh electrodes filled with epoxy were allowed to harden overnight.

Following overnight hardening, the gold tips of the electrodes were polished by hand using a progression of coarse to fine grained sandpaper (100 to 1000 grit) mounted on a Dremel rotary tool, followed by 15, 6 , 1, ¼ micron diamond pastes (Buehler) on mounted polishing pads (Buehler) on the Dremel tool. It is imperative that Buehler diamond pastes are used in this step, as aluminum abrasives used in commercial electrodes will negatively affect the plating process. Briefly, a small dab of the paste is added to the polishing pad and softened with two drops of polishing oil (Buehler), turning the paste into a soft slurry. Electrodes could be firmly pressed vertically by hand against the rotating Dremel tool in a "figure 8" motion or held in place with a micromanipulator above and assisted by hand, in small figure 8's. Typical polishing times for each sandpaper and paste lasted no longer than 90 seconds.

Immediately following polishing, working electrodes were plated with Hg by placing the working, reference, and counter electrodes in an argon-purged solution of 0.16 M $Hg(NO_3)_2$ dissolved in pH 1.5 deionized water (adjusted with nitric acid) while fixing the potential at -1.0 V for 4 minutes. This step reduces the Hg^{2+} onto the Au surface of the electrode. It is important to use a fritted Ag/AgCl reference electrode in this step, as solid-state Ag/AgCl electrodes will dissolve in the plating solution. Following 4 minutes of Hg plating, an amalgamation step was performed by placing the working electrode and Pt-wire counter electrode in a 0.1 M NaOH solution for 1 minute at a potential of -9 V for the working electrode, and +9V to the counter electrode. The visible formation of bubbles was H_2 gas, confirming reduction of water at the mercury tip, thus also confirming the amalgamation of Hg onto the Au surface

(Brendel and Luther 1995). Successfully plated electrode tips examined under a stereo microscope had a noticeably dull silver tarnish, whereas un-plated gold wire tips were gold and shiny in color. Finally, after the amalgamation step, the plated working electrode, along with the platinum counter and an Ag/AgCl reference electrode were placed in a 0.02 M NaCl solution and tested in cyclic voltammetry mode from -0.1 to -1.8 to -0.1 V 50 to 100 times at 1 V/s in order to check for the existence reproducible O_2 peaks.

A.2 Electrode Calibration

Electrode calibrations for O_2, Fe(II), and Mn(II) were performed using Toolik Lake water from the three sites in order to accurately represent locations where the electrodes would be used in the field. O_2 calibrations were performed based on previously detailed methods (Moore et al. 2009, Hudson et al. 2019). Briefly, lake water was purged to 100% O_2 saturation for 1 to 2 min with a small aquarium bubbler. Upon saturation, CV scans were performed and O_2 peak heights were measured was recorded. Concentrations of O_2 were calculated and corrected for salinity and temperature based on the equation from Weiss (1970):

$$ln[C] = A1 + A2 * \left[\frac{100}{T}\right] + A3 * ln\left[\frac{T}{100}\right] + A4\left[\frac{T}{100}\right] + S‰[B1 + B2\left(\frac{T}{100}\right) + B3\left(\frac{T}{100}\right)^2] \quad \text{(A.1)}$$

Because the ionic strength of Toolik Lake water was low (specific conductivity = 70 µS), unaltered waters were nearly at O_2 saturation (DO unaltered water ~314 µM = 90% saturation: 100% saturation = 352 µM). A two-point calibration curve was then

built from 100% O_2 saturation peak height (nA) vs) 0 nA for a 0% saturation concentration and used to calculate dissolved O_2 throughout the core. Porewater ionic strength were similar to Toolik Lake surface water and temperatures were uniform throughout cores (data not shown).

Aqueous Fe(II) and Mn(II) calibrations were performed by spiking in aliquots of a 10 mM stock solution into a 50 ml Falcon tube filled with unfiltered Toolik Lake water. Water was purged with argon before and during calibrations to prevent oxidation of Fe(II) and Mn(II). Additionally, a small amount of dithionite was added to the Fe(II) stock in order to prevent oxidation. While this step produced a visible FeS peak around -1.1 V, it did not interfere with the Fe(II) peak around -1.43 V. Soluble Fe(III)-organo-complexes were not quantified and reported only as measured current (nA) due to the lack of a proper standard since the nature of these complexes are not known.

A.3 Electrode Measurement Validation

To corroborate our voltammetric measurements we measured dissolved Fe(II) and Fe(III) *ex situ* by the Ferrozine colorimetric analysis. Samples taken from our Rhizon sampler integrated the top 5 cm of the gully water column where we observed lower concentrations for Fe(II) (27.2 µM) while Fe(III) was 14.1 µM. Our Rhizon results corroborate the existence of both Fe(II) *and* Fe(III) as detected by the microelectrode, but the Rhizon measurements are less due to some oxidation artifacts despite our attempts to preserve the sample quickly with HCl. Because of the near circumneutral iron seep pH even small amounts of O_2 diffusion could oxidize some of

the Fe(II). Further, because the Rhizon approach is a composite sample it represents an average of Fe(II) concentrations unlike our microelectrode that measures the analyte at its tip. Thus, while the *in situ* measurement of redox sensitive species using voltammetric microelectrodes provides finer spatial resolution, one must make many more measurements over a larger space to capture Fe(II) concentrations in the solution volume determined by the Rhizon sampler. Nonetheless, the Fe(II) value measured using the Rhizon collected porefluids still compares favorably (within 64%) to the voltammetrically obtained value.

A.4 Solid Phase Fe(III) Abundance Calculation

We determined the amount of solid phase Fe(III) in quasi-equilibrium with porewater Fe(II) based upon an assumed porosity (f) of 0.7 at a depth of 1cm below the SWI. Thus, at this depth the Fe(III) solid phase concentration is 60 µMol/g from Figure 3 and the porewater Fe(II) concentration is 10 µM. Based upon our assumed porosity the sediment-to-water concentration (SW) is

$$SW\ (kg/L) = r_s[(1 - f)/f] \qquad (A.2)$$

Where r_s = the density of a sediment solid (~ 2.5kg/L) (Schwarzenbach et al., 2017). Our SW value would be 1.07kg/L or 1.07 g/mL or 1 gram of sediment will have 0.93 mL of porewater associated with it. The total **moles** of Fe(II) at 1cm would be 9.3 x 10^{-3} µMoles, while the solid phase concentration would contain 60 µMoles. Thus, there is abundant Fe(III) available to the iron reducers present in this sediment layer. Even much deeper in the core there exist sufficient Fe(III) to support iron reduction.

Using the same logic, but a different porosity (0.5) at a depth of 5 cm the solid phase Fe(III) concentration is ~ 7 µMol/g, while the porewater concentration is ~ 300 µM. The SW value would be 2.5 g/mL. Thus, the total moles of Fe(III) would be ~ 17.5 µMoles (based upon a mass of 5.8g), while the moles of Fe(II) in 1 mL of porewater would be 0.3 µMoles. Thus, even at depth sufficient solid phase enough Fe(III) exists to support iron reducers until it is below the detection limit of our analytical method.

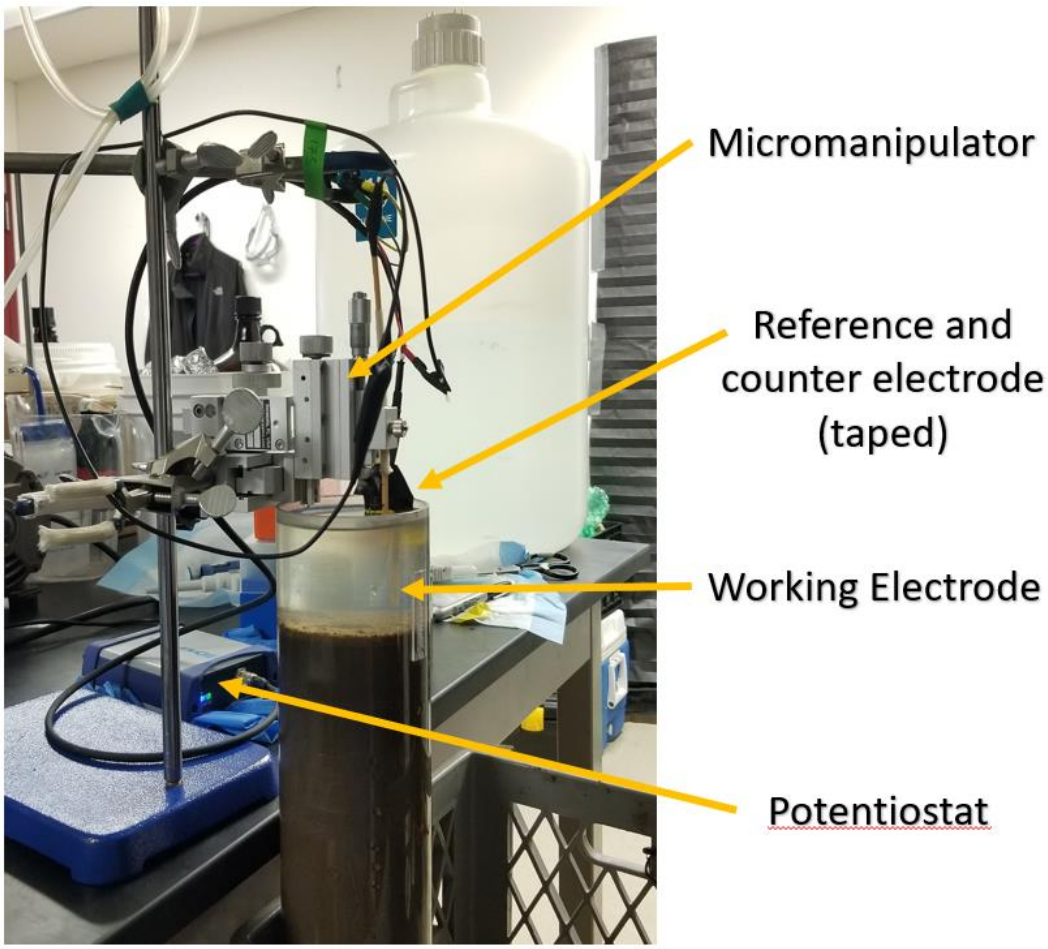

Figure A.1 Field laboratory set-up of ex-situ voltammetric sediment core analysis.

Figure A.2 Iron seep at Oksrukuyik River.

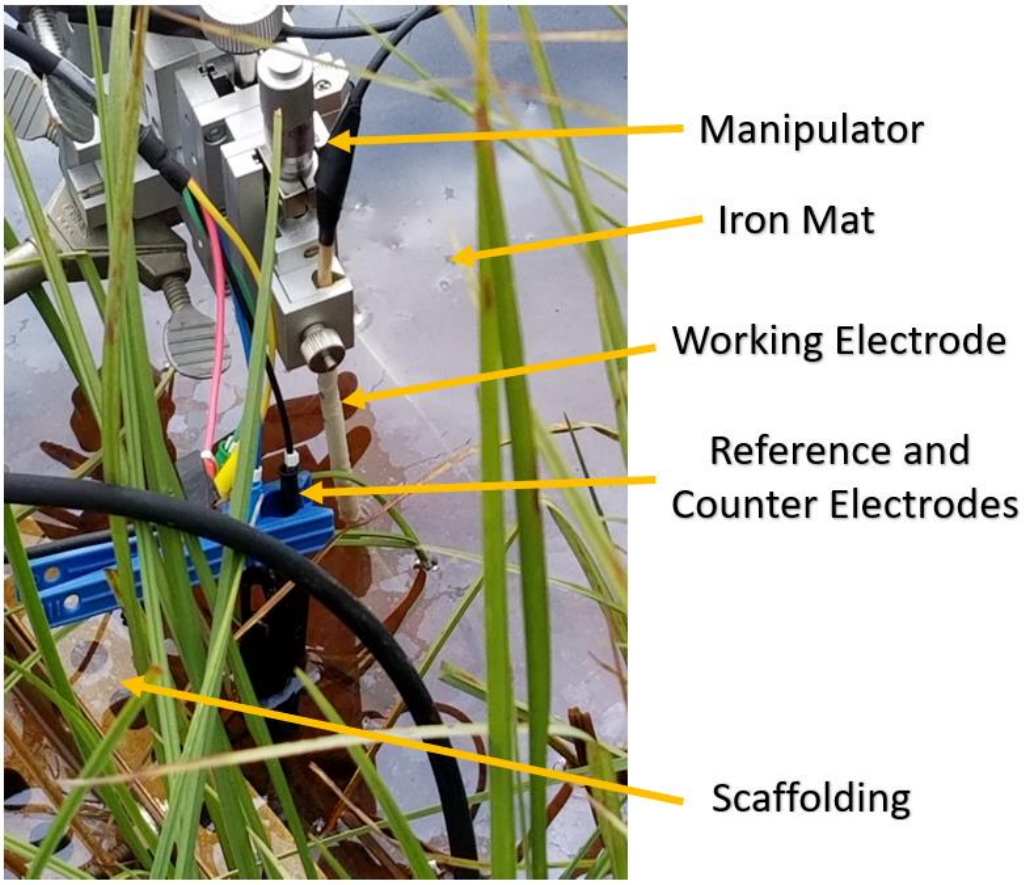

Figure A.3 Oks iron seep field experimental setup.

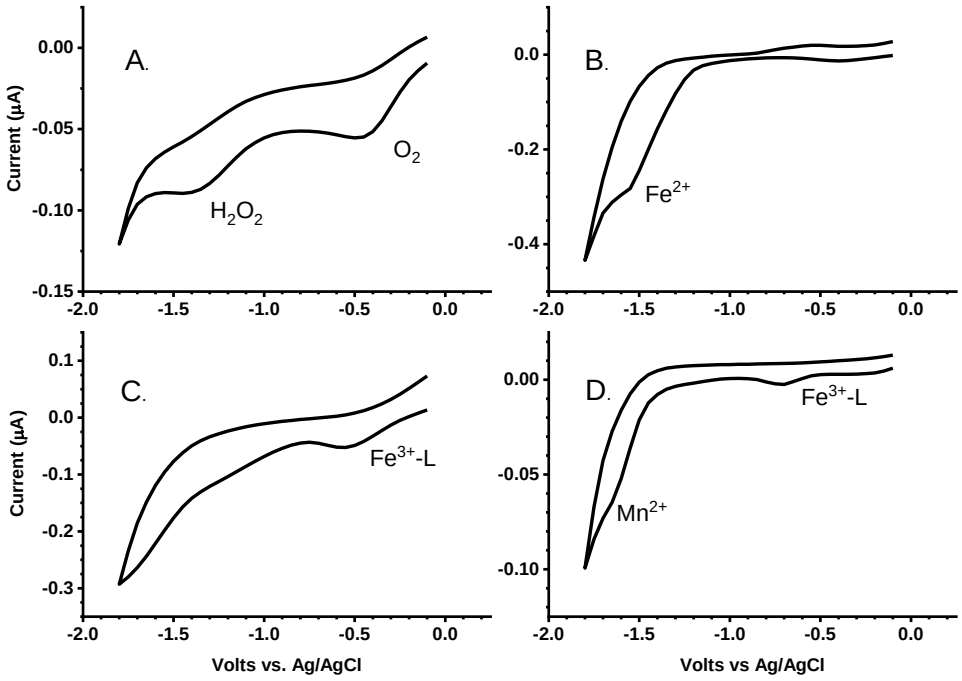

Figure A.4 Representative cyclic voltammograms of species present directly in Toolik Lake and Arctic freshwater samples. A) O_2 (half-wave potential ~ -0.33 V) signal response from Toolik Lake surface water B) Fe(II) (half-wave potential -1.43 V) measured from a Toolik sediment core C) Fe(II) and Fe(III) (present as DOM complex anywhere from -0.4 to -0.9V; -0.5 V here) measured in an iron seep near Oks D) Toolik Lake sediment core scan showing peaks for Mn(II) (half-wave potential at -1.55 V), small concentration of Fe(II) (-1.43), and an Fe(III)-complex (-0.65 V).

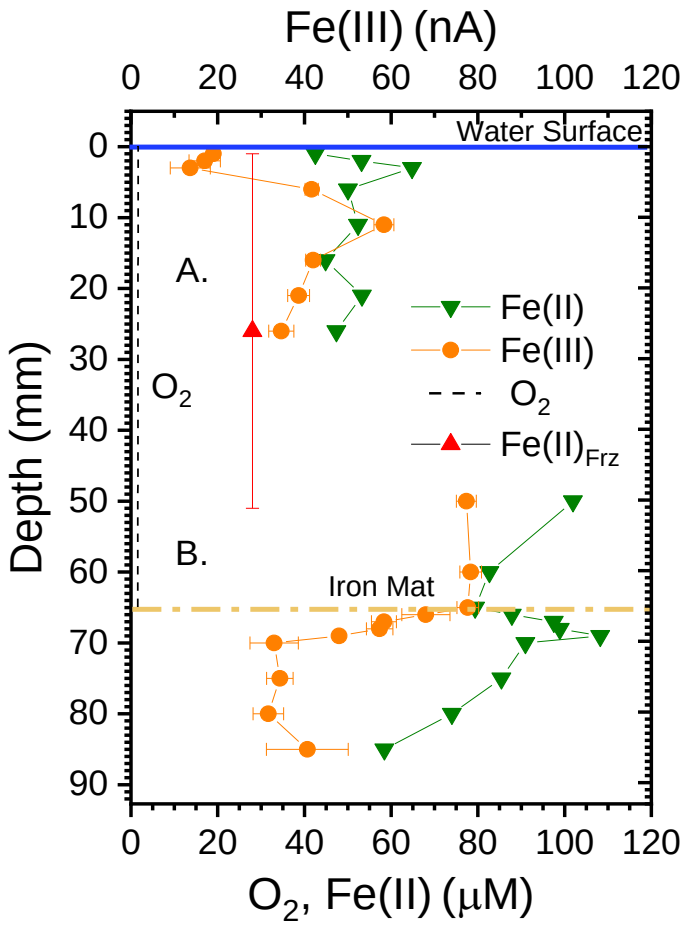

Figure A.5Validation of electrode measurements with Ferrozine assay. An Fe(II) measurement made by Ferrozine assay ($Fe(II)_{Fero}$) is shown by the red triangle. Vertical error bars on the Ferrozine measurement represent the 5 cm integration of vertical space created by the measurement.

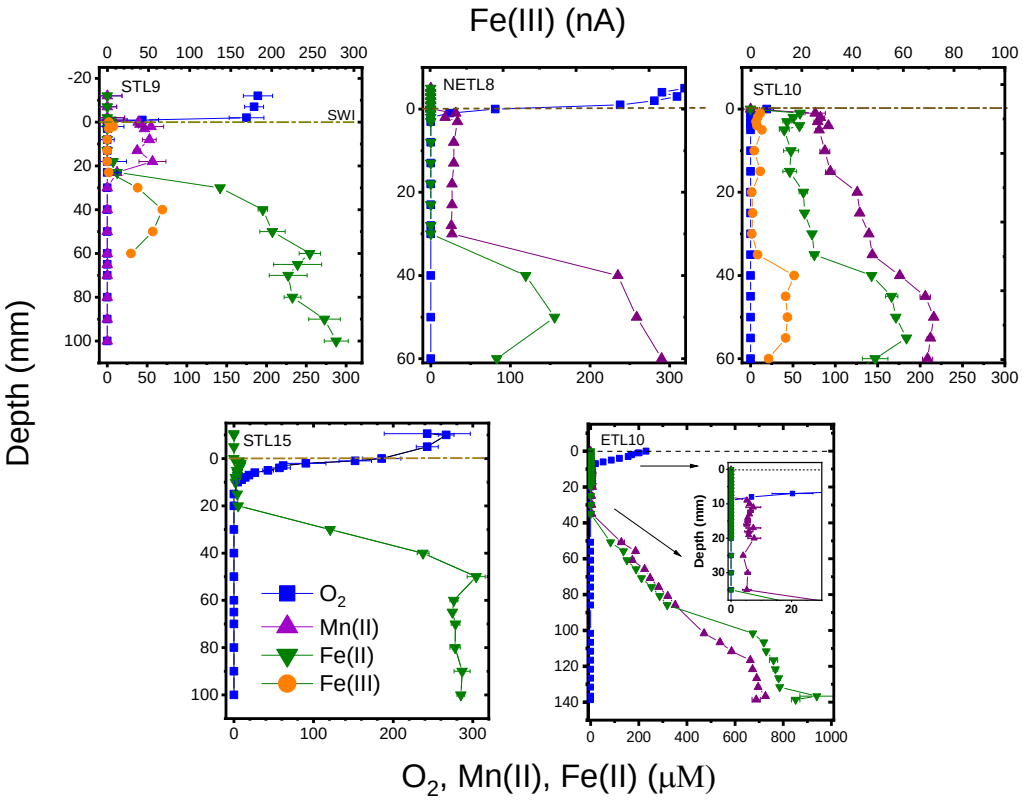

Figure A.6 Cores taken around Toolik Lake. Measurements for O_2, Fe(II), and Mn(II) are in μM, while Fe(III) measurements are reported by current (nA). Note y-axis scales are not uniform in depth, and x-axis scales are not uniform in concentration. Cores are divided by shallow, near shore cores (top row), and deeper, middle lake cores (bottom row).

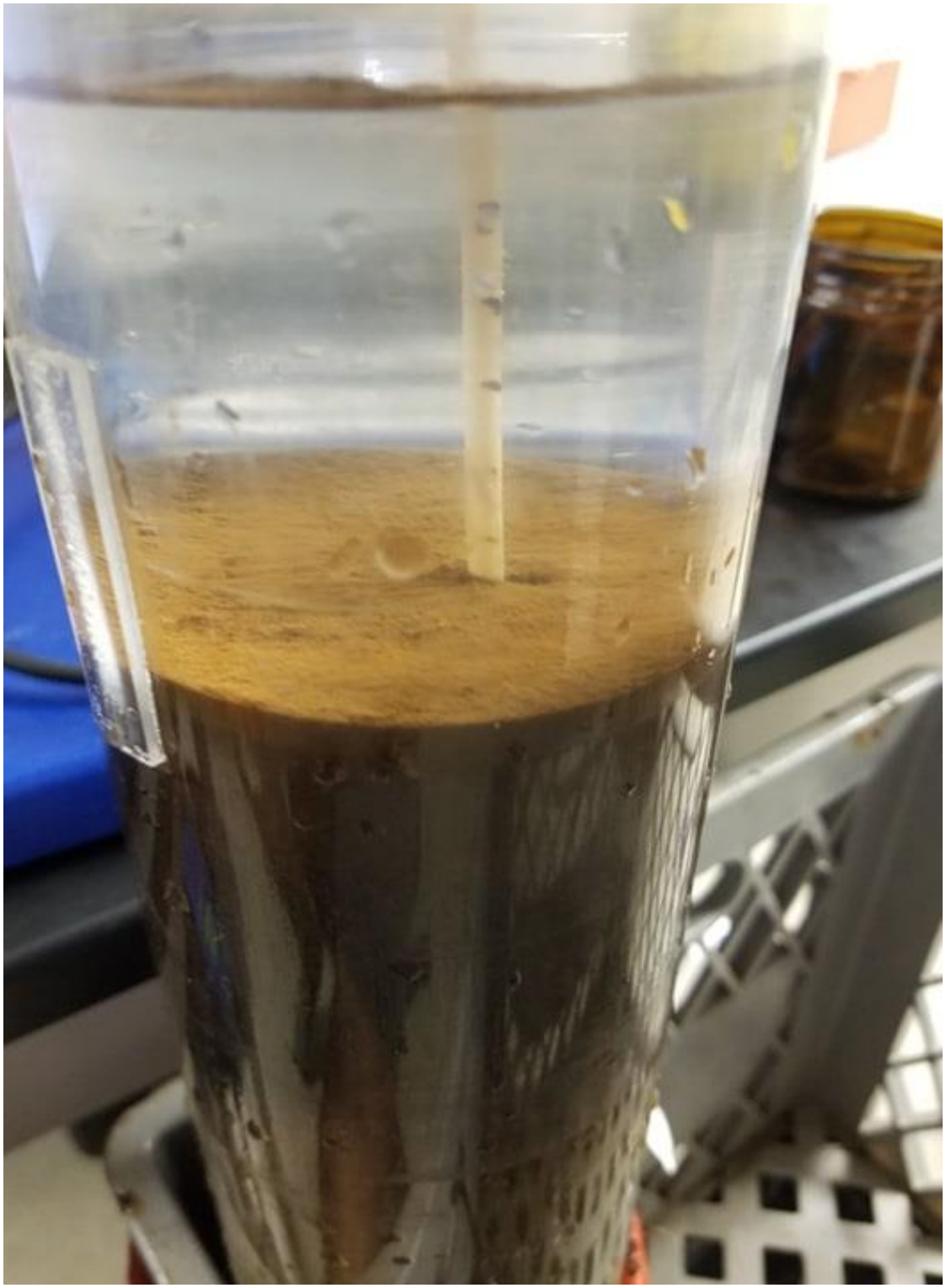

Figure A.7 Iron oxides at the sediment-water interface from Core 2.

A.5 List of Chemicals for Chapter 4 and 5

Mediating compounds ((2,2'-azinobis(3-ethylbenzthiazoline-6-sulfonic acid) diammonium salt (98%) (ABTS), hydroquinone (HQ), hexaammineruthenium(II) chloride (Ru), 2,6-Dichlorophenol-indophenol (DCPIP), and ferri/ferro-cyanide (FeCN) were purchased from sigma. Fe(II) used in experiments was purchased as $FeCl_2$, also from sigma. Acetic acid, 2-(N-morpholino)ethanesulfonic acid (MES), 2-[4-(2-hydroxyethyl)piperazin-1-yl]-ethanesulfonic acid (HEPES), and N-Cyclohexyl-2-aminoethanesulfonic acid (CHES) buffers were purchased from Fisher, as well as the potassium chloride (KCl) salt. 3-(2-Pyridyl)-5,6-diphenyl-1,2,4-triazinep,p -disulfonic acid monosodium salt hydrate (Ferrozine), sodium citrate, nitrilotriacetic acid (NTA), ethylenediaminetetraacetic acid (EDTA), potassium oxalate, and catechol were purchased from Fisher. Potassium hydroxide and hydrochloric acid were also purchased from Fisher.

A.6 Choice of Mediators Used

A.6.1 Mediators investigated

To profile Fe^{II} oxidation extent across a range of oxidizing potentials from +0.1V to +0.77V, we chose to investigate 5 redox mediators. These mediators were chosen due to their high solubility, reversible nature, and mediator redox half-potential.[1,2] Detailed reports on the nature of the redox mediators have been extensively reported elsewhere.[1-4]

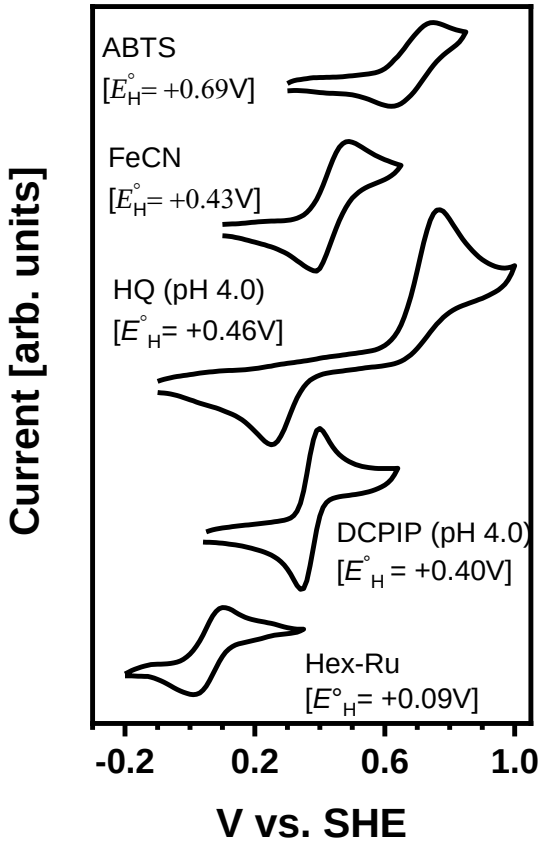

Figure A.8 Cyclic voltammograms (CV's) of 5 mediators investigated in our study plotted as a function of their half-potential (vs. SHE). Note that two of our mediators, DCPIP and HQ, exhibit proton-coupled electron transfer, so the redox potential of the mediators (half-wave potential on voltammograms) changes depending on pH (approximately 60 mV/pH unit). Scan rates shown here were 30 mV/s. CV's of the 5 mediators were performed in the same buffered solutions used for mediated electrochemical experiments (0.1M KCl, 0.01M buffer).

A.6.2 Ferri/Ferro-Cyanide mediator behavior with Fe^{II}

To test the ability of the mediating compounds to effectively facilitate electron transfer from Fe^{II} to the electrochemical cell, we performed individual CVs of all the mediators in buffered solutions in the absence and presence of Fe^{II}. Experiments were

performed by adding in our mediating compounds to a cell containing a working, counter, and reference electrode to achieve concentrations of approximately 300 µM. Fe^{II} was added into the cell to achieve similar concentration ratios to profiling work and incrementally increased to achieve higher concentrations (e.g. ranging from 30 µM to 150 µM). All scans of mediators or mediators with Fe^{II} were performed at a scan rate of 30 mV/s after stirring for 1 minute. For all mediators except FeCN, Fe^{II} did not affect reversibility or current response of the mediator (data not shown). Upon addition of Fe^{II} to our CV experiments with FeCN, however, we saw a change in the reversible nature of the current response, indicating that Fe^{II} affected the ability of FeCN to mediate electrons (Figure A.9.b.). We suspect that there could be mediator binding of Fe^{III} (produced from oxidation of Fe^{II} during anodic CV sweeps) to free CN groups (log K = 43.6) on our FeCN mediator compound, which was only of 98% purity. The formation of colloidal $KFe^{III}[Fe^{II}(CN)_6]$ species (Prussian blue) would be likely given the high concentrations of Fe^{III} formed.[5] Indeed, we noticed the formation of cloudy white to blue substances during our tests with Fe(II) and the FeCN mediator (Figure A.9.a.). Due to the associated interferences of Fe^{II} with this mediator, we opted not to use this mediator in our experiments.

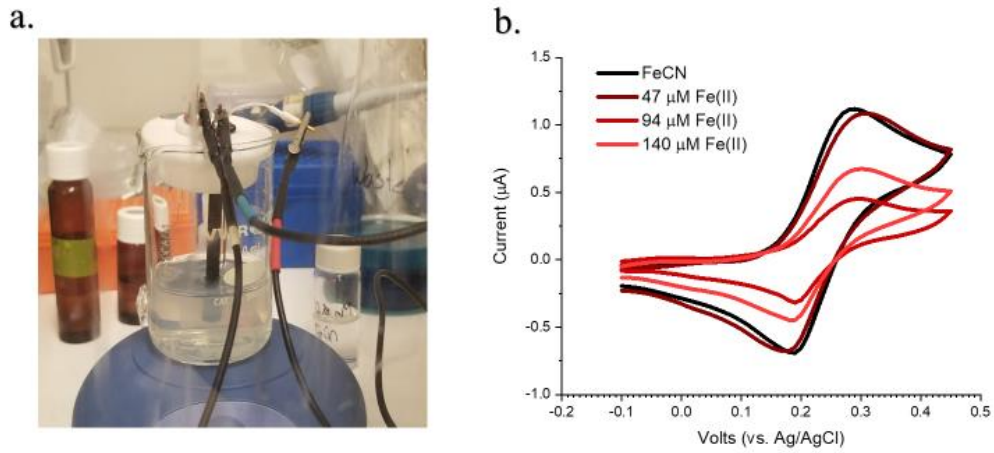

Figure A.9 Interference of reversible electron transfer properties of FeCN upon addition of Fe(II). a. Formation of milky-white/blue substance upon multiple redox cycles of FeCN in the presence of Fe(II) ofr CV experiments. b. Reversibility changes in FeCN voltammogram from conditions without Fe(II), to conditions with increasing concentrations of Fe(II). Scan rates were performed at 30 mV/s. Initial FeCN concentration was 300 μM.

A.6.3 Comparison of $q_{Fe(II)}$ obtained by alternate mediators and no mediators

As previously mentioned, we were not able to use FeCN as a mediator due to deleterious effects between Fe^{II} and the compound. We utilized other mediators to bracket the missing region (430± 120 mV) over which FeCN is reported to be the most effective mediator.[1] To test the efficacy of several mediators, we profiled Fe^{II} oxidation at pH 5 in acetic-acid buffered solutions. We chose pH 5 because it had been used to experimentally determine E_H^{ϕ} of most of our Fe-ligand complexes. At pH 5 under our parameters (activity $\{Fe^{II}\}$ = 10 μM), Fe^{II} oxidation becomes thermodynamically favorable ($\Delta_r G_{ox} < 0$) above +467 mV (Eq A.3, Eq A.4).[6]

$$Fe^{II} + 3H_2O \rightarrow Fe(OH)_3 + 3H^+ + e^- \quad (A.3)$$
$$E_h = 1.060 - 0.1773(pH) - 0.059\log\{Fe^{II}\} \quad (A.4)$$

When tested around these potentials, the FeCN mediator led to inconsistent $q_{Fe^{II}}$ when profiling Fe^{II} oxidation, confirming results from our CVs (Figure S2b.) that FeCN was a poor mediator (Figure S3). We tested hydroquinone (HQ) as a mediator (E_h at pH 5 = 400 mV), as this mediator had the closest half-potential and range (400±60 mV) towards the E_h region where Fe^{II} oxidation was expected to happen (E_h > 467 mV). We also tested the efficacy of hexaammineruthenium(II) chloride (Ru^{II}) as a mediator, which we specifically chose as a mediating compound with a redox potential and expected potential range (90±120 mV) farthest from the range which Fe^{II} was expected to oxidize at pH 5. Typically, it is optimal to choose mediators that are within ±120 mV of the applied E_h at the electrode.[1,3,4] When compared to experiments without any mediators added (i.e. only Fe^{II} added), our results show that HQ, Ru^{II}, and Fe^{II} alone produced similar $q_{Fe^{II}}$, indicating either that all mediators worked efficiently beyond their expected potential range,[1,3,4] or that Fe^{II} did not interact with the mediator during oxidation. Previous work has utilized mediators beyond their optimal E_h ± 120 mV range,[2,7] although not as far as we attempted with Ru^{II} (E_h + 480 mV; Figure S3). While Fe^{II} oxidation at pH 5 produces Fe^{III}-oxyhydroxides (Eq. 1), the oxidation of Fe^{II} to Fe^{III} can be considered a reversible, single-electron transfer process if we consider initial oxidation of Fe^{II} to Fe^{III} (Eq A.5):

$$Fe^{II} \rightarrow Fe^{III} + e^- \quad (A.5)$$

Because of this reason, Fe^{II} oxidation exhibits reversible behavior in a similar fashion to electron mediating compounds (i.e. electron transfer takes place over 240 mV range). Based on our data, we acknowledge that the use of mediators for Fe^{II} oxidation is not necessary, particularly at low pH. However, we opted to use mediators in all experiments, including higher pH experiments where Fe^{III} precipitation in the absence of a ligand was rapid, which could require mediators to preclude any phenomenon that could affect Fe^{II} redox reversibility.

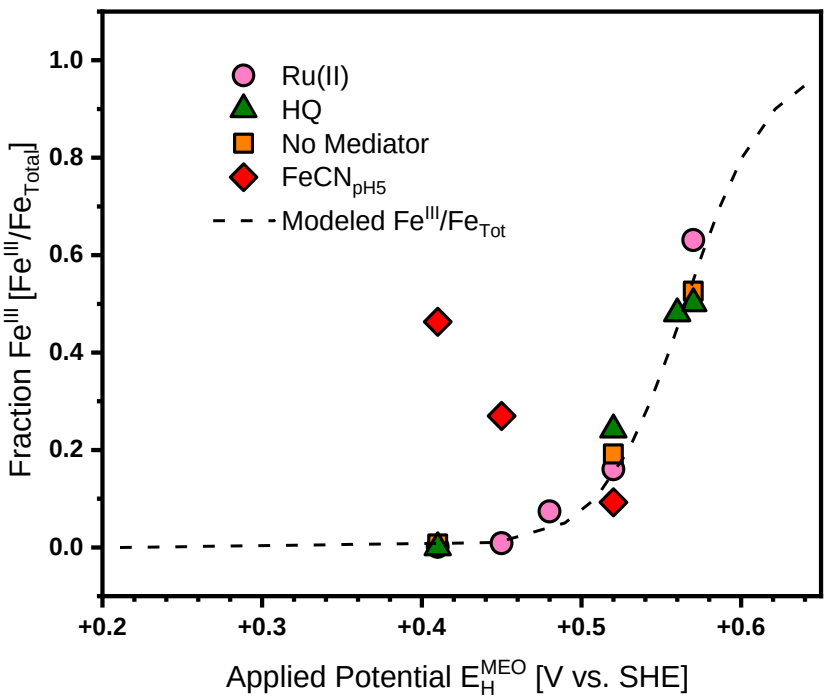

Figure A.10 Comparison of $q_{Fe(II)}$ produced by different mediators at pH 5. The dashed line represents Fe^{II} oxidation at pH 5, modeled based on the Nernst equation, where we assume that Fe^{II} oxidation to Fe^{III} occurs over 240 mV.

A.6.4 Effect of oxidized mediator concentration on Fe(II) oxidation extent

We tested the influence of oxidized mediator concentrations on q_{FeII} by applying different ratios of oxidized mediator concentrations vs. Fe^{II} added to our electrochemical cell. We performed these experiments at oxidizing potentials where Fe^{II} was expected to completely oxidize, and we also tested the response of q_{FeII} in the presence of different ligands. These ratios were dived into two groups, a 1:1 oxidized mediator to Fe^{II} ratio (30 µM: 30 µM), as well as a 10:1 oxidized mediator to Fe^{II} ratio (300 µM: 30 µM). Both ratios showed complete oxidation extent of Fe^{II}, indicating that conditions in all our experiments allowed for complete extent of Fe^{II} oxidation without any artifacts from a lack of oxidized mediator concentrations.

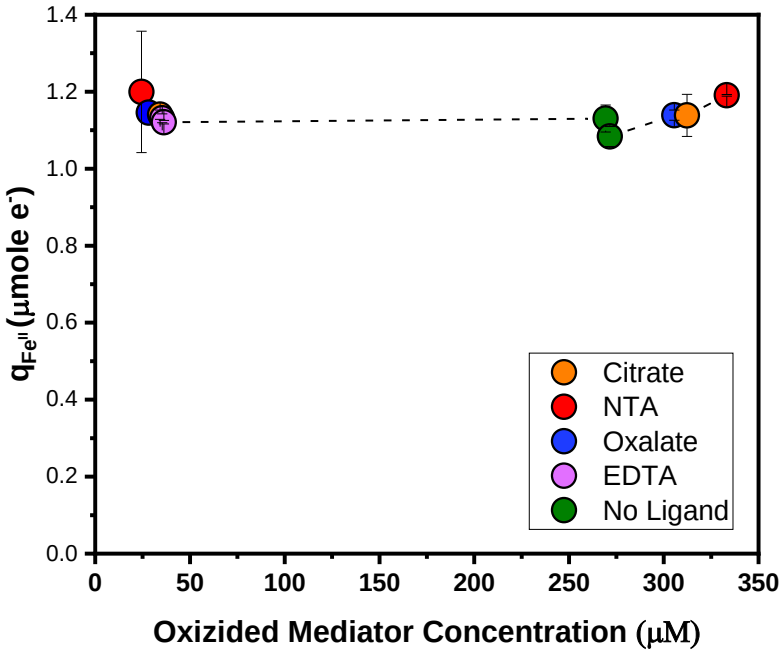

Figure A.11 Oxidized mediator concentrations vs. q_{FeII}. Different colored circles represent Fe^{II} oxidation in experiments with their respective individual ligand or experiments in the absence of ligand (i.e. Fe(II) alone). The dotted line represents maximum q_{FeII} expected based on the amount of Fe(II) added to the cell and the applied potential.

A.7 Example of Speciation Calculation using Visual Minteq

Input Parameters: 30 µM Fe^{II},100.06 mM Cl (Fe as $FeCl_2$ and KCl), 300 µM Citrate, 10 mM Acetate, 100 mM Potassium, pH = 5.00.

	Concentration	Activity	Log activity
Acetate-1	0.0068178	0.0053198	-2.274
Citrate-3	0.000027092	2.9045E-06	-5.537
Cl-1	0.097248	0.075881	-1.12
Fe(OH)2 (aq)	1.5563E-16	1.5929E-16	-15.798
Fe(OH)3-	6.5006E-22	5.0722E-22	-21.295
Fe+2	0.000013403	4.9682E-06	-5.304
Fe-Acetate+	8.5083E-07	6.6388E-07	-6.178
Fe-Citrate-	0.000014356	0.000011201	-4.951
FeCl+	3.0485E-07	2.3786E-07	-6.624
FeH-Citrate (aq)	2.0853E-06	2.1344E-06	-5.671
FeOH+	2.5524E-10	1.9916E-10	-9.701
H+1	0.000012816	0.00001	-5
H2-Citrate-	0.000053435	0.000041694	-4.38
H3-Citrate (aq)	5.4697E-07	5.5985E-07	-6.252
H-Acetate (aq)	0.0029702	0.0030401	-2.517
H-Citrate-2	0.00019502	0.000072289	-4.141
K+1	0.09697	0.075663	-1.121
K-Acetate (aq)	0.00021119	0.00021616	-3.665
K-Citrate-2	7.4639E-06	2.7667E-06	-5.558
KCl (aq)	0.0028113	0.0028775	-2.541
KOH (aq)	1.2935E-10	1.324E-10	-9.878
OH-	1.2905E-09	1.0069E-09	-8.997

Figure A.12 Minteq Output: Concentrations and activities

Component	% of total concentration	Species name
Citrate-3	9.031	Citrate-3
	65.007	H-Citrate-2
	17.812	H2-Citrate-
	0.182	H3-Citrate (aq)
	4.785	Fe-Citrate-
	0.695	FeH-Citrate (aq)
	2.488	K-Citrate-2
K+1	96.97	K+1
	0.211	K-Acetate (aq)
	2.811	KCl (aq)
Cl-1	97.19	Cl-1
	2.81	KCl (aq)
Fe+2	43.236	Fe+2
	2.745	Fe-Acetate+
	0.983	FeCl+
	46.309	Fe-Citrate-
	6.727	FeH-Citrate (aq)
Acetate-1	68.178	Acetate-1
	2.112	K-Acetate (aq)
	29.702	H-Acetate (aq)

Figure A.13 Minteq Output: Species distribution (%)

A.8 Example of Experimental Parameters Chosen using Speciation Data to Determine $E_H^{\emptyset}$

To accurately determine the apparent reduction potential ($E_H^{\emptyset}$) of Fe-L ligand complexes in our experiments, we had to specifically select Fe to ligand ratios and a pH to achieve speciation conditions where our complex of interest was primarily the only complex in abundance in our experiments. This was done by speciation modeling in Visual Minteq prior to experiments. An example can be found below, where we compare Fe^{II} speciation data (% of total concentration) at pH5 between experiments with 10 to 1 ligand to Fe^{II} ratios, and 1 to 1 ligand to Fe^{II} ratios. For 10 to 1 ratios, there is significant interference from FeH-citrate, which makes up 6.7% of the

abundance of total Fe^{II} in the solution. As FeH-citrate is redox-active and reversible,[8] this interferes with the determination of the redox potential of Fe-citrate. For 1 to 1 ratios, the abundance of FeH-Cit is much lower (1.2%). Based on these results, it is optimal to measure $E_H^{\emptyset}$ of Fe^{II}-Cit at experiments at 1 to 1 molar ratios.

Component	% of total concentration	Species name
Citrate-3	9.031	Citrate-3
	65.007	H-Citrate-2
	17.812	H2-Citrate-
	0.182	H3-Citrate (aq)
	4.785	Fe-Citrate-
	0.695	FeH-Citrate (aq)
	2.488	K-Citrate-2
K+1	96.97	K+1
	0.211	K-Acetate (aq)
	2.811	KCl (aq)
Cl-1	97.19	Cl-1
	2.81	KCl (aq)
Fe+2	43.236	Fe+2
	2.745	Fe-Acetate+
	0.983	FeCl+
	46.309	Fe-Citrate-
	6.727	FeH-Citrate (aq)
Acetate-1	68.178	Acetate-1
	2.112	K-Acetate (aq)
	29.702	H-Acetate (aq)

Component	% of total concentration	Species name
Acetate-1	68.163	Acetate-1
	0.016	Fe-Acetate+
	2.113	K-Acetate (aq)
	29.708	H-Acetate (aq)
Fe+2	83.074	Fe+2
	5.28	Fe-Acetate+
	1.892	FeCl+
	8.516	Fe-Citrate-
	1.238	FeH-Citrate (aq)
Citrate-3	8.607	Citrate-3
	62.066	H-Citrate-2
	17.023	H2-Citrate-
	0.174	H3-Citrate (aq)
	8.516	Fe-Citrate-
	1.238	FeH-Citrate (aq)
	2.376	K-Citrate-2
Cl-1	97.188	Cl-1
	2.812	KCl (aq)
K+1	96.974	K+1
	0.211	K-Acetate (aq)
	2.814	KCl (aq)

Figure A.14 10 to 1 Cit to Fe ratios (left) vs 1 to 1 Cit to Fe ratios (right)

A.9 Calculation of Stability Constants

Example: Calculate the thermodynamic stability constant of the Fe^{II}-Citrate complex.

Thermodynamic stability constant, log K_{therm}, is equal to:

$$\frac{\{ML\}}{\{L\}\{M\}} \tag{A.6}$$

Where ML = the activity of the metal-ligand complex,
L = activity of the free ligand
M = activity of the free metal
We will use data obtained in Visual Minteq for Fe^{II} and Citrate in **S3.**
ML (Fe-cit) = 1.12E-5 M
L (cit) = 2.9E-6 M
M (Fe^{2+}) = 4.97E-6 M

Solve for K:

$$K = \frac{\{1.12E-5\}}{\{2.9E-6\}\{4.97E-6\}} = 777100 \tag{Calc. A.1}$$

$$\log(777100) = 5.89 \tag{Calc.A.2}$$

A.10 Stability Constants Generated in Visual Minteq

	log K	delta Hr (kJ/mol)	Citrate-3	Fe+2	H+1	H2O
Fe(OH)2 (aq)	-20.494	119.62	0	1	-2	2
Fe(OH)3-	-30.991	126.43	0	1	-3	3
Fe-Citrate-	5.89	0	1	1	0	0
FeH-Citrate (aq)	10.17	0	1	1	1	0
FeOH+	-9.397	55.81	0	1	-1	1
H2-Citrate-	11.157	1.3	1	0	2	0
H3-Citrate (aq)	14.285	-2.7	1	0	3	0
H-Citrate-2	6.396	3.3	1	0	1	0
OH-	-13.997	55.81	0	0	-1	1

Figure A.15 Example of log K values generated in Visual Minteq for input parameters used in A.7.

A.11 List of Calculated Stability Constants in our Experiments

Table A.1 Calculated stability constants of Fe-Ligand complexes used in this study. All stability constants reported in this table are thermodynamic and were calculated in Visual Minteq (based on previous literature values) or, in the case of ferrozine, experimentally determined. Thermodynamic stability constants of Fe^{III}-ferrozine complexes are not reported in the literature, although conditional stability constant values for Fe^{II}-ferrozine$_3$ are reported and assumed to be higher than Fe^{III} due to the Fe^{II} stabilizing properties of ferrozine.[9] We calculated the stability constants of Fe^{III}-ferrozine$_3$ using potentiometry (see section A.13, A.14).

	Fe^{II}	**Fe^{III}**
Acetate	**1.40**	**4.24**
Oxalate	**3.97**	**9.15**
Oxalate$_2$	**5.90**	**15.45**
Citrate	**5.89**	**13.13**
NTA	**10.18**	**17.82**
NTA$_2$	**12.62**	**25.92**
EDTA	**16.01**	**27.66**
(OH)$_2$	**-20.49**	**-5.75**
Ferrozine$_3$	**15.86***	**12.47***

*denotes value obtained in our experiments via potentiometry

A.12 Calculation of Redox Potential from Stability Constants

Example: Calculate the redox potential of the Fe-citrate complex:

We will use the Nernst Equation:

$$E_{\mathrm{H}}^{0} = 0.77 - 0.059 log(\frac{K_{Fe(III)L}}{K_{Fe(II)L}}) \quad \text{(Calc. A.3)}$$

Data for this calculation (log K from Visual Minteq):

$$\log K_{Fe(III)} = 5.89;\ \log K_{Fe(II)} = 13.1 \quad \text{(Calc. A.4)}$$

Solve for E_{H}^{0}:

$$E_{\mathrm{H}}^{0} = 0.77 - ((0.059*13.1) - (0.059*5.89)) \quad \text{(Calc. A.5)}$$

$$E_{\mathrm{H}}^{0} = +0.34\ \mathrm{V} \quad \text{(Calc. A.6)}$$

A.13 Potentiometry of Iron-Ferrozine Complex

Knowing the redox potential of iron-ferrozine complexes is important to not only predict Fe^{II} oxidation during profiling across a range of oxidizing potentials (E_H^{MEO}), but also to calculate stability constants for Fe^{III} and Fe^{II}-Ferrozine complexes. While redox potentials can be calculated from stability constants, previous values for iron-ferrozine complexes in the literature only reported stability constants for Fe(II)-ferrozine complexes.[9,10,11] Because there is no known reported logK value for Fe(III)-ferrozine, the redox potential of the $Fe^{III/}Fe^{II}$ couple in the ferrozine complex cannot be calculated from stability constants alone.

To directly address this issue, we used potentiometry to measure the redox potential of iron-ferrozine complexes in conditions like those in our MEO

experiments. Potentiometry experiments were conducted in unbuffered 0.1M KCl solutions pH adjusted to 5 to minimize interference from hydroxide species, which can strongly complex Fe^{III} and can strongly influence the redox potential of the Fe^{III}/Fe^{II} couple (see main text). An equimolar solution of 30 µM Fe^{III} and Fe^{II} was dissolved in excess ferrozine (approximately 1 mM) to ensure formation of 3:1 ferrozine to iron complexes, which are the same conditions in our MEO experiments. A platinum-wire working electrode and Ag/AgCl indicator electrode (both from BASi, West Lafayette, IN) were connected to a Dropsens µStat 400 (Metrohm) and run in potentiometric detection mode. The experiment was run for 3 hours to allow for equilibration of the redox couple with the working electrode. Potential drift over 3 hours was 11 millivolts, with most drift occurring in the first hour (data not shown). Following termination of the experiment, the measured potential was +970 mV vs. SHE (Figure 4.1c).

A.14 Calculation of Thermodynamic Stability Constants for Iron Ferrozine Complex

Previous literature[9] reported a conditional stability constant (**$\log K_{cond\ M'L'}$**) value of 15.86 for Fe(II)-$Ferrozine_3$ complexes at pH 5 (bolded, table S4). For Fe(II), the side reaction coefficient (**$\log\alpha_{M'}$**), which accounts for other inorganic species that can act as a ligand, was calculated using Visual Minteq (Table S3). Although no side reaction coefficients for Ferrozine (**$\alpha_{L'}$**) are reported in the literature, we assumed a value of 1. From there, these values were added together[12] to calculate the log of the thermodynamic stability constant (15.86, $K_{therm} = 7.24 \times 10^{15}$ Table S2, S4) for Fe(II)-$Ferrozine_3$ complexes assuming 3:1 ferrozine-iron complexes in our system:

$$\log K_{Therm} = \log K_{COND} + \log \alpha_{M'} + 3 \log \alpha_{L'} \quad (A.7)$$

Following the potentiometric measurement of 970 mV, we used equation 1 to calculate the log of the thermodynamic constant for the Fe(III)(ferrozine)$_3$ complex, which we found to be 12.47 (K_{therm} = 2.95 x 10^{12}). (Table S2, S4). From here, assuming a ferrozine side reaction coefficient value of 1 as there is no hydrogen ion interaction with the N atoms, we used Visual Minteq to calculate the side reaction coefficient for Fe(III) (Table S3). Finally, using these known values we were able to calculate the log of the conditional stability constant ($\log K_{cond\ M'L'}$) for Fe(III)-Ferrozine$_3$ at pH 5 (Table S4).

Table A.2 Minteq Calculations for 30 uM Fe(II) (as $FeCl_2$) or 30 uM Fe(III) (as $Fe(NO_3)_3$), pH 5:

pH 5 Fe(II)	Concentration		
Cl-1	6.00E-05	Fe_{Tot}	3.00E-05
Fe(OH)2 (aq)	9.19E-16	Fe2+	3.00E-05
Fe(OH)3-	2.96E-21	Act. Coeff	1.00E+00
		Side Reaction	
Fe+2	3.00E-05	$\alpha_{M'}$	1.00E+00
FeCl+	1.09E-09	**log ($\alpha_{M'}$)**	**0.00**
FeOH+	1.16E-09		
H+1	1.01E-05		
OH-	1.02E-09		

*Fe(II) Input Parameters: 30 uM Fe2+, 60 uM Cl-1, pH fixed at 5

pH 5 Fe(III)	Concentration		
Fe(OH)2+	2.84E-05	Fe_{Tot}	3.00E-05
Fe(OH)3 (aq)	1.58E-09	Fe3+	1.73E-09
Fe(OH)4-	3.19E-12	Act Coeff.	5.75E-05
		Side Reaction	
Fe+3	1.73E-09	$\alpha_{M'}$	1.74E+04
Fe2(OH)2+4	3.73E-11	**log ($\alpha_{M'}$)**	**4.24**
Fe3(OH)4+5	2.60E-13		
FeOH+2	1.57E-06		
H+1	1.01E-05		
NO3-1	9.00E-05		
OH-	1.02E-09		

*Fe(III) Input Parameters: 30 uM Fe3+, 90 uM NO3-1, pH fixed at 5

Table A.3 Stability constant values for iron-ferrozine complexes in our potentiometric experiment

	log K_{therm}	**log $K_{cond\ M'L'}$**	**log$\alpha_{M'}$**	**ylog$\alpha_{L'}$**
Fe(II) :	**15.86**	**15.86**	0	0
Fe(III):	**12.47**	8.23	4.24	0

A.15 Apparent Reduction Potential Calculations

Calc. S1 Calculate apparent standard reduction potential ($E_H^{\emptyset}$) for Fe-Cit in a molar ratio of 1:1 Fe to Cit at pH 5 and at an applied E_h of +0.3V vs. SHE using the Nernst equation:

$$E_h = E_H^{\emptyset} - 0.059 \cdot \log\left[\frac{Fe^{II}}{Fe^{III}}\right] \quad \text{(Calc. A.7)}$$

Data from these experiments:

$$E_h = +0.3V;\ Fe^{III*} = 21\%\ ;\ Fe^{II} = 79\% \quad \text{(Calc. A.8)}$$

Solve for $E_H^{\emptyset}$ using the Nernst equation:

$$+0.3 = E_H^{\emptyset} - 0.059 \cdot \log\left[\frac{79}{21}\right] \quad \text{(Calc. A.9)}$$

$$E_H^{\emptyset} = +0.33\ \text{V} \quad \text{(Calc. A. 10)}$$

A.16 Calculated redox potentials of the free Fe^{III}/Fe^{II} redox couple.

Table A.4 Calculated redox potentials of free (i.e. no ligands) Fe^{III}/Fe^{II} redox couples. Experimental parameters were used to calculate: Fe^{II} = 30µM, 0.1M KCl, 10 mM buffer. Reported activity coefficients for free Fe^{II} and Fe^{III} are listed at each pH.

pH	Fe2+ (Conc.)	[Fe2+] Activity	Activity coefficient	Fe3+ (Conc.)	[Fe3+] Activity	Activity Coefficient	E_H
4	2.88E-05	1.11E-05	3.85E-01	4.06E-07	4.43E-08	1.09E-01	0.628
5	2.76E-05	1.06E-05	3.83E-01	1.01E-08	1.09E-09	1.08E-01	0.535
6	2.93E-05	1.14E-05	3.87E-01	1.20E-10	1.30E-11	1.08E-01	0.420
7	2.93E-05	1.13E-05	3.86E-01	1.20E-12	1.31E-13	1.09E-01	0.302
8	2.88E-05	1.10E-05	3.82E-01	1.06E-14	1.14E-15	1.07E-01	0.181
9	2.47E-05	9.13E-06	3.70E-01	9.76E-18	1.04E-18	1.07E-01	0.006

A.17 Comparison of Experimental Redox Potentials to values in the Literature

Table A.5 Experiment E_H^{ϕ} vs Literature Values

	Experiment E_H^{ϕ} (V vs. SHE):	**Literature E_H:**
acetate	**0.653 ± 0.007**	**0.63**[129]
oxalate	**0.447 ± 0.013**	**0.47,**[130] **0.50**[129]
$oxalate_2$	**0.214 ± 0.006**	**0.21,**[130] **0.25**[129]
citrate	**0.331 ± 0.015**	**0.37,**[129,130] **0.34**[134]
nta	**0.308 ± 0.007**	**0.30,**[130] **0.36**[129]
nta_2	**0.146 ± 0.003**	**0.06,**[129] **0.11**[130]
edta	**0.109 ± 0.006**	**0.13**[129]
$(OH)_2$	**-0.094 ± 0.028**	**-0.01,**[129,139,134]

A.18 Fe(II) inorganic speciation calculations from pH 4 to 8 in Visual Minteq

pH 4	Concentration (M)	pH 5	(M)	pH 6	(M)	pH 7	(M)	pH 8	(M)
Acetate-1	1.85E-03	Acetate-1	6.82E-03	Cl-1	9.72E-02	Cl-1	9.72E-02	Cl-1	9.72E-02
Cl-1	9.72E-02	Cl-1	9.72E-02	Fe(OH)2	3.42E-14	Fe(OH)2	3.43E-12	Fe(OH)2	3.34E-10
Fe(OH)2 (aq)	3.38E-18	Fe(OH)2	3.21E-16	Fe(OH)3-	1.43E-18	Fe(OH)3-	1.43E-15	Fe(OH)3-	1.40E-12
Fe(OH)3-	1.41E-24	Fe(OH)3-	1.34E-21	Fe+2	2.93E-05	Fe+2	2.93E-05	Fe+2	2.88E-05
Fe+2	2.88E-05	Fe+2	2.76E-05	FeCl+	6.70E-07	FeCl+	6.71E-07	FeCl+	6.55E-07
Fe-Acetate+	5.01E-07	Fe-Acetate+	1.76E-06	FeOH+	5.61E-09	FeOH+	5.61E-08	FeOH+	5.48E-07
FeCl+	6.61E-07	FeCl+	6.29E-07	H+1	1.28E-06	H+1	1.28E-07	H+1	1.28E-08
FeOH+	5.53E-11	FeOH+	5.26E-10	H-MES	5.87E-03	HEPES-1	2.63E-03	HEPES-1	7.82E-03
H+1	1.28E-04	H+1	1.28E-05	K+1	9.72E-02	H-HEPES	7.37E-03	H-HEPES	2.18E-03
H-Acetate (aq)	8.09E-03	H-Acetate	2.97E-03	KCl	2.83E-03	K+1	9.72E-02	K+1	9.72E-02
K+1	9.71E-02	K+1	9.70E-02	KOH	1.30E-09	KCl	2.83E-03	KCl	2.82E-03
K-Acetate (aq)	5.77E-05	K-Acetate	2.11E-04	MES-1	4.13E-03	KOH	1.30E-08	KOH	1.30E-07
KCl (aq)	2.83E-03	KCl (aq)	2.81E-03	OH-	1.29E-08	OH-	1.29E-07	OH-	1.29E-06
KOH (aq)	1.30E-11	KOH (aq)	1.29E-10						
OH-	1.29E-10	OH-	1.29E-09						

Figure A.16 Minteq Speciation Calculation for Fe(II)

A.19 Marcus Expression

The overall expression can be written as:

$$\alpha = \frac{1}{2} + \frac{F(E - E^{\circ})}{2\lambda} \qquad (A.8)$$

The $\frac{F(E-E^{\circ})}{2\lambda}$ term is dimensionless, where:

F has units of coul/mole or A s / mole (96,485 coul)
E has units of Volt or kg m^2 / (s^2 A s) (all V diff is < 0.05 V except for OH_2)
λ has units of J / mole or kg m^2 / (s^2 mole) (1.24 eV or 119,640 J / mole) from spectrum below.

$$\frac{\frac{96{,}485\ \mathrm{A\ s}}{\mathrm{mole}} \quad \frac{(0.03\ \mathrm{kg\ m^2})}{(\mathrm{s^2\ A\ s})} \quad \frac{[\mathrm{s^2\ mole}]}{[2\ (119{,}640)\mathrm{kg\ m^2}]}}{} \qquad \text{(Calc. A.11)}$$

$$\alpha = 0.5 + 0.020 = 0.512 \qquad \text{(Calc. A.12)}$$

All other complexes are closer to 0.5 due to having absorption values of smaller wavelength (larger energy transition, i.e. larger λ). For the $Fe(OH)_2$ case, the max α would be < 0.536.

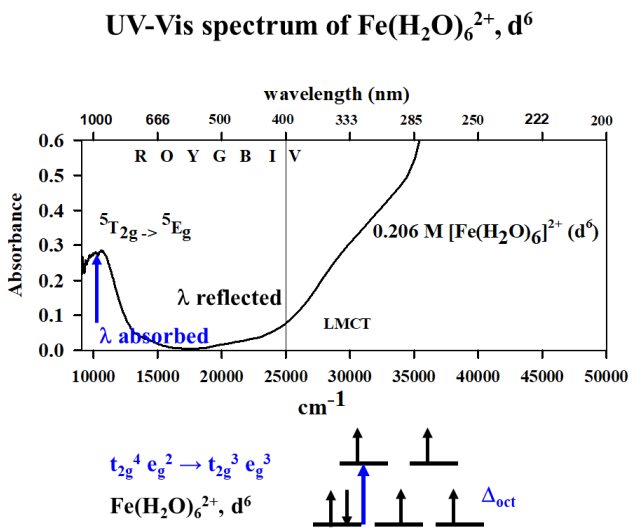

λ in J mol^{-1} from Marcus theory is approximately the d → d transition ($t_{2g}^4 e_g^2 \rightarrow t_{2g}^3 e_g^3$) with a wavelength of ~ 1000 nm (or ~10000 cm^{-1} or ~1.24 eV), which is in the near IR region.

Figure A.17 Absorption peak of $Fe(H_2O)^{2+}$ (taken from Luther, 2016)

A.20 NICA-Donnan DOM Speciation Data at pH 4

Table A.6 SRHA speciation calculations at pH 4. Concentrations of DOM in experiments are listed in upper left hand corner. Percent distributions are based on experimental conditions (i.e. 30 µM Fe(II))

SRHA 49.86 mg C/L

Component	**% of total conc.**	**Species name**
DOC (NICA-Donnan)	100	DOC (NICA-Donnan)
Acetate-1	18.518	Acetate-1
	80.902	H-Acetate (aq)
	0.577	K-Acetate (aq)
Cl-1	97.175	Cl-1
	2.824	KCl (aq)
K+1	96.997	K+1
	2.826	KCl (aq)
	0.058	K-Acetate (aq)
	0.12	(6)K+1D(aq)
Fe+2	71.812	Fe+2
	0.222	HA2-Fe(II)(6)(aq)
	1.647	FeCl+
	1.249	Fe-Acetate+
	1.39	(6)Fe+2D(aq)
	23.68	HA1-Fe(II)(6)(aq)
HFA1-(6)(aq)	45.992	HFA1-(6)(aq)
	51.267	HA1-H(6)(aq)
	2.741	HA1-Fe(II)(6)(aq)
HFA2-(6)(aq)	4.116	HFA2-(6)(aq)
	0.032	HA2-Fe(II)(6)(aq)
	95.852	HA2-H(6)(aq)
(6)H+1D(aq)	0.131	(6)H+1D(aq)
	0.691	(6)Fe+2D(aq)
	99.587	(6)K+1D(aq)

Table A.7 SRHA speciation calculations at pH 4

SRHA 24.69 mg C/L

Component	**% of total concentration**	**Species name**
DOC (NICA-Donnan)	100	DOC (NICA-Donnan)
Acetate-1	18.518	Acetate-1
	80.9	H-Acetate (aq)
	0.577	K-Acetate (aq)
Cl-1	97.174	Cl-1
	2.825	KCl (aq)
K+1	97.056	K+1
	2.827	KCl (aq)
	0.058	K-Acetate (aq)
	0.059	(6)K+1D(aq)
Fe+2	83.501	Fe+2
	0.119	HA2-Fe(II)(6)(aq)
	1.915	FeCl+
	1.452	Fe-Acetate+
	0.798	(6)Fe+2D(aq)
	12.215	HA1-Fe(II)(6)(aq)
HFA1-(6)(aq)	46.115	HFA1-(6)(aq)
	51.03	HA1-H(6)(aq)
	2.856	HA1-Fe(II)(6)(aq)
HFA2-(6)(aq)	4.118	HFA2-(6)(aq)
	0.034	HA2-Fe(II)(6)(aq)
	95.848	HA2-H(6)(aq)
(6)H+1D(aq)	0.131	(6)H+1D(aq)
	0.801	(6)Fe+2D(aq)
	99.477	(6)K+1D(aq)

Table A.8 SRHA speciation calculations at pH 4.

SRHA 12.49 mg C/L

Component	**% of total concentration**	**Species name**
DOC (NICA-Donnan)	100	DOC (NICA-Donnan)
Acetate-1	18.518	Acetate-1
	80.9	H-Acetate (aq)
	0.577	K-Acetate (aq)
Cl-1	97.173	Cl-1
	2.826	KCl (aq)
K+1	97.084	K+1
	2.828	KCl (aq)
	0.058	K-Acetate (aq)
	0.03	(6)K+1D(aq)
Fe+2	89.595	Fe+2
	0.062	HA2-Fe(II)(6)(aq)
	2.055	FeCl+
	1.558	Fe-Acetate+
	0.432	(6)Fe+2D(aq)
	6.298	HA1-Fe(II)(6)(aq)
HFA1-(6)(aq)	46.174	HFA1-(6)(aq)
	50.916	HA1-H(6)(aq)
	2.91	HA1-Fe(II)(6)(aq)
HFA2-(6)(aq)	4.119	HFA2-(6)(aq)
	0.035	HA2-Fe(II)(6)(aq)
	95.846	HA2-H(6)(aq)
(6)H+1D(aq)	0.131	(6)H+1D(aq)
	0.858	(6)Fe+2D(aq)
	99.42	(6)K+1D(aq)

Table A.9 SRHA speciation calculations at pH 4.

SRHA 3.6 mg C/L

Component	**% of total concentration**	**Species name**
DOC (NICA-Donnan)	100	DOC (NICA-Donnan)
Acetate-1	18.519	Acetate-1
	80.899	H-Acetate (aq)
	0.577	K-Acetate (aq)
Cl-1	97.173	Cl-1
	2.827	KCl (aq)
K+1	97.105	K+1
	2.828	KCl (aq)
	0.058	K-Acetate (aq)
Fe+2	94.212	Fe+2
	0.018	HA2-Fe(II)(6)(aq)
	2.16	FeCl+
	1.638	Fe-Acetate+
	0.131	(6)Fe+2D(aq)
	1.84	HA1-Fe(II)(6)(aq)
HFA1-(6)(aq)	46.217	HFA1-(6)(aq)
	50.833	HA1-H(6)(aq)
	2.95	HA1-Fe(II)(6)(aq)
HFA2-(6)(aq)	4.12	HFA2-(6)(aq)
	0.036	HA2-Fe(II)(6)(aq)
	95.844	HA2-H(6)(aq)
(6)H+1D(aq)	0.131	(6)H+1D(aq)
	0.901	(6)Fe+2D(aq)
	99.377	(6)K+1D(aq)

Table A.10 SRHA speciation calculations at pH 4.

SRHA 0 mg C/L

Component	% of total concentration	Species name
Cl-1	97.172	Cl-1
	2.827	KCl (aq)
Acetate-1	18.519	Acetate-1
	0.577	K-Acetate (aq)
	80.899	H-Acetate (aq)
Fe+2	96.124	Fe+2
	1.671	Fe-Acetate+
	2.204	FeCl+
K+1	97.114	K+1
	0.058	K-Acetate (aq)
	2.829	KCl (aq)

Table A.11 SRFA speciation calculations at pH 4. Concentrations of DOM in experiments are listed in upper left hand corner. Percent distributions are based on experimental conditions (i.e. 30 µM Fe(II))

SRFA 48.29 mg C/L

Component	**% of total concentration**	**Species name**
DOC (NICA-Donnan)	100	DOC (NICA-Donnan)
K+1	96.874	K+1
	2.823	KCl (aq)
	0.058	K-Acetate (aq)
	0.246	(6)K+1D(aq)
Cl-1	97.178	Cl-1
	2.821	KCl (aq)
Fe+2	49.683	Fe+2
	1.14	FeCl+
	0.864	Fe-Acetate+
	2.881	(6)Fe+2D(aq)
	45.432	FA1-Fe(II)(6)(aq)
Acetate-1	18.517	Acetate-1
	80.904	H-Acetate (aq)
	0.576	K-Acetate (aq)
HFA1-(6)(aq)	55.73	HFA1-(6)(aq)
	41.361	FA1-H(6)(aq)
	2.909	FA1-Fe(II)(6)(aq)
HFA2-(6)(aq)	0.069	HFA2-(6)(aq)
	99.931	FA2-H(6)(aq)
(6)H+1D(aq)	0.131	(6)H+1D(aq)
	0.698	(6)Fe+2D(aq)
	99.362	

Table A.12 SRFA speciation calculations at pH 4.

SRFA 24.39 mg C/L

Component	**% of total concentration**		**Species name**
DOC (NICA-Donnan)		100	DOC (NICA-Donnan)
K+1		96.993	K+1
		2.826	KCl (aq)
		0.058	K-Acetate (aq)
		0.124	(6)K+1D(aq)
Cl-1		97.175	Cl-1
		2.824	KCl (aq)
Fe+2		69.993	Fe+2
		1.605	FeCl+
		1.217	Fe-Acetate+
		2.026	(6)Fe+2D(aq)
		25.158	FA1-Fe(II)(6)(aq)
Acetate-1		18.518	Acetate-1
		80.902	H-Acetate (aq)
		0.577	K-Acetate (aq)
HFA1-(6)(aq)		55.907	HFA1-(6)(aq)
		40.903	FA1-H(6)(aq)
		3.189	FA1-Fe(II)(6)(aq)
HFA2-(6)(aq)		0.069	HFA2-(6)(aq)
		99.93	FA2-H(6)(aq)
(6)H+1D(aq)		0.131	(6)H+1D(aq)
		0.974	(6)Fe+2D(aq)
		99.088	(6)K+1D(aq)

Table A.13 SRFA speciation calculations at pH 4.

SRFA 12.26 mg C/L

Component	**% of total concentration**	**Species name**
DOC (NICA-Donnan)	100	DOC (NICA-Donnan)
K+1	97.053	K+1
	2.827	KCl (aq)
	0.058	K-Acetate (aq)
	0.062	(6)K+1D(aq)
Cl-1	97.174	Cl-1
	2.825	KCl (aq)
Fe+2	82.3	Fe+2
	1.887	FeCl+
	1.431	Fe-Acetate+
	1.189	(6)Fe+2D(aq)
	13.192	FA1-Fe(II)(6)(aq)
Acetate-1	18.518	Acetate-1
	80.9	H-Acetate (aq)
	0.577	K-Acetate (aq)
HFA1-(6)(aq)	55.997	HFA1-(6)(aq)
	40.673	FA1-H(6)(aq)
	3.33	FA1-Fe(II)(6)(aq)
HFA2-(6)(aq)	0.07	HFA2-(6)(aq)
	99.93	FA2-H(6)(aq)
(6)H+1D(aq)	0.13	(6)H+1D(aq)
	1.139	(6)Fe+2D(aq)
	98.924	(6)K+1D(aq)

Table A.14 SRFA speciation calculations at pH 4.

SRFA 3.53 mg C/L

Component	**% of total concentration**	**Species name**
DOC (NICA-Donnan)	100	DOC (NICA-Donnan)
K+1	97.096	K+1
	2.828	KCl (aq)
	0.058	K-Acetate (aq)
	0.018	(6)K+1D(aq)
Cl-1	97.173	Cl-1
	2.826	KCl (aq)
Fe+2	91.994	Fe+2
	2.11	FeCl+
	1.6	Fe-Acetate+
	0.381	(6)Fe+2D(aq)
	3.915	FA1-Fe(II)(6)(aq)
Acetate-1	18.519	Acetate-1
	80.899	H-Acetate (aq)
	0.577	K-Acetate (aq)
HFA1-(6)(aq)	56.062	HFA1-(6)(aq)
	40.508	FA1-H(6)(aq)
	3.43	FA1-Fe(II)(6)(aq)
HFA2-(6)(aq)	0.07	HFA2-(6)(aq)
	99.93	FA2-H(6)(aq)
(6)H+1D(aq)	0.13	(6)H+1D(aq)
	1.269	(6)Fe+2D(aq)
	98.795	(6)K+1D(aq)

Appendix B

Printed Data for Generating Figures

Table B.1 Data for generating Figure 3.2a.

STL 9

Depth (mm)	O_2 (µM) avg.	O_2 std. dev	Mn(II) (µM) avg.	Mn(II) std. dev	Fe(II) (uM) avg.	Fe(II) std. dev
-12	189.20	18.38	0.00	0.00	0.000	0.00
-7	184.44	11.90	0.00	0.00	0.000	0.00
-2	174.92	21.77	0.00	0.00	0.000	0.00
-1	44.03	20.33	35.84	0.99	4.927	1.77
0	0.00	0.00	38.98	0.75	5.187	1.20
1	0.00	0.00	41.13	3.97	5.187	1.20
2	0.00	0.00	55.04	15.73	5.187	1.20
3	0.00	0.00	46.81	1.18	0.000	0.00
8	0.00	0.00	52.88	8.64	0.000	0.00
13	0.00	0.00	37.61	3.73	0.000	0.00
18	0.00	0.00	56.80	16.89	7.261	0.00
23	0.00	0.00	12.34	0.75	12.448	5.36
30	0.00	0.00	0.00	0.00	141.857	2.14
40	0.00	0.00	0.00	0.00	195.280	5.89
50	0.00	0.00	0.00	0.00	207.469	15.96
60	0.00	0.00	0.00	0.00	254.409	13.38
65	0.00	0.00	0.00	0.00	239.108	30.09
70	0.00	0.00	0.00	0.00	227.178	23.73
80	0.00	0.00	0.00	0.00	232.624	10.63
90	0.00	0.00	0.00	0.00	272.822	19.70
100	0.00	0.00	0.00	0.00	287.604	15.04

Table B.2 Data for generating Figure 3.2 b.

STL 15

Depth (mm)	O_2 (µM) avg.	O_2 std. dev.	Fe(II) (uM) avg	Fe(II) std. dev
-10.5	242.74	54.06	0.00	0.00
-10	266.54	9.91	0.00	0.00
-5	242.74	13.74	0.00	0.00
0	185.63	24.11	0.00	0.00
1	152.31	20.33	6.74	5.52
2	90.43	25.00	8.82	4.68
3	61.88	2.75	8.30	3.69
4	57.12	13.67	6.74	1.04
5	42.84	6.73	3.63	2.47
6	26.18	3.89	4.41	0.99
7	19.04	2.38	4.41	1.56
8	14.28	2.38	1.82	1.31
9	9.52	3.89	2.85	0.99
10	4.76	3.89	1.82	2.14
15	0.00		4.15	0.00
20	0.00		5.45	0.52
30	0.00		120.85	1.80
40	0.00		237.55	7.38
50	0.00		304.20	11.41
60	0.00		276.19	4.82
65	0.00		274.38	0.60
70	0.00		278.27	5.45
80	0.00		277.75	6.42
90	0.00		286.57	10.18
100	0.00		285.01	4.82

Table B.3 Data for generating Figure 3.4a.

Iron Mat

Depth (mm)	Fe(III) nA (avg.)	Fe(III) std. dev.	Fe(II) uM avg.	Fe(II) std. dev.
1	19.00	1.00	42.53	2.25
2	17.00	3.61	53.16	2.30
3	13.67	4.62	64.83	9.51
6	41.67	1.53	50.05	2.60
11	58.33	2.31	52.39	5.13
16	42.00	1.73	44.87	5.84
21	38.67	2.52	53.25	2.16
26	34.67	2.89	47.37	2.62
50	77.33	2.31	101.92	5.30
60	78.33	2.52	82.64	3.65
65	77.67	2.52	79.36	5.13
66	68.00	5.57	87.83	6.37
67	58.33	2.89	97.51	0.48
68	57.33	3.06	98.89	2.09
69	48.00	1.00	108.23	10.92
70	33.00	5.57	90.94	4.29
75	34.33	3.06	85.41	3.10
80	31.67	3.51	74.00	9.37
85	40.67	9.45	58.44	5.17

Table B.4 Data for generating Figure 4.2b.

E_H^{MEO}	NTA avg. ($q_{Fe(II)}$)	NTA std dev.	Ferrozine	Fz. std dev	Cit avg.	Cit std dev.	Fe(II) Alone avg.	Fe(II) std dev.
0.77	1.19	0.00	0.07	0.04	1.13	0.02	1.14	0.06
0.69	1.19	0.04	0.00	0.00	1.17	0.01	0.85	0.09
0.61	1.23	0.04	0.00	0.00	1.14	0.01	0.19	0.06
0.52	1.12	0.00	0.00	0.00	0.99	0.06	0.00	0.00
0.41	0.98	0.09	0.00	0.00	0.54	0.11	0.00	0.00
0.3	0.17	0.03	0.00	0.00	0.03	0.01	0.00	0.00

Table B.5 Data for generating Figure 4.2c.

pH	NTA avg. ($q_{Fe(II)}$)	NTA std dev.	Ferrozine	Fz. std dev	Cit avg.	Cit std dev.	Fe(II) Alone avg.	Fe(II) std dev.
4	0.17	0.03	0.00	0.00	0.03	0.01	0.00	0.00
5	0.83	0.10	0.00	0.00	0.84	0.08	0.00	0.00
6	1.19	0.01	0.00	0.00	1.06	0.02	0.00	0.00
7	1.15	0.01	0.00	0.00	1.20	0.03	1.04	0.01
8	1.24	0.02	0.01	0.01	1.13	0.05	0.92	0.10

Table B.6 Data for generating Figure 4.2d.

E_H^{MEO}	NTA avg. ($q_{Fe(II)}$)	NTA std dev.	Ferrozine	Fz. std dev	Cit avg.	Cit std dev.	Fe(II) Alone avg.	Fe(II) std dev.
0.3	1.15	0.01	0.00	0.00	1.20	0.03	1.04	0.01
0.25	1.19	0.04	0.00	0.00	1.21	0.06	1.11	0.02
0.2	1.07	0.04	0.00	0.00	1.22	0.04	1.17	0.03
0.15	0.56	0.07	0.00	0.00	1.08	0.04	1.11	0.03
0.1	0.15	0.00	0.00	0.00	1.11	0.02	0.00	0.00

Table B.7 Data for generating Figure 4.4e.

conc. (mM)	$q_{Fe(II)}$
0.03229	0.19775
0.16014	0.69773
0.32032	0.8433
0.64132	1.03415

Table B.8 Data for generating Figure 4.4f.

pH	$q_{Fe(II)}$
4	0.0314
5	0.84333
6	1.06469
7	1.2034
8	1.13468

Table B.9 Data for generating Figure 4.4g.

conc. (mM)	$q_{Fe(II)}$
0.03177	0.32202
0.15587	0.72612
0.29235	0.7426
0.61723	0.73908

Table B.10 Data for generating Figure 4.4h.

pH	$q_{Fe(II)}$
4	0.1694
5	0.7426
6	1.18713
7	1.15116
8	1.23548

Table B.11 Data for generating Figure 5.2a.

SRFA [g C/L]	$q_{Fe(II)/FeTot}$
0.00	0.16
0.00	0.08
0.01	0.26
0.02	0.49
0.05	0.74

Table B.12 Data for generating Figure 5.2b.

SRFA [g C/L]	$q_{Fe(II)/FeTot}$
0.00	0.16
0.00	0.05
0.01	0.30
0.02	0.55
0.05	0.96

Appendix C

C.1 Publication List Related to Dissertation

Chapter 2:

Hudson, J.M., MacDonald, D.J., Estes, E.R. and Luther III, G.W., 2019. A durable and inexpensive pump profiler to monitor stratified water columns with high vertical resolution. *Talanta*, *199*, pp.415-424.

Chapter 3:

Hudson, J.M., Michaud, A.B., Emerson, D. and Chin, Y.P., 2022. Spatial distribution and biogeochemistry of redox active species in arctic sedimentary porewaters and seeps. *Environmental Science: Processes & Impacts*.

Chapter 4:

Influence of Organic Ligands on the Redox Properties of Fe(II) as Determined by Mediated Electrochemical Oxidation. In Review at *Environmental Science and Technology*

Other Publications During PhD:

Xin, D., Saha, N., Reza, M.T., Hudson, J. and Chiu, P.C., 2021. Pyrolysis creates electron storage capacity of black carbon (biochar) from lignocellulosic biomass. *ACS Sustainable Chemistry & Engineering*, *9*(19), pp.6821-6831.

McAdams, B.C., Hudson, J.M., Arnold. W.A., Chin, Y.P. Reduction of CHOS-rich aquatic dissolved organic matter affects adsorption to goethite To be submitted in April to *Aquatic Geochemistry*

C.2 Selected Presentation List

Hudson, J.M., Chin, Y.P. Redox properties of iron-ligand complexes in dissolved organic matter. IHSS Virtual Meeting, Estes Park, CO 2021 (Poster-presented by Hudson)

Hudson, J.M., Chin, Y.P. Influence of organic ligands and dissolved organic matter on redox properties of Fe(II) as determined by mediated electrochemical oxidation. ACS Virtual Spring Meeting, San Antonio, TX 2021 (Oral- presented by Hudson)

Hudson, J. M., Chin, Y.P Electron Exchange Capacity and Reactivity of Iron-Ligand Complexes in a Freshwater Stream. Goldschmidt Conference, Barcelona, Spain 2019 (Oral- presented by Hudson)

Appendix D

PERMISSIONS

Chapter 2 is a reprinted version of an article published in *Talanta*, an Elsevier journal. According to the policies of Elsevier, the authors can include their articles in a dissertation, provided that the dissertation is not published commercially. For further information on the copyright policies of Elsevier, please see the link: https://www.elsevier.com/about/policies/publishing-ethics#Authors.

Chapter 3 is a reprinted version of an article published in *Environmental Science: Processes and Impacts*, a Royal Society of Chemistry journal. According to the policies of the Royal Society of Chemistry, articles can be included in dissertations as long as they are not published commercially. For further information on the copyright policies of the Royal Society of Chemistry, please see the link: https://www.rsc.org/journals-books-databases/author-and-reviewer-hub/authors-information/licences-copyright-permissions/.